



Merger Rate Density of Population III Binary Black Holes Below, Above, and in the Pair-instability Mass Gap

Ataru Tanikawa¹ , Hajime Susa² , Takashi Yoshida^{3,4} , Alessandro A. Trani¹ , and Tomoya Kinugawa⁵

¹ Department of Earth Science and Astronomy, College of Arts and Sciences, The University of Tokyo, 3-8-1 Komaba, Meguro-ku, Tokyo 153-8902, Japan
tanikawa@ea.c.u-tokyo.ac.jp

² Department of Physics, Konan University, Okamoto, Kobe, Japan

³ Department of Astronomy, Graduate School of Science, The University of Tokyo, Bunkyo-ku, Tokyo, Japan

⁴ Yukawa Institute for Theoretical Physics, Kyoto University, Kyoto 606-8502, Japan

⁵ Institute for Cosmic Ray Research, The University of Tokyo, Kashiwa, Chiba, Japan

Received 2020 August 4; revised 2021 January 30; accepted 2021 February 6; published 2021 March 24

Abstract

We present the merger rate density of Population III binary black holes (BHs) by means of a widely used binary population synthesis code BSE with extensions to very massive and extreme metal-poor stars. We consider not only low-mass BHs (LBHs: $5\text{--}50M_{\odot}$) but also high-mass BHs (HBHs: $130\text{--}200M_{\odot}$), where LBHs and HBHs are below and above the pair-instability mass gap ($50\text{--}130M_{\odot}$), respectively. Population III BH–BHs can be categorized into three subpopulations: BH–BHs without HBHs (hBH0s: $m_{\text{tot}} \lesssim 100M_{\odot}$), with one hBH (hBH1s: $m_{\text{tot}} \sim 130\text{--}260M_{\odot}$), and with two HBHs (hBH2s: $m_{\text{tot}} \sim 270\text{--}400M_{\odot}$), where m_{tot} is the total mass of a BH–BH. Their merger rate densities at the current universe are $\sim 0.1 \text{ yr}^{-1} \text{ Gpc}^{-3}$ for hBH0s, and $\sim 0.01 \text{ yr}^{-1} \text{ Gpc}^{-3}$ for the sum of hBH1s and hBH2s, provided that the mass density of Population III stars is $\sim 10^{13}M_{\odot} \text{ Gpc}^{-3}$. These rates are modestly insensitive to initial conditions and single star models. The hBH1 and hBH2 mergers can dominate BH–BHs with HBHs discovered in the near future. They have low effective spins $\lesssim 0.2$ in the current universe. The number ratio of hBH2s to hBH1s is high, $\gtrsim 0.1$. We also find that BHs in the mass gap (up to $\sim 85M_{\odot}$) merge. These merger rates can be reduced to nearly zero if Population III binaries are always wide ($\gtrsim 100R_{\odot}$), and if Population III stars always enter into chemically homogeneous evolution. The presence of close Population III binaries ($\sim 10R_{\odot}$) is crucial for avoiding the worst scenario.

Unified Astronomy Thesaurus concepts: Astrophysical black holes (98); Stellar mass black holes (1611); Massive stars (732); Close binary stars (254); Common envelope binary stars (2156); Population III stars (1285); Gravitational waves (678)

1. Introduction

In 2015, gravitational wave (GW) observatories, LIGO, first detected GWs; these GWs came from a merger of two black holes (BHs; Abbott et al. 2016). Since then, GW observatories, LIGO and Virgo, have continuously discovered a large number of BH–BH mergers, and have published ~ 50 BH–BH mergers with detailed information, such as their masses, distances, spin magnitudes, and spin–orbit misalignments as of 2020 December (Abbott et al. 2019, 2020a, 2020b, 2020c, 2020d; The LIGO Scientific Collaboration et al. 2020). Moreover, research groups other than the LIGO–Virgo collaboration have found other BH–BHs (Zackay et al. 2019; Venumadhav et al. 2020). Many of them contain BHs with $\sim 30M_{\odot}$, significantly more massive than the BHs previously discovered in X-ray binaries, $\lesssim 15M_{\odot}$ (e.g., Casares et al. 2017). Thus, the origin(s) of merging BH–BHs has been controversial.

Many formation scenarios of merging BH–BHs have been currently suggested. Population I/II binaries evolve to merging BH–BHs through common-envelope evolution (Bethe & Brown 1998; Belczynski et al. 2002, 2014, 2016a, 2020a; Dominik et al. 2012, 2013; Mennekens & Vanbeveren 2014; Spera et al. 2015, 2019; Eldridge & Stanway 2016; Eldridge et al. 2017, 2019; Mapelli et al. 2017, 2019; Stevenson et al. 2017; Giacobbo & Mapelli 2018; Kruckow et al. 2018; Mapelli & Giacobbo 2018). Close binaries can also form merging BH–BHs through chemically homogeneous evolution (CHE; de Mink et al. 2009; Mandel & de Mink 2016; Marchant et al. 2016; du Buisson et al. 2020; Hong et al. 2020; Riley et al. 2020). Dynamical interactions in globular clusters (GCs) give rise to merging BH–BHs

(Portegies Zwart & McMillan 2000; Downing et al. 2010; Tanikawa 2013; Bae et al. 2014; Rodriguez et al. 2016a, 2016b, 2018a, 2018b; Askar et al. 2017; Fujii et al. 2017; Park et al. 2017; Samsing & Ramirez-Ruiz 2017; Hong et al. 2018; Samsing 2018; Samsing et al. 2018). In open clusters, merging BH–BHs are formed by a combination of common-envelope evolution and dynamical interactions (Ziosi et al. 2014; Mapelli 2016; Banerjee 2017, 2018a, 2018b; Di Carlo et al. 2019, 2020a, 2020b; Kumamoto et al. 2019, 2020; Rastello et al. 2019). Dynamical interactions can form merging BH–BHs also in galactic centers (O’Leary et al. 2009; Antonini & Perets 2012; Antonini & Rasio 2016; VanLandingham et al. 2016; Bartos et al. 2017; Petrovich & Antonini 2017; Stone et al. 2017; Hamers et al. 2018; Hoang et al. 2018; Leigh et al. 2018; McKernan et al. 2018; Rasskazov & Kocsis 2019; Trani et al. 2019; Yang et al. 2019; Arca Sedda 2020; Mapelli et al. 2020; McKernan et al. 2020; Tagawa et al. 2020a, 2020b). Merging BH–BHs can emerge through secular evolution in stable triple systems (TSs) and quadruple systems (QSs; Antonini et al. 2014, 2017; Silsbee & Tremaine 2017; Rodriguez & Antonini 2018; Fragione & Kocsis 2019; Liu & Lai 2019; Fragione et al. 2020; Hamers & Safarzadeh 2020). Although merging BH–BHs originate from astrophysical objects in the above scenarios, even primordial BHs, made from dark matter, can generate merging BH–BHs (Sasaki et al. 2016).

Population III binary stars, which are formed from primordial gas at the high-redshift universe, can also give rise to merging BH–BHs. The typical BH mass is $\sim 30M_{\odot}$, larger than Population I/II BH–BHs (Kinugawa et al. 2014). This is not

because Population III stars have a top-heavy initial mass function (IMF), but because Population III binaries tend to experience stable mass transfer owing to their radiative envelopes (Kinugawa et al. 2016a; Inayoshi et al. 2017). This argument is also robust against uncertainties of binary evolutions, such as efficiencies of mass transfer, mass accretion, common envelope, and tidal interaction (Kinugawa et al. 2020). Because the typical BH mass is consistent with observed BH–BH masses, Population III binaries is one of the promising origins.

It is uncertain whether Population III BH–BHs are the dominant origin of observed BH–BHs (Hartwig et al. 2016; Belczynski et al. 2017; Kinugawa et al. 2020). Moreover, observed BH–BHs may be mainly formed through dynamical interactions (Callister et al. 2020). However, even if Population III BH–BHs are not dominant, it should be worthwhile to identify Population III BH–BHs from observed BH–BHs. Population III stars are key ingredients of the cosmic dawn, the reionization of the universe, the beginning of stellar nucleosynthesis, and so on. Despite their importance, Population III stars are not directly observed (Rydberg et al. 2013). Because Population III stars are typically massive stars, $10\text{--}1000M_{\odot}$ (Omukai & Nishi 1998; Abel et al. 2002; Bromm & Larson 2004; Yoshida et al. 2008; Hosokawa et al. 2011; Stacy et al. 2011, 2012; Bromm 2013; Susa 2013; Susa et al. 2014; Hirano et al. 2015), they are short lived and located in the high-redshift universe. They can ultimately be observed only by large telescopes (e.g., Schauer et al. 2020). Although some Population III stars can form as low-mass and long-lived stars (Nakamura & Umemura 2001; Machida et al. 2008; Clark et al. 2011a, 2011b; Greif et al. 2011, 2012; Machida & Doi 2013; Susa et al. 2014; Chiaki et al. 2016), they have not yet been observed (Frebel & Norris 2015; Magg et al. 2018, 2019). Although extremely metal-poor (EMP) stars might be Population III stars metal-polluted by accreting interstellar medium (Komiya et al. 2015), many studies have suggested EMP stars are not polluted Population III stars, because such accretion can be blocked by stellar winds of low-mass Population III stars (Tanaka et al. 2017; Suzuki 2018). Interstellar asteroids cannot pollute Population III stars enough to become to EMP stars (Tanikawa et al. 2018; Kirihara et al. 2019).

In this paper, we predict properties of Population III BH–BHs to distinguish them from BH–BHs observed by current and future GW observatories. Although the current GW observatories can observe BH–BHs within a redshift (z) of $\lesssim 1$, future ground-based GW observatories, such as the Einstein telescope (Punturo et al. 2010; Maggiore et al. 2020) and Cosmic Explorer (Reitze et al. 2019), will detect BH–BHs up to $z \sim 10$. A future space-borne GW observatory, LISA (Amaro-Seoane et al. 2017), is expected to catch Population III BH–BHs (e.g., Sesana et al. 2009). Another space-borne GW observatory, DECIGO (Kawamura et al. 2006), can follow the cosmic evolution of BH–BHs and distinguish Population III BH–BHs (Nakamura et al. 2016).

So far, Kinugawa et al. (2014) have shown that Population III BH–BHs typically have $\sim 30M_{\odot}$, and Kinugawa et al. (2020) have shown its robustness against binary star evolution models. In this paper, we focus on the dependence of Population III BH–BHs on initial conditions and single star evolution models. Previous studies have assumed that Population III binaries can have initial separations comparable to their stellar radii at their zero-age main-sequence (ZAMS) times. In addition, we also consider Population III binaries with the minimum separation of $\sim 100R_{\odot}$. Population III binaries may not be initially compact, because Population III

stars can expand to $\gtrsim 100R_{\odot}$ at their protostellar phases (Stahler et al. 1986; Omukai & Palla 2001, 2003). Although previous studies have not taken into account stellar winds, we account for stellar winds, which are excited by stellar rotation (Yoon et al. 2012). Moreover, we set the maximum ZAMS mass to $300M_{\odot}$, while previous studies set it to $150M_{\odot}$. This maximum mass is reasonable according to recent numerical simulations (Hirano et al. 2014, 2015; Susa et al. 2014). Because such massive stars can overcome pair-instability supernovae (PISNe; Barkat et al. 1967; Fraley 1968; Bond et al. 1984; El Eid & Langer 1986; Fryer et al. 2001; Heger & Woosley 2002; Umeda & Nomoto 2002), we can get BHs with $\gtrsim 100M_{\odot}$. Eventually, we show properties of Population III BH–BHs with several $10M_{\odot}$ and $100M_{\odot}$, and discuss how to identify them from other BH–BHs using current and future GW observatories.

Belczynski et al. (2004) have investigated the formation of BH–BHs from Population III stars with $100\text{--}500M_{\odot}$. Due to the IMF, they have not investigated a BH–BH consisting of a BH overcoming PISN, and a BH not overcoming PISN. Moreover, studies of Population III stars have rapidly developed in this decade (see Dayal & Ferrara 2018 for review). We can reflect these achievements. Liu & Bromm (2020a) and Liu et al. (2021) have studied Population III BH–BHs formed by dynamical interactions. On the other hand, we focus on Population III BH–BHs formed through binary evolution. These studies should be complementary.

The structure of this paper is as follows. In Section 2, we describe our method. In Section 3, we show the calculation results. In Section 4, we consider how to identify Population III BH–BHs from other BH–BHs observed by current and future GW observatories. In Section 5, we discuss the effects we do not examine in Section 3. In Section 6, we summarize this paper.

2. Method

We perform calculations of binary population synthesis by means of the BSE code (Hurley et al. 2000, 2002) with extensions to very massive and EMP stars including Population III stars. In Sections 2.1 and 2.2, we present single and binary star models in our BSE code, respectively. In Section 2.3, we show our initial conditions of binaries. In Section 2.4, we describe parameter sets of our calculation runs. In Section 2.5, we give our Population III formation model to derive the merger rate of Population III BH–BHs.

2.1. Single Star Model

We use fitting formulae for stars with stellar metallicity $Z = 10^{-8}Z_{\odot}$ incorporated into BSE (Tanikawa et al. 2020c). The fitting formulae are based on simulation results of $Z = 10^{-8}Z_{\odot}$ stars from $8M_{\odot}$ to $1280M_{\odot}$ by means of the HOSHI code (Takahashi et al. 2016, 2018, 2019; Yoshida et al. 2019). They consist of luminosity (L), radius (R), helium (He) core mass ($M_{\text{c,He}}$), and carbon–oxygen (CO) core mass ($M_{\text{c,CO}}$) as functions of time and stellar mass (M). They follow the stellar evolutions from the ZAMS time to the carbon ignition time during which stars experience the main-sequence (MS), core He-burning (CHeB), and shell He-burning (ShHeB) phases. If stars lose their hydrogen (H) envelopes through stellar wind mass loss and binary interactions, we adopt the fitting formulae of naked He (nHe) stars derived in Hurley et al. (2000) for their luminosities and set $R = 0.2239(M_{\text{c,He}}/M_{\odot})^{0.62}R_{\odot}$ for their radii (Tout et al. 1997). Figure 1 shows the Hertzsprung–Russell diagram of $10^{-8}Z_{\odot}$ stars

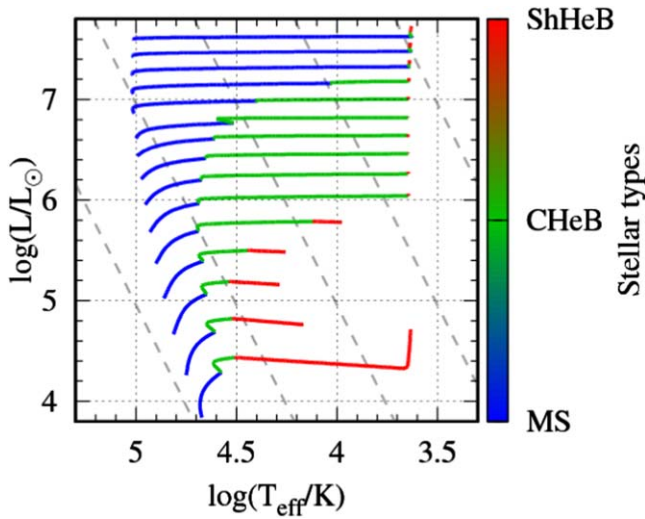


Figure 1. Hertzsprung–Russell diagram of $10^{-8} Z_{\odot}$ stars with $M = 10 at intervals of $2^{1/2}$ from bottom to top. Stellar winds are not taken into account. Gray dashed lines indicate stellar radii of $1, 10, 10^2, 10^3$, and $10^4 R_{\odot}$ from left to right. Colors indicate stellar phases: MS (blue), CHeB (green), and ShHeB (red).$

with $M = 10\text{--}1280 M_{\odot}$ at intervals of $2^{1/2}$, where we do not account for stellar winds. Stars with $10 \lesssim M/M_{\odot} \lesssim 50$ end their lives as blue-supergiant (BSG) stars with temperature of $\gtrsim 10^{3.65}$ K. Stars with $50 \lesssim M/M_{\odot} \lesssim 640$ become red-supergiant (RSG) stars when they are in their CHeB/ShHeB (or post-MS) phases. Stars with $M/M_{\odot} \gtrsim 640$ are still in their MS phases when they become RSG stars.

Tanikawa et al. (2020c) have devised the fitting formulae of stars with $M \leq 160 M_{\odot}$ and have compared the fitting formulae with detailed simulation results obtained by the HOSHI code. Here, we make similar comparisons for $M/M_{\odot} = 320, 640$, and 1280 in Figure 2. The luminosities and He core masses are in good agreement with each other. The He core masses of the fitting formulae grow later than those of the simulation results. This is because we assume the He core masses are zero when the stars are in their MS phases. The radii of the fitting formulae deviate from those of the simulation results in the middle of the evolution. However, these deviations should have small effects on binary evolutions, because the minimum and maximum radii for each MS, CHeB and ShHeB phase are consistent with each other. In particular, it is important that the maximum radii of stars (i.e., the maximum radii of the ShHeB phases) are consistent between the fitting formulae and simulation results. The maximum radii decide whether binary stars interact with each other or not.

We take into account stellar wind mass loss in postprocessing. The wind model is based on Belczynski et al. (2010) with the addition of a modified luminous-blue-variable (LBV) wind, and enhancement through stellar rotations. For no rotating stars, the stellar wind mass loss is expressed as

$$\dot{M}_{\text{wind}} = \begin{cases} \max(\dot{M}_{\text{NJ}}, \dot{M}_{\text{OB}}) & (\text{MS}) \\ \max(\dot{M}_{\text{NJ}}, \dot{M}_{\text{OB}}, \dot{M}_{\text{R}}, \dot{M}_{\text{WR}}, \dot{M}_{\text{LBV}}) & (\text{CHeB}) \\ \max(\dot{M}_{\text{NJ}}, \dot{M}_{\text{OB}}, \dot{M}_{\text{R}}, \dot{M}_{\text{WR}}, \dot{M}_{\text{LBV}}, \dot{M}_{\text{VW}}) & (\text{ShHeB}) \\ \max(\dot{M}_{\text{R}}, \dot{M}_{\text{WR}}) & (\text{nHe}) \end{cases} \quad (1)$$

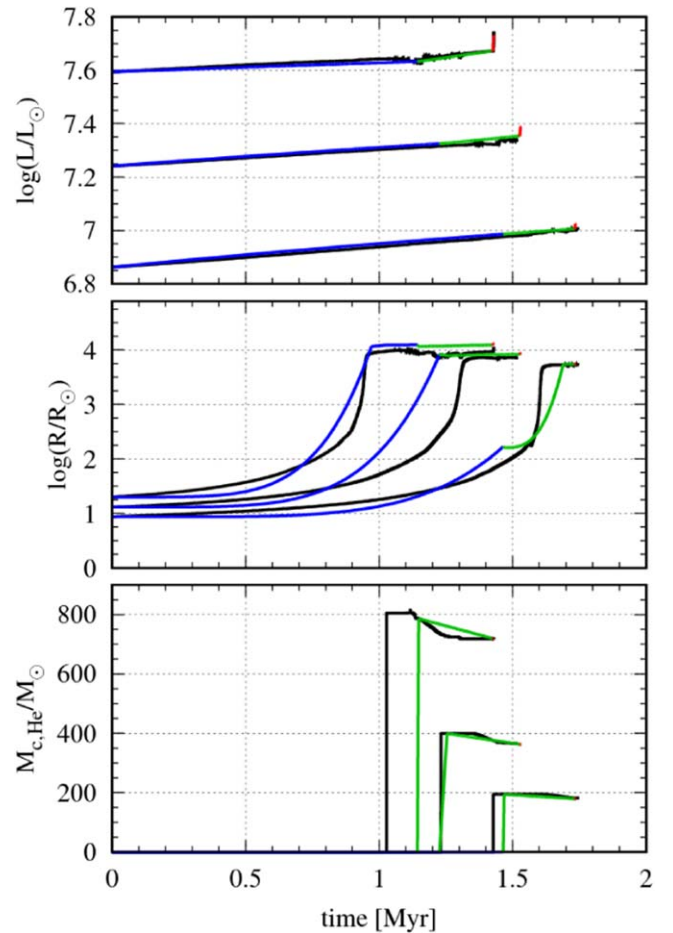


Figure 2. Time evolution of luminosities, radii, and He core masses for stars with $M = 320, 640$, and $1280 M_{\odot}$. Black curves indicate data of detailed simulations, and colored curves indicate our fitting formulae. The color codes are the same as in Figure 1. More massive stars have larger values for all the quantities.

where \dot{M}_{NJ} , \dot{M}_{OB} , \dot{M}_{R} , \dot{M}_{WR} , \dot{M}_{LBV} , and \dot{M}_{VW} are the mass-loss rates of luminous stars (Kudritzki et al. 1989; Nieuwenhuijzen & de Jager 1990), hot massive H-rich stars (Vink et al. 2001), giant-branch stars (Kudritzki & Reimers 1978; Iben & Renzini 1983), Wolf–Rayet stars (Hamann & Koesterke 1998; Vink & de Koter 2005), LBV stars (Humphreys & Davidson 1994), and asymptotic giant-branch (AGB) stars (Vassiliadis & Wood 1993). The expressions of \dot{M}_{NJ} , \dot{M}_{OB} , \dot{M}_{R} , \dot{M}_{WR} , and \dot{M}_{VW} are the same as Equations (56), (57), (58), (59), and (61) in Tanikawa et al. (2020c). We modify the expression of \dot{M}_{LBV} as

$$\frac{\dot{M}_{\text{LBV}}}{M_{\odot} \text{ yr}^{-1}} = \begin{cases} 1.5 \times 10^{-4} (Z/Z_{\odot})^{0.86} & (L > 6 \times 10^5 L_{\odot}, \text{ and } x_{\text{LBV}} > 1), \\ 0 & (\text{otherwise}), \end{cases} \quad (2)$$

where $x_{\text{LBV}} = 10^{-5} (R/R_{\odot}) (L/L_{\odot})^{0.5}$. The expression is the same as that of Belczynski et al. (2010) except for the metallicity dependence, and the metallicity dependence is the same as MOBSE2 (Giacobbo et al. 2018).

The stellar wind can be enhanced by stellar rotation. We include the enhancement as follows:

$$\dot{M}_{\text{wind,rot}} = \min [\dot{M}_{\text{wind}}(1 - v_{\text{rot}}/v_{\text{crit}})^{-0.43}, 0.1M/t_{\text{KH}}] \quad (3)$$

$$v_{\text{crit}} = \sqrt{GM(1 - L/L_{\text{Edd}})/R} \quad (4)$$

(Yoon et al. 2010, 2012; Takahashi et al. 2018), where G , v_{rot} , t_{KH} , and L_{Edd} are the gravitational constant, stellar surface rotation velocity, Kelvin–Helmholtz timescale, and Eddington luminosity, respectively. We adopt $L_{\text{Edd}} = 3.7 \times 10^4(M/M_{\odot})L_{\odot}$ for stars in the MS, CHeB, and ShHeB phases. We put an upper limit on L for nHe stars, such that $L \leq 0.99L_{\text{Edd}}$, where we adopt $L_{\text{Edd}} = 6.3 \times 10^4(M/M_{\odot})L_{\odot}$ for nHe stars. Note that the L_{Edd} of nHe stars is larger than that of MS, CHeB, and ShHeB stars due to the smaller opacity of electron scattering.

We put such an upper limit on the luminosities of nHe stars for the following reason. We infer the luminosity of nHe stars from our fitting formulae for ShHeB stars. Because a ShHeB star with $M = 320M_{\odot}$ has a He core with $180M_{\odot}$, and its luminosity is at most 10^7L_{\odot} (see Figure 2), a nHe star with $180M_{\odot}$ should have a luminosity of 10^7L_{\odot} . Thus, this nHe star should not exceed the Eddington luminosity of nHe stars. When we apply this inference to stars with various M , we find that nHe stars with $\lesssim 300M_{\odot}$ do not exceed the Eddington luminosity according to our fitting formulae. We have confirmed this inference by performing simulations of nonrotating nHe stars with 50, 100, 200, and $320M_{\odot}$ and a $200M_{\odot}$ star with the initial rotating velocity of $0.1v_k$, where $v_k = \sqrt{GM/R}$ is the Kepler velocity, with the HOSHI code. These stars do not exceed their Eddington limits and lose little mass through rotationally enhanced stellar winds. On the other hand, the fitting formulae of nHe stars in Hurley et al. (2000) are made from nHe star models with $M = 0.32\text{--}10M_{\odot}$, and nHe stars with $\gtrsim 100M_{\odot}$ exceed their Eddington luminosity. If we adopt this luminosity, we overestimate the rotationally enhanced mass loss. Hence, we constrain the luminosity of nHe stars, such that $L \leq 0.99L_{\text{Edd}}$.

Stars are assumed to experience supernovae or direct collapse immediately after the carbon ignition and leave stellar remnants like neutron stars (NSs) and BHs, or no remnants. We adopt the rapid model in Fryer et al. (2012) modified by pulsational pair instability (PPI; Heger & Woosley 2002; Woosley et al. 2007; Yoshida et al. 2016; Woosley 2017; Leung et al. 2019) and PISNe (Barkat et al. 1967; Fraley 1968; Bond et al. 1984; El Eid & Langer 1986; Fryer et al. 2001; Heger & Woosley 2002; Umeda & Nomoto 2002). Then, stellar remnant masses can be written as

$$M_{\text{rem}} = \begin{cases} M_{\text{rapid}} & (M_{\text{c,He}} \leq M_{\text{c,He,PPI}}) \\ M_{\text{c,He,PPI}} & (M_{\text{c,He,PPI}} < M_{\text{c,He}} \leq M_{\text{c,He,PISN}}) \\ 0 & (M_{\text{c,He,PISN}} < M_{\text{c,He}} \leq M_{\text{c,He,DC}}) \\ M_{\text{rapid}} & (M_{\text{c,He}} > M_{\text{c,He,DC}}), \end{cases} \quad (5)$$

and

$$\frac{M_{\text{rapid}}}{M_{\odot}} = \begin{cases} 1.2 & (M_{\text{c,CO}}/M_{\odot} \leq 2.5) \\ 0.286M_{\text{c,CO}} + 0.486 & (2.5 < M_{\text{c,CO}}/M_{\odot} \leq 6) \\ M_t & (6 < M_{\text{c,CO}}/M_{\odot} \leq 7) \\ M_t - M_{\text{ej}} & (7 < M_{\text{c,CO}}/M_{\odot} \leq 11) \\ M_t & (M_{\text{c,CO}}/M_{\odot} > 11) \end{cases} \quad (6)$$

$$\frac{M_{\text{ej}}}{M_{\odot}} = [0.25(M_t - 1) - 1.275](11 - M_{\text{c,CO}}). \quad (7)$$

Here, Equation (5) indicates the PPI/PISN corrections. The PPI/PISN corrections consist of four regimes: core-collapse supernovae (or direct collapse), PPI, PISNe, and direct collapse in ascending order of He core mass. We adopt the boundaries of these regimes, such that the minimum He core mass of PPI ($M_{\text{c,He,PPI}} = 45M_{\odot}$), the minimum He core mass of PISN ($M_{\text{c,He,PISN}} = 65M_{\odot}$), and the minimum He core mass of direct collapse ($M_{\text{c,He,DC}} = 135M_{\odot}$) are the same as in Belczynski et al. (2016b). We assume stars undergoing PPI leave BHs with masses of $M_{\text{c,He,PPI}}$. Equations (6) and (7) show the rapid model, where M_t is the total stellar mass. We regard stellar remnants as NSs and BHs if their masses are below and above $3M_{\odot}$, respectively. The lower mass limit of NSs is defined to be $1.2M_{\odot}$. If a stellar remnant has its mass of $< 1.2M_{\odot}$, it is a white dwarf; however, such a stellar remnant does not appear in this paper.

We account for a natal kick when massive stars leave NSs and BHs. The natal kicks are randomly oriented and have a Maxwellian velocity distribution with σ_k . We assume that σ_k does not depend on the remnant mass, contrary to the often-used prescription which attributes to higher-mass remnant a lower kick velocity. In this paper, NSs and BHs acquire the same kick as motivated in Section 2.4.

We model BH spins as follows. BH progenitors obtain and lose their spin angular momenta through single and binary evolutions, such as stellar winds, wind accretion, tidal interactions, Roche lobe overflow, and so on. Then, the spin vectors are always parallel to the binary orbit vectors. BH progenitors keep their spin angular momenta when they become BHs, except that they experience PPI. If BH progenitors experience PPI, we force the spins of their remnants to be zero, because these progenitors lose large amounts of masses. Frequently, the BH progenitors have spin angular momenta larger than those of extreme Kerr BHs. In this case, we force the spin parameters of their remnants to be unity and assume that the BH masses are equal to their progenitor masses. Although BHs can get spin angular momenta through mass transfer, we do not account for this process. In summary, we can express a normalized BH spin vector as follows:

$$\vec{\chi} = \begin{cases} \vec{0} & \text{if PPI} \\ \min(|\vec{S}|/(GM^2/c), 1)\vec{L}/|\vec{L}| & \text{otherwise,} \end{cases} \quad (8)$$

where c is the speed of light, \vec{S} is the spin angular momentum of a BH progenitor just before its collapse, and \vec{L} is the binary

orbit vector. Natal kicks can tilt $\vec{\chi}$ from \vec{L} as described in Section 2.2.

2.2. Binary Star Model

Because we use the BSE code, our binary star model is basically similar to that of Hurley et al. (2002) with some modifications. In this section, we briefly describe our binary star model.

Before describing our binary star model, we define the names of binary members. We call the heavier and lighter stars at their ZAMS times “first-evolving star” and “second-evolving star,” respectively, because the former evolves earlier than the latter. We attach subscripts of “1” and “2” to quantities to indicate first- and second-evolving stars, respectively. For example, masses of first- and second-evolving stars are m_1 and m_2 . We define the first and second BHs as BHs which the first- and second-evolving stars leave, respectively. The first BH is not always heavier than the second BH. We call the heavier and lighter BHs “primary BH” and “secondary BH,” respectively. We attach subscripts “p” and “s” to quantities to indicate primary and secondary BHs. Thus, the masses of primary and secondary BHs are $m_{b,p}$ and $m_{b,s}$, respectively.

We take into account wind accretion through which a star gets mass outflowing from its companion through stellar winds. In the original BSE code, the accretion rate is estimated as a Bondi–Hoyle mechanism (Bondi & Hoyle 1944) with an upper limit of a fraction of the mass-loss rate of the stellar winds. We find that the accretion rate sometimes exceeds the Eddington limit due to the presence of massive stellar winds and massive BHs. Thus, we put an upper limit on the wind accretion rate and set the limit to the Eddington limit expressed by Cameron & Mock (1967). Through stellar winds and wind accretion, stars lose and gain their spin angular momenta, and binaries change their semimajor axes and eccentricities. Our treatment for these processes is the same as that of the original BSE code.

Our prescriptions for tidal evolution are the same as the original BSE code. We adopt the equilibrium tide with convective damping for stars with convective envelopes, and the dynamical tide with radiative damping for stars with radiative envelopes. However, the difference between the original BSE code and our binary star model is which post-MS stars (here, CHeB and ShHeB stars) have which types of envelopes. In the original BSE code, CHeB and ShHeB stars have radiative and convective envelopes, respectively, where ShHeB stars are called AGB stars in the original BSE code. In our binary model, stars with $\log(T_{\text{eff}}/\text{K}) \geq 3.65$ and < 3.65 have radiative and convective envelopes, respectively. We need the above treatment, because CHeB stars can have convective envelopes, and ShHeB stars can have radiative envelopes in our single star model.

We also treat mass transfer in the same way as the original BSE code. If mass transfer is stable, a binary experiences stable mass transfer (or stable Roche-lobe overflow), and otherwise common-envelope evolution. Its stability strongly depends on whether a donor star has radiative or convective envelopes. If a donor star has a radiative (convective) envelope, mass transfer tends to be stable (unstable). We determine which post-MS stars have which types of envelopes in the same way as the case of tidal evolution described above. The common-envelope evolution is modeled as the α formalism (e.g., Webbink 1984). Thus, we have to decide on the common-envelope efficiency,

α_{CE} , and the structural binding energy parameter of a star, λ_{CE} . We set $\alpha_{\text{CE}} = 1$ and $\lambda_{\text{CE}} = 1$, if unspecified.

We consider orbital decay through GW radiation in the same way as the original BSE code. On the other hand, we switch off magnetic braking. It is difficult to expect the B -field configuration of Population III binaries. In the state-of-the-art Population III formation simulation (Sharda et al. 2020), the dominant component of the magnetic field is tangled. In such a case, the effect of magnetic braking is weak, so we omit the process.

BH spin vectors can be misaligned to binary orbit vectors due to natal kicks. We record angles between the BH spin and binary orbit vectors, where the binary orbit vectors are the ones when BH–BHs are formed. The angle between the second BH spin and binary orbit vectors (θ_2) can be decided only by the kick vector and binary parameters at the birth time. On the other hand, to determine the angle between the first BH spin and binary orbit vectors (θ_1), we need to know the differences between the binary phases at the birth times of the first and second BHs. Although we can know them, we choose the differences by Monte Carlo technique. Because binary periods are generally much smaller than the time intervals between the birth times, it is good approximation to choose the differences of phases randomly. Then, the angles θ_1 and θ_2 are given by

$$\cos \theta_1 = \vec{\chi}_1 \cdot \vec{L} / |\vec{L}|, \quad (9)$$

$$\cos \theta_2 = \vec{\chi}_2 \cdot \vec{L} / |\vec{L}|, \quad (10)$$

where the “.” operator means the inner product, $\vec{\chi}_1$ and $\vec{\chi}_2$ are the normalized BH spin vectors of the first and second BHs, respectively, and \vec{L} is the binary orbit vector of the final BH–BHs. Note that \vec{L} can be obtained from the natal kick velocity of the second BH and the binary parameter at its birth time as described above. We use the coordinate in which the z -axis is parallel to the binary orbit vector just before the second BH is born. Then, $\vec{\chi}_1$ and $\vec{\chi}_2$ can be written as

$$\vec{\chi}_1 = (\sin \theta'_1 \cos \phi'_1, \sin \theta'_1 \sin \phi'_1, \cos \theta'_1), \quad (11)$$

$$\vec{\chi}_2 = (0, 0, 1), \quad (12)$$

where θ'_1 is the angle between the first BH spin vector and binary orbit vector just before the second BH is born, and ϕ'_1 is randomly chosen between 0 and 2π . The spin vector of the second BH should be parallel to the binary orbit vector just before its birth, because we do not account for spin–orbit misalignment mechanism other than natal kicks. Note that θ'_1 can be determined by the natal kick vector of the first BH and binary parameters at the birth time of the first BH.

2.3. Initial Conditions

To generate a bunch of binaries, we set the distribution of the first-evolving star’s masses ($m_{1,i}$), mass ratios of the second-evolving stars to first-evolving stars ($q_i = m_{2,i}/m_{1,i}$), semimajor axes (a_i), and eccentricities (e_i) at the initial time as follows. The distribution of $m_{1,i}$ is given by

$$f(m_{1,i}) \propto m_{1,i}^{-1} (10 \leq m_{1,i}/M_{\odot} \leq 300). \quad (13)$$

This is based on the logarithmically flat mass distribution of Population III stars in the range from about $10M_{\odot}$ to several $100M_{\odot}$ (Hirano et al. 2014, 2015; Susa et al. 2014). Note that

although we set the maximum mass to $300M_{\odot}$, the maximum mass can be smaller (e.g., Tarumi et al. 2020).

We set the distribution of q_i , such that

$$f(q_i) \propto \text{const} (q'_{\min} \leq q_i \leq 1), \quad (14)$$

$$q'_{\min} = \max(q_{\min}, 10M_{\odot}/m_{1,i}). \quad (15)$$

The second equation means that the minimum mass of second-evolving star is $10 M_{\odot}$, the same as the minimum mass of first-evolving stars. We determine q_{\min} in Section 2.4.

The average mass of binaries at the initial time, $\langle m_{\text{bin},i} \rangle$, can be calculated as

$$\begin{aligned} \frac{\langle m_{\text{bin},i} \rangle}{M_{\odot}} &= \int_{10}^{300} dm_{1,i} f(m_{1,i}) \int_{q_{\min}}^1 dq_i f(q_i) m_{1,i} (1 + q_i) \\ &\sim 43(3 + q_{\min}). \end{aligned} \quad (16)$$

The semimajor axis distribution can be written as

$$f(a_i) \propto a_i^{-1} (a'_{\min} \leq a_i/R_{\odot} \leq 2000) \quad (17)$$

$$a'_{\min} = \max \left[a_{\min}, \frac{0.6q_i^{2/3} + \log(1 + q_i^{1/3})}{0.49q_i^{2/3}} R_{1,i}/R_{\odot} \right], \quad (18)$$

where $R_{1,i}$ is the initial radius of the first-evolving star. The maximum value $2000R_{\odot}$ can be obtained from the simulation results in Figure 5 in M. Arimoto et al. (2020, in preparation). The maximal final semimajor axis of the binaries at $\gtrsim 2 \times 10^4$ yr is ~ 10 au, after which the radiative feedback quenches further gas accretion. This is a spatially coarse calculation, thus this could be used as the upper bound of the separation of Population III binaries. Owing to the second equation, binaries can avoid Roche-lobe overflow from the beginning. We choose a_{\min} in Section 2.4.

The eccentricity distribution is the thermal distribution with modification as

$$f(e_i) \propto e_i (0 \leq e_i \leq e_{\max}), \quad (19)$$

$$e_{\max} = 1 - a'_{\min}/a_i. \quad (20)$$

The modification makes the pericenter distance larger than a'_{\min} at the initial time. Note that $e_{\max} = 1$ if the eccentricity distribution is completely thermal.

Each star has nearly no rotation at the initial time.

2.4. Parameter Sets

We prepare a bunch of parameter sets summarized in Table 1. We mainly focus on 16 parameter sets (hereafter, the 16 main models) in which we consider non- and $Z = 10^{-3}Z_{\odot}$ stellar winds, and $\sigma_k = 0, 265 \text{ km s}^{-1}$, $q_{\min} = 0.0, 0.9$, and $a_{\min} = 10, 200R_{\odot}$. We suppose that these stellar winds are weak and strong extremes. The natal kick velocities of $\sigma_k = 0$ and 265 km s^{-1} are also weak and strong extremes. We adopt $\sigma_k = 265 \text{ km s}^{-1}$, obtained in Hobbs et al. (2005). We set $q_{\min} = 0.0$ and 0.9 . We can get a variety of mass combinations for $q_{\min} = 0.0$, while we restrict the mass combinations for $q_{\min} = 0.9$ due to the fact that the mass ratios of binaries tend to be close to unity (Susa 2019). We use $a_{\min} = 200R_{\odot}$, because Population III stars can expand to $\gtrsim 100R_{\odot}$ at their protostellar phases (Stahler et al. 1986; Omukai & Palla 2001, 2003), and binaries with $a \lesssim 100R_{\odot}$ can merge before they enter into their MS phases. Nevertheless, we also

Table 1
Summary of Parameter Sets

Model	Wind	σ_k	q_{\min}	a_{\min}
optiq0.0a1e1	w/o	0	0.0	10
optiq0.0a2e2	w/o	0	0.0	200
optiq0.9a1e1	w/o	0	0.9	10
optiq0.9a2e2	w/o	0	0.9	200
kickq0.0a1e1	w/o	265	0.0	10
kickq0.0a2e2	w/o	265	0.0	200
kickq0.9a1e1	w/o	265	0.9	10
kickq0.9a2e2	w/o	265	0.9	200
windq0.0a1e1	$10^{-3}Z_{\odot}$	0	0.0	10
windq0.0a2e2	$10^{-3}Z_{\odot}$	0	0.0	200
windq0.9a1e1	$10^{-3}Z_{\odot}$	0	0.9	10
windq0.9a2e2	$10^{-3}Z_{\odot}$	0	0.9	200
pessq0.0a1e1	$10^{-3}Z_{\odot}$	265	0.0	10
pessq0.0a2e2	$10^{-3}Z_{\odot}$	265	0.0	200
pessq0.9a1e1	$10^{-3}Z_{\odot}$	265	0.9	10
pessq0.9a2e2	$10^{-3}Z_{\odot}$	265	0.9	200
half-kick	w/o	130	0.0	10
weak-wind	$10^{-5}Z_{\odot}$	0	0.0	10
no-rot-wind	$10^{-3}Z_{\odot}$	0	0.0	10
K14	w/o	0	0.0	0

Note. The units of σ_k and a_{\min} are km s^{-1} and R_{\odot} , respectively. In the wind column, the metallicity adopted for our wind model is described. In the “no-rot-wind” model, we do not account for rotationally enhanced stellar winds, $\dot{M}_{\text{wind,rot}}$. In the “K14” model, we set the $m_{1,i}$ distribution as $f(m_{1,i}) \propto \text{const} (10 \leq m_{1,i}/M_{\odot} \leq 100)$ and do not take into account PPI effects.

choose $a_{\min} = 10R_{\odot}$. This is because they may avoid their mergers for unknown reasons. In fact, the evolution of the protostellar radius in the protobinary system is not known, although only a single star evolution has been investigated so far assuming spherically symmetric mass accretion (Stahler et al. 1986; Omukai & Palla 2001, 2003). It is also worth noting that such close binaries with $a \lesssim 100R_{\odot}$ may be formed through dynamical processes after they enter into their MS phases. The model names are named w/ and w/o wind, w/ and w/o kick, and the values of q_{\min} and a_{\min} . “Opti” and “pess” stand for “optimistic” and “pessimistic,” respectively. The “opti” and “pess” models are thought to form large and small numbers of merging BH–BHs, respectively.

Note that the natal kick velocities are smaller for larger remnant masses in the prescription that is usually adopted in the literature. However, we do not adopt this prescription here. In the commonly used prescription, kick velocities are set to $\sigma_k(M_{\text{rem}}/M_{\text{rem},0})^{-1}$, where $\sigma_k = 265 \text{ km s}^{-1}$ and $M_{\text{rem},0} = 3.0M_{\odot}$ (e.g., Wang et al. 2016). BHs with $\sim 10M_{\odot}$ receive kick velocities of $\sim 80 \text{ km s}^{-1}$. On the other hand, BH–BHs with two $\sim 10M_{\odot}$ BHs have orbital velocities of $\gtrsim 400 \text{ km s}^{-1}$ if they merge within a Hubble time. Thus, such BH natal kicks have small effects on merging BH–BHs within the Hubble time. The effects becomes smaller for more massive BHs. Even if we adopt the usual prescription, we get similar results to those of models without BH natal kicks. Moreover, the usual prescription may be hard to explain several X-ray binaries with BHs (Willems et al. 2005; Wong et al. 2012; Repetto & Nelemans 2015; Mandel 2016; Repetto et al. 2017; Gandhi et al. 2019, 2020). The spin–orbit misalignment of GW190412 needs natal kicks of several 100 km s^{-1} , if GW190412 is formed through binary evolution (Olejak et al. 2020;

Safarzadeh & Hotokezaka (2020). There are several theoretical studies for natal kicks with high velocities (Barkov & Komisarov 2010; Batta & Ramirez-Ruiz 2019).

Additionally, we make four parameter sets. For the “half-kick” model, we investigate the dependence of the BH–BH populations on natal kick velocities. We examine effects of metallicity and rotational enhancement on stellar winds, investigating the “weak-wind” and “no-rot-wind” models, respectively. In order to compare our results with results in Kinugawa et al. (2020), we prepare the K14 model, which has initial condition and single/binary star models similar to the K14 model in Kinugawa et al. (2020).

For each parameter set, we follow the time evolutions of 10^6 binaries until 100 Gyr. The initial conditions of 10^6 binaries are the same if q_{\min} and a_{\min} are identical. For each parameter set, we spend 1–2 hr calculating on 1 CPU core of an Intel Core i9-7980XE CPU with turbo boost enabled.

2.5. Population III Formation Model

In this paper, we adopt the Population III formation model as follows. All Population III stars are formed in mini halos at the same time. Only one Population III binary is born in one mini halo, $\eta_{\text{bin}} = 1$. The number density of the mini halos is $n_{\text{DM}} = 10^{11} \text{ Gpc}^{-3}$. Then, the number density of Population III binaries is 10^{11} Gpc^{-3} . Using Equation (16), we can obtain the mass density of Population III binaries to be $1.3 \times 10^{13} M_{\odot} \text{ Gpc}^{-3}$ for $q_{\min} = 0.0$ and $1.7 \times 10^{13} M_{\odot} \text{ Gpc}^{-3}$ for $q_{\min} = 0.9$. Our mass density is a fraction of the Population III star density of $\sim 10^{14} M_{\odot} \text{ Gpc}^{-3}$ (see Figure 2 of Magg et al. 2016) and $\sim 3 \times 10^{13} M_{\odot} \text{ Gpc}^{-3}$ (see Figure 4 of Skinner & Wise 2020). On the other hand, our mass density is smaller than in Kinugawa et al. (2020) by two orders of magnitude. They have estimated the Population III mass density from the results of de Souza et al. (2011) modified by the argument of Inayoshi et al. (2016). We interpret that our formation rate is the lower limit.

According to Magg et al. (2016), Population III stars stop forming at $z \sim 5$, or at the lookback time of ~ 12.5 Gyr. Thus, Population III BH–BHs that merge in the local universe should have the delay time of ~ 12.5 – 13.8 Gyr. Note that the upper bound should be less than 13.8 Gyr, because Population III stars are not formed at the beginning of the universe. However, we assume that Population III BH–BHs with the delay time of ~ 10 – 15 Gyr merge in the local universe. This assumption enables us to obtain many Population III BH–BHs from our binary population synthesis calculations and investigate their mass and spin distributions in the local universe.

3. Results

We describe the results of binary population synthesis calculations. In Section 3.1, we show the relation between ZAMS and remnant masses through single star evolution. It is instructive to investigate the dependence of the relation on stellar winds. In Section 3.2, we compare our results with those of Kinugawa et al. (2020), examining the K14 model. In Section 3.3, we present populations of merging Population III BH–BHs.

3.1. Single Star Evolution

In Figure 3, we show the relation between ZAMS and remnant masses. The maximum ZAMS mass is $600M_{\odot}$, which is the possible maximum mass of binaries in our calculations.

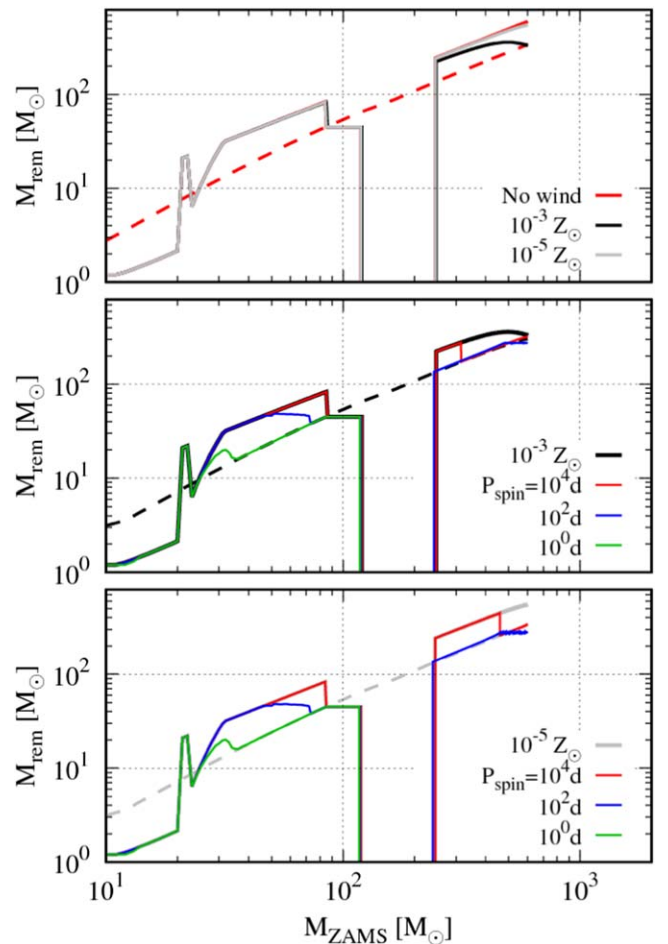


Figure 3. Relation between ZAMS and remnant masses. In the top panel, stars receive no wind (red), $10^{-3} Z_{\odot}$ winds (black), and $10^{-5} Z_{\odot}$ winds (gray). The stars receive no wind, or winds without $\dot{M}_{\text{wind,rot}}$. In the middle and bottom panels, stars receive winds with $Z = 10^{-3}$ and $10^{-5} Z_{\odot}$, respectively. The black and gray curves in the middle and bottom panels are identical to those in the top panel, respectively. In the middle and bottom panels, stars receive winds with $\dot{M}_{\text{wind,rot}}$ except for the stars indicated by the black and gray curves. They are forced to keep stellar rotations with periods of 10^4 days (red), 10^2 days (blue), and 1 day (green). As guides, He core masses are indicated by the dashed curves in stars receiving no wind (top), $10^{-3} Z_{\odot}$ winds without $\dot{M}_{\text{wind,rot}}$ (middle), and $10^{-5} Z_{\odot}$ winds without $\dot{M}_{\text{wind,rot}}$ (bottom).

Moreover, a star with this maximum ZAMS mass creates a He core with $\sim 300M_{\odot}$ and can form a nHe star with $\sim 300M_{\odot}$. As described in Section 2.1, we confirm that our stellar wind model is valid for nHe stars with $\lesssim 300M_{\odot}$. We can see the metallicity dependence without $\dot{M}_{\text{wind,rot}}$ in the top panel and the dependence on stellar rotation speeds for $Z = 10^{-3}$ and $10^{-5} Z_{\odot}$ in the middle and bottom panels, respectively. We forcibly fix the stellar rotation periods for stars in the middle and bottom panels. There are two reasons for this treatment. First, we simply attempt to investigate effects of stellar rotations on stellar wind mass loss. Second, stars could keep their rotation periods when they are synchronized with binary motions.

We first focus on the top panel. For any winds without $\dot{M}_{\text{wind,rot}}$, stars with $M_{\text{ZAMS}} \lesssim 20M_{\odot}$ and $\gtrsim 20M_{\odot}$ leave NSs and BHs, respectively. We can see that BH masses decrease at $M_{\text{ZAMS}} \sim 25M_{\odot}$, which is a feature of the rapid model we adopt (see Equation (6) in detail). Stars with $M_{\text{ZAMS}} \sim 90$ – $120M_{\odot}$ have $45M_{\odot}$ BHs due to the PPI effect, stars with $M_{\text{ZAMS}} \sim 120$ – $250M_{\odot}$

leave no remnant due to the PISN effect, and stars with $M_{\text{ZAMS}} \gtrsim 250M_{\odot}$ undergo direct collapse to BHs. PPI/PISN effects make “the PI mass gap” from $45M_{\odot}$ to $135M_{\odot}$. Nevertheless, some of the stars can have BHs in the PI mass gap. Their maximum mass is $\sim 85M_{\odot}$. They can avoid PPI/PISN effects due to small He core masses and can grow to $>45M_{\odot}$ owing to massive H envelopes. For $M_{\text{ZAMS}} \lesssim 250M_{\odot}$, the relation has weak dependence on metallicity. For $M_{\text{ZAMS}} \gtrsim 250M_{\odot}$, stars receiving $10^{-3}Z_{\odot}$ winds leave BHs with distinctly smaller masses than the other cases. This is due to luminous-star winds (\dot{M}_{NJ}).

In the middle panel, we find that the boundary between NSs and BHs, as well as the PPI/PISN effects, is similar to the case of winds without $\dot{M}_{\text{wind,rot}}$. For $M_{\text{ZAMS}} \lesssim 120M_{\odot}$, BH masses become smaller as rotation periods become smaller. Stars with rotation periods of 10^4 days keep their H envelopes to the ends of their lives. On the other hand, stars with rotation periods of 1 and 100 days become nHe stars when their ZAMS masses are $M_{\text{ZAMS}} \gtrsim 35M_{\odot}$ and $\gtrsim 70M_{\odot}$, respectively. For $M_{\text{ZAMS}} \gtrsim 250M_{\odot}$, stars with smaller periods also leave BHs with smaller masses. For periods of 1 day, stars undergo PISNe and leave no remnants, because they lose large amounts of masses in their MS phases and create their He core with $65\text{--}135M_{\odot}$ entering into their CHeB phases. For periods of 10^2 days, they become nHe stars. For periods of 10^4 days, BH masses suddenly decrease at $M_{\text{ZAMS}} \sim 300M_{\odot}$. Stars with $M_{\text{ZAMS}} \lesssim 300M_{\odot}$ keep their H envelopes, while those with $M_{\text{ZAMS}} \gtrsim 300M_{\odot}$ become nHe stars. This is because the luminosities of the latter stars exceed their Eddington limit in the middle of their evolution. Thus, they lose large amounts of their mass and become nHe stars.

In many cases, we can see that stars lose large amounts of mass in the MS, CHeB, and ShHeB phases, and stop losing mass in the nHe phases. This is because the Eddington luminosity is increased from the former phases to the latter phase. Then, rotationally enhanced mass loss becomes inactive when stars become nHe stars.

We find that the relations are weakly dependent on metallicity when $\dot{M}_{\text{wind,rot}}$ is taken into account (see the middle and bottom panels). Nevertheless, for rotation periods of 10^4 days, BH masses suddenly decrease at different M_{ZAMS} : $M_{\text{ZAMS}} \sim 300M_{\odot}$ for $Z = 10^{-3}Z_{\odot}$, and $M_{\text{ZAMS}} \sim 450M_{\odot}$ for $Z = 10^{-5}Z_{\odot}$. It is harder for stars with $Z = 10^{-5}Z_{\odot}$ to lose mass than those with $Z = 10^{-3}Z_{\odot}$, because they have larger masses, i.e., a larger Eddington limit, owing to slightly weaker stellar winds.

3.2. Comparison with K14

We describe the calculation results of our K14 model to compare them with the K14 model in Kinugawa et al. (2020; hereafter the original K14 model). Figure 4 shows the chirp mass distribution of merging BH–BHs within 15 Gyr in our K14 model. Hereafter, we use 15 Gyr as the Hubble time, because it is just a round number. The chirp mass of BH–BHs can be expressed as

$$m_{\text{chirp}} = \frac{(m_{\text{b,p}} m_{\text{b,s}})^{3/5}}{(m_{\text{b,p}} + m_{\text{b,s}})^{1/5}}, \quad (21)$$

where $m_{\text{b,p}}$ and $m_{\text{b,s}}$ are the primary and secondary BH masses of BH–BHs. We find that it is quite consistent with the results of the original K14 model (see the purple curve in their Figure 3). Both K14 models have sharp peaks at $m_{\text{chirp}} \sim 30M_{\odot}$. Our K14 model has a sharp drop at $m_{\text{chirp}} \sim 60M_{\odot}$, while the original K14 model

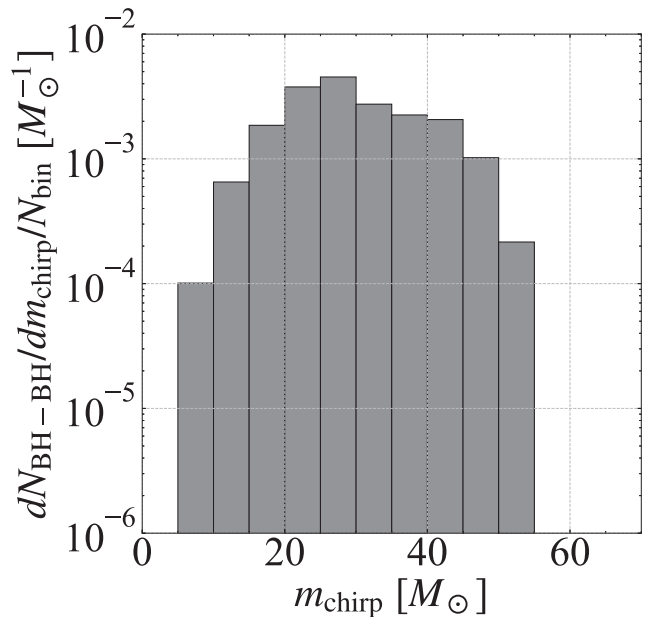


Figure 4. Chirp mass distribution of merging BH–BHs within 15 Gyr in our K14 model. The number of merging BH–BHs ($N_{\text{BH–BH}}$) is normalized by the total number of binaries, $N_{\text{bin}} = 10^6$.

has it at $m_{\text{chirp}} \sim 80M_{\odot}$. This comes from the different treatments of H envelopes of post-MS stars whose H envelopes are almost stripped. If the treatments are the same, the sharp drop is at $m_{\text{chirp}} \sim 60M_{\odot}$ even in the original K14 model (see the light-blue curve in Figure 1 in Kinugawa et al. 2016a). We emphasize that these agreements are very surprising. This is because we both use fitting formulae of Population III stars based on different stellar evolution models (Marigo et al. 2001; Tanikawa et al. 2020c, respectively). These results reinforce the argument of Kinugawa et al. (2014) that typical Population III BH–BH mergers have $\sim 30M_{\odot}$ BHs.

We can see the delay time (t_d) distribution of BH–BHs in our K14 model in Figure 5, where t_d is the delay time, or defined as the time interval from the ZAMS time to the BH–BH merger time. The black curve indicates the distribution of all BH–BHs, while the other curves indicate the distribution of BH–BHs formed through the CE0, CE1, CE2, CE3, and CE4 channels. In the CE0 channel, binary systems experience no common-envelope evolution. In the CE1 and CE2 channels, they undergo common-envelope evolution, ejecting the H envelopes of the first- and second-evolving stars, respectively. In the CE3 channel, they have both CE1 and CE2 channels. In the CE4 channel, they go through common-envelope evolution, ejecting the H envelopes of both the first- and second-evolving stars at the same time.

The delay time distribution of all the BH–BHs is similar to the original K14 model (see the purple curve in their Figure 4). Note that their values in the vertical axis are six digits larger than ours, because they do not normalize the number of BH–BHs by the total number of binaries. The number of mergers sharply increase at several Myr and gradually decrease until several 10 Myr. After that, the number starts to rise and reaches to a few 10^{-3} at 10 Gyr.

We recognize common and different features, comparing the delay time distribution of BH–BHs formed through each channel (see their Figure 5(e)). The common feature is that the

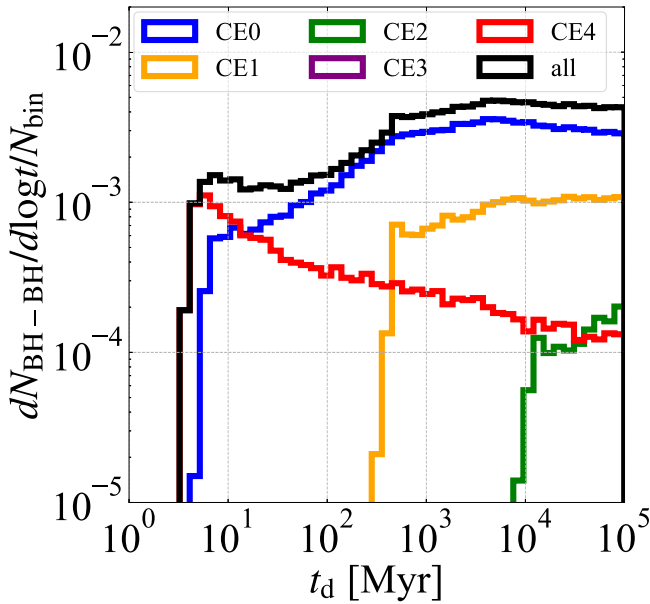


Figure 5. Delay time distribution of BH–BHs in our K14 model. The normalization is the same as in Figure 4. The black curve indicates the distribution of all BH–BHs. All colored curves indicate that BH–BHs formed through channels related to common-envelope evolutions defined in the main text. There is no BH–BH formed through the CE3 channel.

dominant channels are CE4 and CE0 at earlier and later times than a few 10 Myr, respectively. Another common feature is the distribution of BH–BHs formed through the CE1 channel. The BH–BHs start forming from $\sim 10^2$ Myr, and their number remains at $\sim 10^{-3}$ after that.

The number of BH–BHs formed through the CE2 and CE3 channels in our K14 model is much smaller than in the original K14 model. This is because our fitting formulae for single star models have larger He core masses than theirs (see Figure 6). As the ratios of He core masses to stellar masses become larger, common-envelope evolution is harder to happen. Although He core masses in our fitting formulae are smaller than those of Kinugawa for $M_{\text{ZAMS}} \gtrsim 130M_{\odot}$, stars with $M_{\text{ZAMS}} \gtrsim 130M_{\odot}$ have a small chance of going through the CE2 and CE3 channels in both the K14 models.

Figure 7 shows the delay time distribution of BH–BHs with effective spins, χ_{eff} . The definition of χ_{eff} is given by

$$\chi_{\text{eff}} = \left(\frac{m_{\text{b,p}} \vec{\chi}_{\text{p}} + m_{\text{b,s}} \vec{\chi}_{\text{s}}}{m_{\text{b,p}} + m_{\text{b,s}}} \right) \cdot \frac{\vec{L}}{|\vec{L}|}, \quad (22)$$

where $\vec{\chi}_{\text{p}}$ and $\vec{\chi}_{\text{s}}$ are the normalized spin vectors of the primary and secondary BHs. We are going to make a comparison between the χ_{eff} evolution in both K14 models. However, we should note that we cannot strictly compare Figure 7 with the χ_{eff} evolution shown in the original K14 model (see their Figure 7(e)). We assume that all stars are instantaneously born at $t = 0$, while they adopt a Population III star formation history in which Population III stars have a wide range of formation times. In addition, the horizontal axes of our and their figures are time and redshift, respectively.

There are several common features. We find that BH–BHs with $0.8 < \chi_{\text{eff}} < 1.0$ are always dominant in both the results. When we compare the numbers at 10 Gyr in our K14 model with those at $z = 0$ in the original K14 model, BH–BHs with $\chi_{\text{eff}} < 0.8$ have

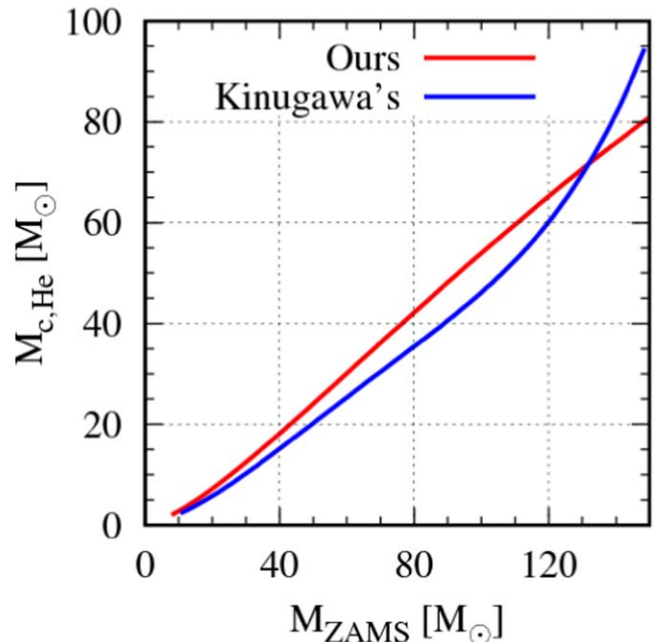


Figure 6. Relation between ZAMS and He core masses at the carbon ignition time in the fitting formulae of Kinugawa et al. (2020, blue) and Tanikawa et al. (2020c, red).

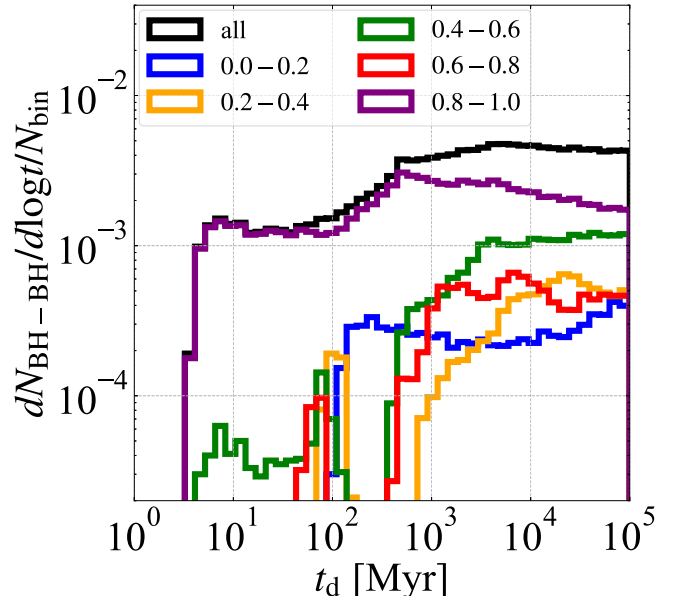


Figure 7. Delay time distribution of BH–BHs in our K14 model. The normalization is the same as in Figure 4. The black curve indicates the distribution of all BH–BHs. Other curves indicate the distribution of BH–BHs with effective spins (χ_{eff}) described in the legend. The definition of χ_{eff} is in the main text.

significant contributions to the numbers in both K14 models. However, the numbers are quite different at an early time. In our K14 model, only BH–BHs with $0.8 < \chi_{\text{eff}} < 1.0$ merge at time $< 10^2$ Myr. On the other hand, BH–BHs with $0.4 < \chi_{\text{eff}} < 0.6$ and $0.8 < \chi_{\text{eff}} < 1.0$ have comparable contributions in the original K14 model. These differences can be explained by the difference between spin models. In our model, BHs keep their spin angular momenta even when they lose their mass at their collapse. On the other hand, in the original K14 model, BHs lose their spin angular

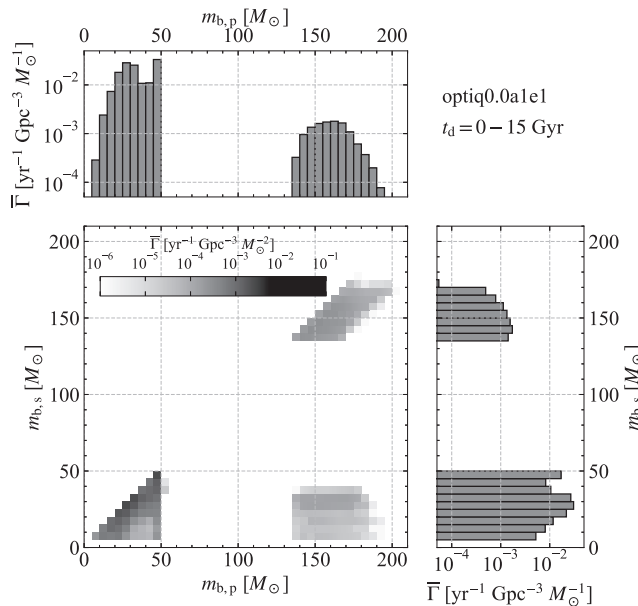


Figure 8. Average merger rate density of BH–BHs for $t_d = 0-15$ Gyr.

momenta. Nevertheless, the spin distributions in both K14 models are consistent in the current universe.

3.3. Merging BH–BHs

Figure 8 shows the average merger rate density of BH–BHs for $t_d = 0-15$ Gyr in the optiq0.0a1e1 model. We define the merger rate density as

$$\Gamma = \frac{d(N_{\text{BH-BH}}/N_{\text{bin}})}{dt_d} \left(\frac{\eta_{\text{bin}}}{1} \right) \left(\frac{n_{\text{DM}}}{10^{11} \text{ Gpc}^{-3}} \right) \times [\text{yr}^{-1} \text{ Gpc}^{-3}]. \quad (23)$$

As seen in the above formula, the average merger rate density is defined in the local comoving volume at the source frame time. Using Equation (23), we can express the average merger rate density as

$$\bar{\Gamma} = \frac{1}{t_{\text{d,f}} - t_{\text{d,i}}} \int_{t_{\text{d,i}}}^{t_{\text{d,f}}} \Gamma dt_d, \quad (24)$$

where $t_{\text{d,i}}$ and $t_{\text{d,f}}$ are the beginning and ending times for the averaging.

We can clearly see that there are three subpopulations of BH–BHs: those with two low-mass BHs (IBHs), those with one IBH and one high-mass BH (hBH), and those with two hBHs, where we call BHs with $\lesssim 50M_\odot$ “IBHs,” and BHs with $\gtrsim 130M_\odot$ “hBHs.” There is a large mass gap between IBHs and hBHs due to PPI/PISN effects, the PI mass gap, as seen also in Figure 3. The mass gap ranges from $\sim 50M_\odot$ to $\sim 130M_\odot$. Hereafter, we name BH–BHs with two IBHs, those with one IBH and one hBH, and those with two hBHs “hBH0,” “hBH1,” and “hBH2,” respectively, after the number of hBHs. The mass ranges of IBHs and hBHs are quite different; the maximum mass of IBHs is $\sim 50M_\odot$, and the minimum mass of hBHs is $\sim 135M_\odot$. Stars with $M_{\text{c,He}} < 45M_\odot$ and H envelopes can leave $>45M_\odot$ BHs avoiding PPI, and leave BHs with $\sim 50M_\odot$ at most. Thus, we can identify hBH0, hBH1, and hBH2 as distinct subpopulations.

In Figure 9, we show the merger rate density of hBH0, hBH1, and hBH2 as a function of t_d in the 16 main models. The merger

rate densities are not necessarily proportional to t_d^{-1} . Some of the merger rate densities suddenly increase, because the dominant formation channels of BH–BHs are switched. For example, for the hBH2s of the optiq0.0a2e2 model, the dominant formation channels switch from CE4 to CE0 at $t_d \sim 10$ Gyr. For $t_d \lesssim 0.1$ Gyr, some of the merger rate densities decrease more slowly than t_d^{-1} . This is because a part of BH–BH progenitors with $t_d \gtrsim 0.1$ Gyr shrink their orbits due to mechanisms other than common-envelope evolutions. One mechanism is BH natal kicks. We can see that BH natal kicks yield hBH1s with $t_d \lesssim 0.1$ Gyr, since the kickq0.0a1e1 model has hBH1s with $t_d \sim 0.1$ yr, while the optiq0.0a1e1 model does not. Another mechanism is stable mass transfer in which the mass ratio of a donor star to an accretor star is sufficiently larger than unity. This can sometimes strip the H envelopes of post-MS stars. This can be seen in the hBH0s of the optiq0.0a1e1 model.

In the present day (~ 10 Gyr), the merger rates of hBH0s are $\sim 0.1 \text{ yr}^{-1} \text{ Gpc}^{-3}$, independently of single star models; q_{\min} ; and a_{\min} . This is much smaller than the merger rate density inferred by LIGO/Virgo observations, $\sim 10-100 \text{ yr}^{-1} \text{ Gpc}^{-3}$ (Abbott et al. 2019). Although this is smaller than estimated by Kinugawa et al. (2020) by two orders of magnitude, this is consistent with their results, because the total Population III mass in our model is smaller than theirs by two orders of magnitude (see Section 2.5). If our formation model is close to the actual formation rate, we may not expect that Population III hBH0s are a dominant origin of the GW sources discovered recently. However, it should be worth examining properties of Population III hBH0s for the following reason. It is important to identify Population III hBH0s with respect to the star formation history in the universe, and moreover future GW observatories, such as the Einstein Telescope (Punturo et al. 2010; Maggiore et al. 2020) and Cosmic Explorer (Reitze et al. 2019), may detect a large number of Population III hBH0s.

We also inspect hBH1s and hBH2s for the following reason. María Ezquiaga & Holz (2021) have shown that hBH1s and hBH2s can be detected by current GW observatories if they merge within detectable distances, although they have not yet been detected. Moreover, space-borne GW observatories, such as LISA and DECIGO (Kawamura et al. 2006; Amaro-Seoane et al. 2017, respectively), may be helpful in searching for merging hBHs. LISA especially, will detect hBHs months to years before hBH mergers in the local universe (Sesana 2016).

Before we examine hBH0s, hBH1s, and hBH2s separately, we investigate their initial conditions and formation channels. By this, we make clear the reason why the merger rates of hBH0s and the sum of hBH1s and hBH2s do not depend on initial conditions and single star models. First, we mainly focus on the dependence on initial conditions. Second, we mention the dependence on single star models.

Figure 10 shows the initial conditions of Population III binaries which form BH–BHs merging within 15 Gyr for the optiq0.0a1e1 model. We separate the initial conditions into two panels depending on whether $q_i < 0.9$ or $q_i \geq 0.9$, and mark an initial pericenter distance ($r_{\text{p},i}$) of $200R_\odot$ by vertical dashed lines, so as to imagine results of models with $q_{\min} = 0.9$ and $a_{\min} = 200R_\odot$. We can see a gap between $m_{1,i} \sim 120-250M_\odot$ in which BH–BHs are not formed. This is due to PISN effects. All hBH0s are under this gap, and all hBH1s and hBH2s are above this gap. In other words, binaries with first-evolving stars with $m_{1,i} \lesssim 120M_\odot$ can only form hBH0s, and binaries with first-evolving stars with $m_{1,i} \gtrsim 250M_\odot$ can only form hBH1s

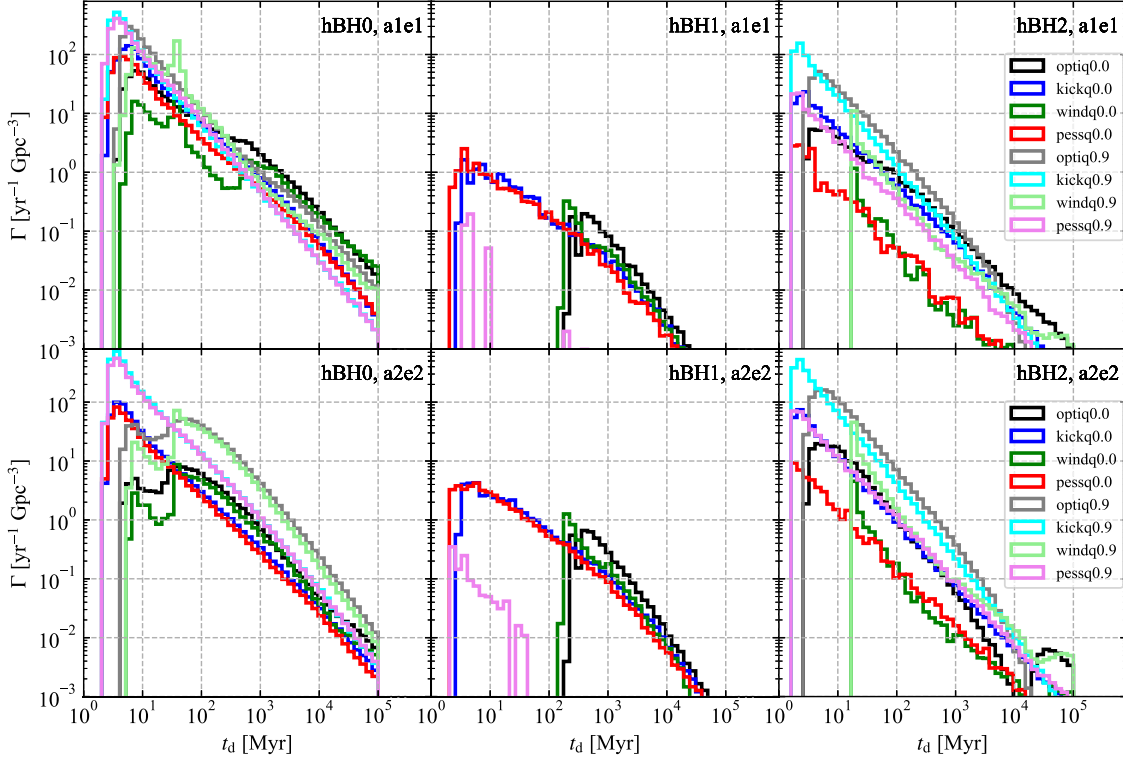


Figure 9. Merger rate densities of hBH0, hBH1, and hBH2 as a function of the delay time in the 16 main models. The left, middle, and right panels indicate the distributions of hBH0s, hBH1s, and hBH2s, respectively. The top and bottom panels indicate models with $a_{\min} = 10$ and $200R_{\odot}$, respectively. The colors of the curves show single star models and q_{\min} .

and hBH2s. In both panels, there is no BH–BH in the top-left and bottom-right corners. The reason for their absence from the top-left corner is that binaries merge before they form BH–BHs, and the reason for their absence from the bottom-right corner is that BH–BHs have too wide separation to merge within 15 Gyr.

Even binaries with $r_{p,i} \sim 10^3 R_{\odot}$ can form hBH0s, hBH1s, and hBH2s. This is because Population III stars with $M \gtrsim 50M_{\odot}$ expand to $\gtrsim 10^3 R_{\odot}$ (see Figure 1) and interact with their companions. Thus, the merger rates of hBH0s, hBH1s, and hBH2s in models with $a_{\min} = 200R_{\odot}$ are comparable to those in models with $a_{\min} = 10R_{\odot}$ as seen in Figure 9.

There is no hBH1 in the bottom panel. Binaries with high q_i cannot form an hBH1, because their members have similar masses. This is consistent with the merger rate density as a function of t_d in the middle panels of Figure 9. The merger rate of hBH1s is nearly zero in models with $q_{\min} = 0.9$. Nevertheless, the sums of the merger rates of hBH1s and hBH2s are independent of q_{\min} , because the increase of the hBH2 merger rate compensates for the decrease of the hBH1 merger rate in the case of $q_{\min} = 0.9$.

We have to keep in mind that, although the merger rates of hBH0s and the sum of hBH1s and hBH2s are insensitive to a_{\min} and q_{\min} , their formation channels can depend on a_{\min} and q_{\min} . Figure 11 is the same plot as Figure 10, except for color coding that indicates common-envelope channels forming BH–BHs. We can see that hBH0s are formed from binaries with $r_{p,i} \lesssim 50R_{\odot}$ and $\gtrsim 50R_{\odot}$ through stable mass transfer (the CE0 channel), and common-envelope evolution (the CE1, CE2, and CE4 channels), respectively. The boundary of $r_{p,i}$ increases with $m_{1,i}$, because BSG stars can have larger radii with $m_{1,i}$. The reason for the absence of the CE3 channel is described in

Section 3.2. Thus, only the CE1, CE2, and CE4 channels work for forming hBH0s in the cases of $a_{\min} = 200R_{\odot}$.

All the hBH1s are formed from binaries with $r_{p,i} \gtrsim 10^2 R_{\odot}$ through the CE1 channel. We draw an example binary evolution leading to one hBH1 in Figure 12. To form hBH1s, binaries should have a small q_i . Due to the small q_i , a binary experiences a merger or common-envelope evolution when the first-evolving star fills its Roche lobe. If the first-evolving star is in its MS and CHeB/ShHeB phases, the binary experiences merger and common-envelope evolution, respectively. The common-envelope evolution reduces the binary separation down to several $10R_{\odot}$. Then, the second-evolving star expands to $\sim 10R_{\odot}$, fills its Roche lobe, and drives stable mass transfer, because it is a BSG star, and its mass ratio to the first BH is small. Eventually, binaries forming hBH1s experience common-envelope evolution driven by the first-evolving star, i.e., the CE1 channel.

A fraction of hBH2s are formed from binaries with $r_{p,i} \lesssim 10^2 R_{\odot}$ through the CE0 channel, and the rest of them from binaries with $r_{p,i} \gtrsim 10^2 R_{\odot}$ through the CE4 channel. For binaries with $r_{p,i} \lesssim 10^2 R_{\odot}$, both the first- and second-evolving stars fill their Roche lobes when they are BSG stars. Then, they drive stable mass transfer, i.e., the CE0 channel. For binaries with $r_{p,i} \gtrsim 10^2 R_{\odot}$, they enter into their CHeB/ShHeB phases almost at the same time due to their similar masses and fill their Roche lobes. Then, the binaries experience the CE4 channel. We draw an example binary evolution leading to one hBH2 through the CE4 channel in Figure 13, which can occur regardless of q_{\min} and q_{\max} as seen in Figure 10.

The merger rates of hBH0s, hBH1s, and hBH2s are insensitive to single star models for the following reasons. Natal kicks have small effects on the binary parameters of BH–

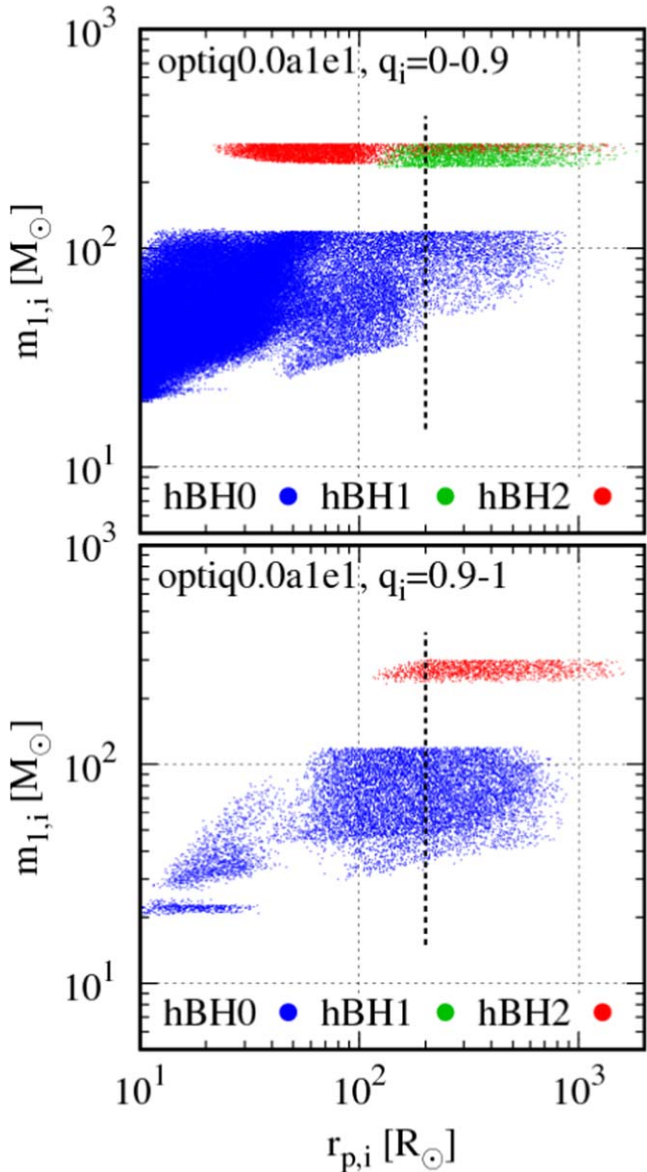


Figure 10. Initial pericenter distances ($r_{p,i}$) and the first-evolving star’s mass ($m_{1,i}$) of BH–BHs with $t_d = 0$ –15 Gyr in the optiq0.0a1e1 model. In the top and bottom panels, the initial mass ratios (q_i) are 0–0.9 and 0.9–1, respectively. The vertical dashed lines indicate $r_{p,i} = 200R_\odot$. The color codes show hBH0, hBH1, and hBH2.

BHs. This is because the natal kick velocities are comparable to or smaller than the internal velocities of BH–BHs with $t_d < 15$ Gyr. Stellar winds do not prevent stars from filling their Roche lobe and interacting with their companions. Because they are driven by stellar rotations, they are active only when stars nearly fill their Roche lobe. They can strip H envelopes from stars and decrease stellar masses (see Figure 3). Nevertheless, stars also lose their H envelopes through common-envelope evolution (see Figure 10) even if stellar winds are switched off. Thus, stellar winds do not have dominant roles in stripping H envelopes from stars.

In the following sections, we investigate in detail hBH0, hBH1, and hBH2 in Sections 3.3.1–3.3.3, respectively. In advance, Figure 14 summarizes their features, and Figure 15 shows their characteristic features that have weak dependences on initial conditions (q_{\min} and a_{\min}) and stellar evolution

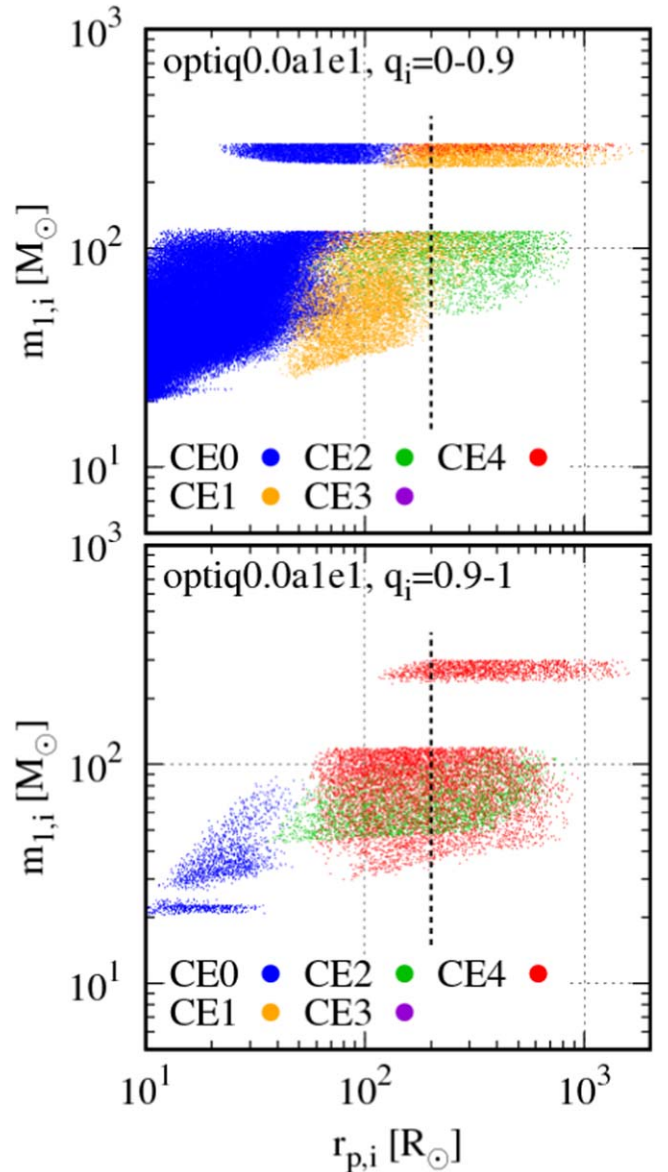


Figure 11. The same as in Figure 10, except for color codes that indicate common-envelope channels forming BH–BHs.

models (stellar winds and natal kicks). They will help in reading the following sections.

3.3.1. Binaries with Two Low-mass BHs (hBH0s)

We investigate first the optiq0.0a1e1 model and next the other main models. This is because hBH0s in the optiq0.0a1e1 model have all the features the other models have, and those in the other models have a subset of them, as will be revealed later.

Figure 16 shows the merger rate density of hBH0s for each t_d in the optiq0.0a1e1 model. We can find two peaks in the $m_{b,p}$ and $m_{b,s}$ distributions for $t_d = 0.1$ –15 Gyr. One peak is at $m_{b,p} \sim m_{b,s} \sim 45$ – $50M_\odot$. We call this peak “the higher-mass peak.” The higher-mass peak appears for all t_d (including $t_d = 0$ –0.1 Gyr). The other peak is at $m_{b,p} \sim m_{b,s} \sim 20$ – $35M_\odot$ and for $t_d = 0.1$ –15 Gyr, named “the lower-mass peak.” We do not consider that a population of $m_{b,p} = 15$ – $20M_\odot$ for $t_d = 0$ –0.1 Gyr is associated with the lower-mass peak, because it is too weak. The lower-mass

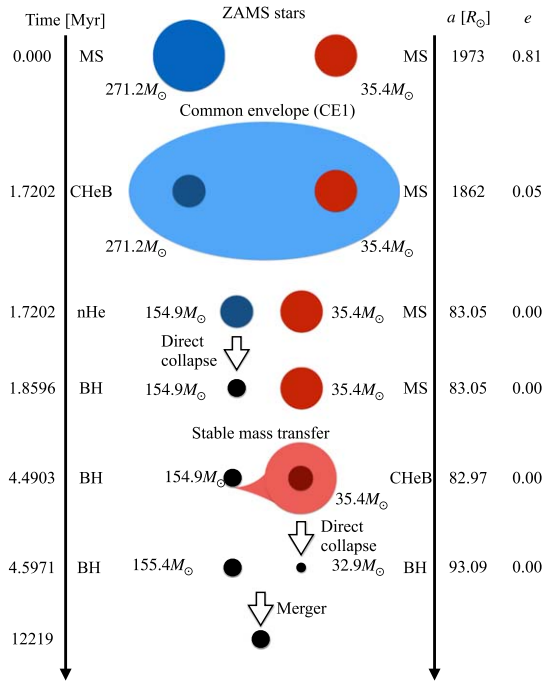


Figure 12. Example binary evolution leading to one hBH1 through the CE1 channel.

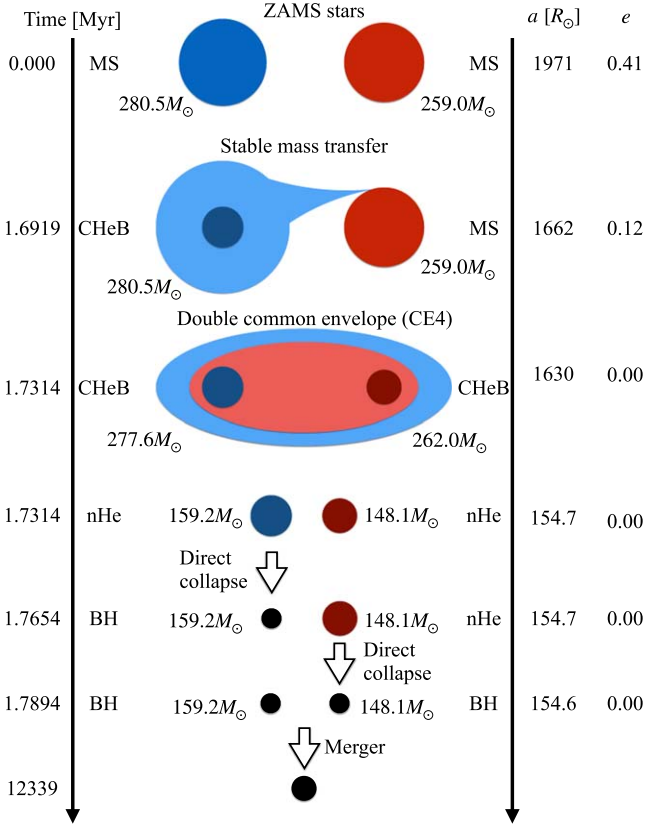


Figure 13. Example binary evolution leading to one hBH2 through the CE4 channel.

peak shifts from $(m_{b,p}, m_{b,s}) \sim (20M_\odot, 20M_\odot)$ to $(m_{b,p}, m_{b,s}) \sim (35M_\odot, 35M_\odot)$ with t_d . The merger rate density is decreased sharply at both ends of ~ 5 and $50 M_\odot$. There are no $3\text{--}5M_\odot$ BHs, the so-called “lower-mass gap,” because the rapid model never

forms BHs in the lower-mass gap. The number of BHs in the PI mass gap is quite small due to PPI/PISN effects. A few BHs in the PI mass gap can be formed from stars with light He cores and heavy H envelopes (see Figure 3), or through accretion from their companion stars. These BHs have at most $55M_\odot$, while BHs can have $\sim 85M_\odot$ if they evolve as single stars (see Figure 3). This is because BH progenitors in binaries easily lose their H envelopes through binary interactions.

The higher-mass peak appears due to PPI effects. This peak is not observed in the K14 model, which does not account for PPI effects. Stars with He core masses of $45\text{--}65M_\odot$ experience PPI and are thus swept up together to BHs with $45M_\odot$. Because PPI effects are independent of binary star evolution, the higher-mass peak always appears regardless of t_d .

The lower-mass peak has two features; it shifts from $\sim 20M_\odot$ to $\sim 35M_\odot$, and the mass ratio favors a value of nearly unity. The reasons for the two features can be explained by their formation channels. Here, we first explain the formation channel, and next the reasons for the features. The lower-mass peak is formed through the same mechanism as the peak of $\sim 30M_\odot$ in the K14 model, i.e., the CE0 channel. The details of the processes are as follows. The first-evolving star enters into its CHeB phase, fills its Roche lobe, and starts stable mass transfer to the second-evolving star. The mass transfer can remain stable, because a Population III star with $M_{ZAMS} = 10\text{--}50M_\odot$ ends its life as a BSG star (see Figure 1). Subsequently, the first-evolving star collapses to a BH. After that, the second-evolving star also fills its Roche lobe and begins stable mass transfer. Finally, the second-evolving star collapses into a BH.

The reason for the mass ratio of unity is as follows. The first mass transfer makes the second-evolving star heavier than the first BH. Because mass transfer is more efficient when the donor star is heavier than the accreting star, the second mass transfer continues until the mass ratio of the second-evolving star to the first BH becomes close to unity. After that, the second-evolving star collapses to a BH with a similar mass to the first BH. Thus, these BH–BHs tend to have a mass ratio of unity.

The reason for the time shift of the lower-mass peak is as follows. The merging timescale through GW radiation is expressed as

$$t_{\text{GW}} = \frac{5}{256} \frac{c^5}{G^3} \frac{a^4}{m_{b,p} m_{b,s} (m_{b,p} + m_{b,s})} g(e) \quad (25)$$

$$g(e) = \frac{(1 - e^2)^{3.5}}{1 + (73/24)e^2 + (37/96)e^4}, \quad (26)$$

where a and e are the semimajor axis and eccentricity of a BH–BH. Because $m_{b,p} \sim m_{b,s}$ and $e \sim 0$ here, we reduce these equations to $t_{\text{GW}} \propto a^4 m^{-3}$, where we use m instead of $m_{b,p}$ and $m_{b,s}$. The semimajor axis is proportional to the radius of the second-evolving star, $a \propto R_2$, when the second mass transfer occurs. Because $R_2 \propto L_2^{1/2}$, and $L_2 \propto m^2$ for stars with $10\text{--}50M_\odot$ in CHeB and ShHeB phases (see Figure 1), $a \propto m$. Finally, $t_{\text{GW}} \propto m$. We now assume that the second-evolving star with a different m has the same effective temperature. If we relax this assumption, the second-evolving star with a larger m tends to have a lower effective temperature for $m \gtrsim 20M_\odot$ (see Figure 1). Then, t_{GW} can depend on m more strongly. Thus, the time shift of the lower-mass peak appears.

optiq0.0a1e1
 $(q_{\min} = 0.0, a_{\min} = 10R_{\odot}, \text{No kicks, No winds})$

hBH0:
 $m_{b,p}, m_{b,s} < 50M_{\odot}$
 Mergers peak at
 • $m_{b,p}, m_{b,s} \sim 20 \rightarrow 35M_{\odot}$
 at $t_d \sim 0.1 \rightarrow 15\text{Gyr}$
 • 100 % high spins at $t_d \sim 15\text{Gyr}$
 • $m_{b,p}, m_{b,s} \sim 45M_{\odot}$
 • spin decreases with t_d
 • 50 % high spins at $t_d \sim 15\text{Gyr}$

hBH1: $m_{b,p} > 130M_{\odot}$, $m_{b,s} < 50M_{\odot}$
 Mergers only at $t_d > 0.1\text{Gyr}$
 Mergers peak at
 • $m_{b,p} \sim 130 - 180M_{\odot}$
 • tail at $\sim 180 - 200M_{\odot}$
 • spin decreases with t_d
 • no high spins at $t_d \sim 15\text{Gyr}$
 • $m_{b,s} \sim 25 \rightarrow 40M_{\odot}$ at $t_d \sim 0.1 \rightarrow 15\text{Gyr}$
 • 100 % high spins at $t_d \sim 15\text{Gyr}$

hBH2: $m_{b,p}, m_{b,s} > 130M_{\odot}$
hBH2/hBH1 ~ 3
 Mergers peak at
 • $m_{b,p} \sim 130 - 180M_{\odot}$ at $t_d < 0.1\text{Gyr}$,
 $m_{b,p} \sim 130 - 200M_{\odot}$ at $t_d > 0.1\text{Gyr}$
 • spin decreases with t_d
 • no high spins at $t_d \sim 15\text{Gyr}$
 • $m_{b,s} \sim 130 - 170M_{\odot}$
 • spin decreases with t_d
 • no high spins at $t_d \sim 15\text{Gyr}$

 $q_{\min} = 0.0 \rightarrow 0.9$

hBH0:
 $m_{b,p}, m_{b,s} < 50M_{\odot}$
 Mergers peak at
 • $m_{b,p}, m_{b,s} \sim 30M_{\odot}$ at $t_d \sim 10 - 15\text{Gyr}$
 • 100 % high spins at $t_d \sim 15\text{Gyr}$
 • $m_{b,p}, m_{b,s} \sim 45M_{\odot}$
 • spin decreases with t_d
 • no high spins at $t_d \sim 15\text{Gyr}$

hBH1: $m_{b,p} > 130M_{\odot}$, $m_{b,s} < 50M_{\odot}$
 Mergers only at $t_d > 0.1\text{Gyr}$
 Mergers peak at
 • $m_{b,p} \sim 130 - 180M_{\odot}$
 • tail at $\sim 180 - 200M_{\odot}$
 • spin decreases with t_d
 • no high spins at $t_d \sim 15\text{Gyr}$
 • $m_{b,s} \sim 25 \rightarrow 40M_{\odot}$ at $t_d \sim 0.1 \rightarrow 15\text{Gyr}$
 • 100 % high spins at $t_d \sim 15\text{Gyr}$

hBH2: $m_{b,p}, m_{b,s} > 130M_{\odot}$
hBH2/hBH1 $\gg 1$
 Mergers peak at
 • $m_{b,p} \sim 130 - 180M_{\odot}$ at $t_d < 0.1\text{Gyr}$,
 $m_{b,p} \sim 130 - 180M_{\odot}$ at $t_d > 0.1\text{Gyr}$
 • 100 % high spins at $t_d \sim 15\text{Gyr}$
 • $m_{b,p}, m_{b,s} \sim 45M_{\odot}$
 • spin decreases with t_d
 • no high spins at $t_d \sim 15\text{Gyr}$
 • $m_{b,s} \sim 130 - 170M_{\odot}$
 • spin decreases with t_d
 • no high spins at $t_d \sim 15\text{Gyr}$

 $a_{\min} = 10 \rightarrow 200R_{\odot}$

hBH0:
 $m_{b,p}, m_{b,s} < 50M_{\odot}$
 Mergers peak at
 • $m_{b,p}, m_{b,s} \sim 20 \rightarrow 35M_{\odot}$ at $t_d \sim 0.1 \rightarrow 15\text{Gyr}$
 • 100 % high spins at $t_d \sim 15\text{Gyr}$

hBH1: $m_{b,p} > 130M_{\odot}$, $m_{b,s} < 50M_{\odot}$
hBH2/hBH1 ~ 0.1
 Mergers only at $t_d > 0.1\text{Gyr}$
 Mergers peak at
 • $m_{b,p} \sim 130 - 180M_{\odot}$ at $t_d < 0.1\text{Gyr}$,
 $m_{b,p} \sim 130 - 180M_{\odot}$ at $t_d > 0.1\text{Gyr}$
 • 100 % high spins at $t_d \sim 15\text{Gyr}$
 • $m_{b,s} \sim 25 \rightarrow 40M_{\odot}$ at $t_d \sim 0.1 \rightarrow 15\text{Gyr}$
 • 100 % high spins at $t_d \sim 15\text{Gyr}$

hBH2: $m_{b,p}, m_{b,s} > 130M_{\odot}$
hBH2/hBH1 ~ 0.1
 Mergers peak at
 • $m_{b,p} \sim 130 - 180M_{\odot}$ at $t_d < 0.1\text{Gyr}$,
 $m_{b,p} \sim 130 - 180M_{\odot}$ at $t_d > 0.1\text{Gyr}$
 • spin decreases with t_d
 • no high spins at $t_d \sim 15\text{Gyr}$
 • $m_{b,s} \sim 130 - 170M_{\odot}$
 • spin decreases with t_d
 • no high spins at $t_d \sim 15\text{Gyr}$

No kicks \rightarrow Kicks

hBH0:
 $m_{b,p}, m_{b,s} < 50M_{\odot}$
 Mergers peak at
 • $m_{b,p}, m_{b,s} \sim 30M_{\odot}$ at $t_d \sim 0 - 15\text{Gyr}$
 • 100 % high spins at $t_d \sim 15\text{Gyr}$
 • $m_{b,p}, m_{b,s} \sim 45M_{\odot}$
 • spin decreases with t_d
 • 50 % high spins at $t_d \sim 15\text{Gyr}$
 • $m_{b,s} \sim 30M_{\odot}$ at $t_d \sim 0.1 \rightarrow 15\text{Gyr}$
 • 100 % high spins at $t_d \sim 15\text{Gyr}$

hBH1: $m_{b,p} > 130M_{\odot}$, $m_{b,s} < 50M_{\odot}$
 Mergers only at $t_d > 0.1\text{Gyr}$
 Mergers peak at
 • $m_{b,p} \sim 130 - 180M_{\odot}$
 • tail at $\sim 180 - 200M_{\odot}$
 • spin decreases with t_d
 • 50 % high spins at $t_d \sim 15\text{Gyr}$
 • $m_{b,s} \sim 30M_{\odot}$ at $t_d \sim 0.1 \rightarrow 15\text{Gyr}$
 • 100 % high spins at $t_d \sim 15\text{Gyr}$

hBH2: $m_{b,p}, m_{b,s} > 130M_{\odot}$
hBH2/hBH1 ~ 1
 Mergers peak at
 • $m_{b,p} \sim 130 - 200M_{\odot}$ at $t_d < 0.1\text{Gyr}$,
 $m_{b,p} \sim 130 - 200M_{\odot}$ at $t_d > 0.1\text{Gyr}$
 • 20 % high spins at $t_d \sim 15\text{Gyr}$
 • $m_{b,p}, m_{b,s} \sim 45M_{\odot}$
 • spin decreases with t_d
 • 50 % high spins at $t_d \sim 15\text{Gyr}$
 • $m_{b,s} \sim 130 - 170M_{\odot}$
 • spin decreases with t_d
 • 50 % high spins at $t_d \sim 15\text{Gyr}$

No winds \rightarrow Winds

hBH0:
 $m_{b,p}, m_{b,s} < 50M_{\odot}$
 Mergers peak at
 • $m_{b,p}, m_{b,s} \sim 20M_{\odot}$ at $t_d \sim 0 - 15\text{Gyr}$
 • 20 % high spins at $t_d \sim 15\text{Gyr}$

hBH1: $m_{b,p} > 130M_{\odot}$, $m_{b,s} < 50M_{\odot}$
hBH2/hBH1 ~ 0.3
 Mergers only at $t_d > 0.1\text{Gyr}$
 Mergers peak at
 • $m_{b,p} \sim 130 - 180M_{\odot}$ at $t_d < 0.1\text{Gyr}$,
 $m_{b,p} \sim 130 - 180M_{\odot}$ at $t_d > 0.1\text{Gyr}$
 • spin decreases with t_d
 • no high spins at $t_d \sim 15\text{Gyr}$
 • $m_{b,s} \sim 20M_{\odot}$ at $t_d \sim 0.1 \rightarrow 15\text{Gyr}$
 • 30 % high spins at $t_d \sim 15\text{Gyr}$

hBH2: $m_{b,p}, m_{b,s} > 130M_{\odot}$
hBH2/hBH1 ~ 0.3
 Mergers peak at
 • $m_{b,p} \sim 130 - 180M_{\odot}$ at $t_d < 0.1\text{Gyr}$,
 $m_{b,p} \sim 130 - 180M_{\odot}$ at $t_d > 0.1\text{Gyr}$
 • spin decreases with t_d
 • no high spins at $t_d \sim 15\text{Gyr}$
 • $m_{b,s} \sim 130 - 170M_{\odot}$
 • spin decreases with t_d
 • no high spins at $t_d \sim 15\text{Gyr}$

Figure 14. Features of hBH0s, hBH1s, and hBH2s for the optiq0.0a1e1 model, and their variations with initial conditions and stellar evolution models. We regard the spin magnitude of ~ 0.3 as the boundary between high and low spins. The ratio of hBH2s to hBH1s is indicated by hBH2/hBH1. We cross out disappearing features and emphasize changed values with bold font and an underline. For hBH2s, $m_{b,p} \lesssim 200$ and $\gtrsim 180M_{\odot}$ indicate the parallelogram and triangle shapes in 2D mass distribution, respectively. Note that these features consider only cases where only one of the initial conditions and stellar models is changed.

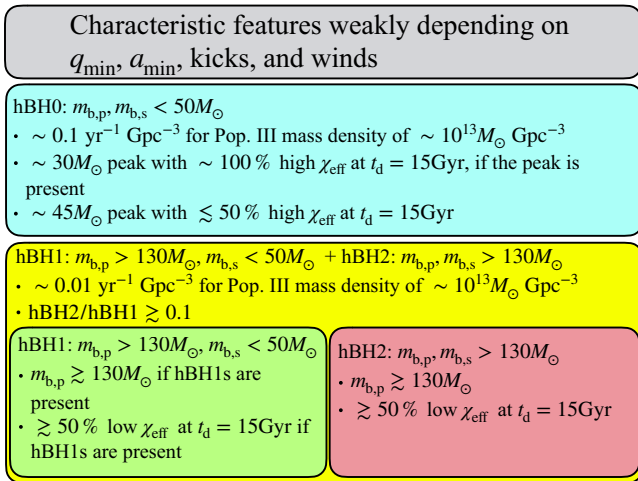


Figure 15. Characteristic features weakly depending on initial conditions (q_{\min} and a_{\min}) and stellar evolution models (stellar winds and natal kicks).

Figure 17 shows the spin distributions of the primary and secondary BHs of hBH0s in the optiq0.0a1e1 model. We can consider that hBH0s with $0 \leq m_{b,p}/M_\odot < 40$ and $40 \leq m_{b,p}/M_\odot < 100$ are associated with populations of lower-mass and higher-mass peaks, respectively. The top two panels indicate that hBH0s in the lower-mass peak have two BHs with high spins ~ 1 independently of t_d . The reason is as follows. Their progenitors can be highly spun up by the tidal fields of their companion stars, because they expand to their Roche-lobe radii. Moreover, they keep their H envelopes more or less until they collapse into BHs.

On the other hand, half of hBH0s in the higher-mass peak have BHs with nearly zero spins. This is due to PPI effects. We assume BH progenitors undergoing PPI lose their spin angular momenta. The other half have high spins with $\gtrsim 0.5$, but have smaller spins with t_d increasing. The reason for the time dependence is as follows. BH progenitors gain and lose their spin angular momenta through tidal interactions and mass transfer, respectively. As the t_d increases, the binary separation becomes larger, and tidal interaction becomes weaker. Thus, a BH progenitor decreases its spin angular momentum in the net, and its BH has a lower spin. The details can be described in many studies (Kushnir et al. 2016; Hotokezaka & Piran 2017; Piran & Piran 2020; Safarzadeh & Hotokezaka 2020). We call this relation the spin– t_d relation tentatively.

With respect to spins, the hBH0s have four subpopulations; both BHs have high spins (~ 1), both BHs have low spins (~ 0), and the first (second) BH has a high spin (~ 1) but the other BH has a low spin (~ 0). This is different from the results of Kinugawa et al. (2016b, 2016c). In their model, the hBH0s do not have a subpopulation with the first BHs with high spins and the second BHs with low spins. We obtain the subpopulation, because we assume BHs after PPI have zero spins.

Hereafter, we assess the dependence of these features on the initial conditions of binaries (q_{\min} and a_{\min}) and single star models (stellar winds and natal kicks). First, we focus on the dependence on initial conditions.

Figure 18 shows the merger rate densities of hBH0s in models with different initial conditions from the optiq0.0a1e1 model. We can find peaks at $(m_{b,p}, m_{b,s}) \sim (45M_\odot, 45M_\odot)$ in all the panels. These peaks correspond to the higher-mass peak in the optiq0.0a1e1 model. Even in the optiq0.0a2e2 and

optiq0.9a2e2 models, there can be hBH0s with $t_d \leq 15$ Gyr. This is because stars with $M_{\text{ZAMS}} \sim 100M_\odot$ can expand to $\gtrsim 10^3 R_\odot$ (see Figure 1), interact with their companion stars through common-envelope evolutions, and leave $45M_\odot$ BHs (see Figure 3). Consequently, the higher-mass peak in the optiq0.0a1e1 model is present regardless of different initial conditions (q_{\min} and a_{\min}).

We cannot find the lower-mass peak in the optiq0.0a2e2 and optiq0.9a2e2 model. In these models, hBH0s with $t_d \leq 15$ Gyr cannot form through the CE0 channel. Because the CE0 channel does not reduce binary separations, hBH0s formed through the CE0 channel have binary separations $\gtrsim 100R_\odot$. Their merging timescales through GW radiation are much larger than 15 Gyr. We can find the lower-mass peak in the optiq0.9a1e1 model for $t_d = 10\text{--}15$ Gyr, which is formed through the same mechanism in the optiq0.0a1e1 model. On the other hand, we cannot find the lower-mass peak in this model for $t_d = 0.1\text{--}1$ Gyr. Because two stars with similar masses expand on similar timescales, they fill their Roche lobes and merge when their separation is small. Eventually, the lower-mass peak in the optiq0.0a1e1 model is sensitive to a_{\min} , and its time shift is weak against q_{\min} .

Although the presence of the higher-mass peak is insensitive to initial conditions, the spin distributions of hBH0s around the higher-mass peak can be affected by initial conditions. Half of the primary and secondary BHs have nearly zero spins in the optiq0.0a1e1 model, while more than half of them have nearly zero spins in the other models, and moreover, the fraction increases with time up to unity for $t_d = 10\text{--}15$ Gyr. This is because the CE0 channel has little contribution to the higher-mass peak in the other models. On the other hand, the spin distributions of hBH0s around the lower-mass peak are similar between the optiq0.0a1e1 and optiq0.9a1e1 models if the lower-mass peak is present in the optiq0.9a1e1 model.

Next, we focus on the dependence on single star models. Figure 19 shows the merger rate densities of hBH0s in models with different single star models. We can find peaks at $(m_{b,p}, m_{b,s}) \sim (45M_\odot, 45M_\odot)$ in all the panels. These peaks correspond to the higher-mass peak in the optiq0.0a1e1 model. Therefore, the higher-mass peak is present with or without stellar winds and natal kicks.

The kickq0.0a1e1 model has a lower-mass peak of $(m_{b,p}, m_{b,s}) \sim (30M_\odot, 30M_\odot)$ independently of t_d (see the top panels). In other words, the lower-mass peak has no time shift, unlike in the optiq0.0a1e1 model. This is because natal kicks shorten and lengthen the merging timescales of hBH0s, independently of their masses. For example, if a BH progenitor gets a natal kick whose direction is the same as and opposite to its traveling direction, the resulting merging timescale becomes longer and shorter, respectively. Whether the time shift can survive or not depends on the magnitude of natal kicks. We can observe the time shift in the half-kick model, although it is less distinct than in the optiq0.0a1e1 model. If we assume $\sigma_k = 265 \text{ km s}^{-1}$ for NSs and kick velocities inversely proportional to remnant masses as in the commonly used prescription, the time shift can be seen as prominent as in the optiq0.0a1e1 model, because the kick velocities are $\sim 10 \text{ km s}^{-1}$ for BHs with several $10M_\odot$.

Stellar winds significantly smooth the lower-mass peak and shift it to $\sim 20M_\odot$ (see the bottom panels). The peak shift is simply because BHs lose their masses through stellar winds. This is not due to stellar winds of high metallicity, $10^{-3} Z_\odot$. In the weak-wind model ($Z = 10^{-5} Z_\odot$), hBH0s have merger rate

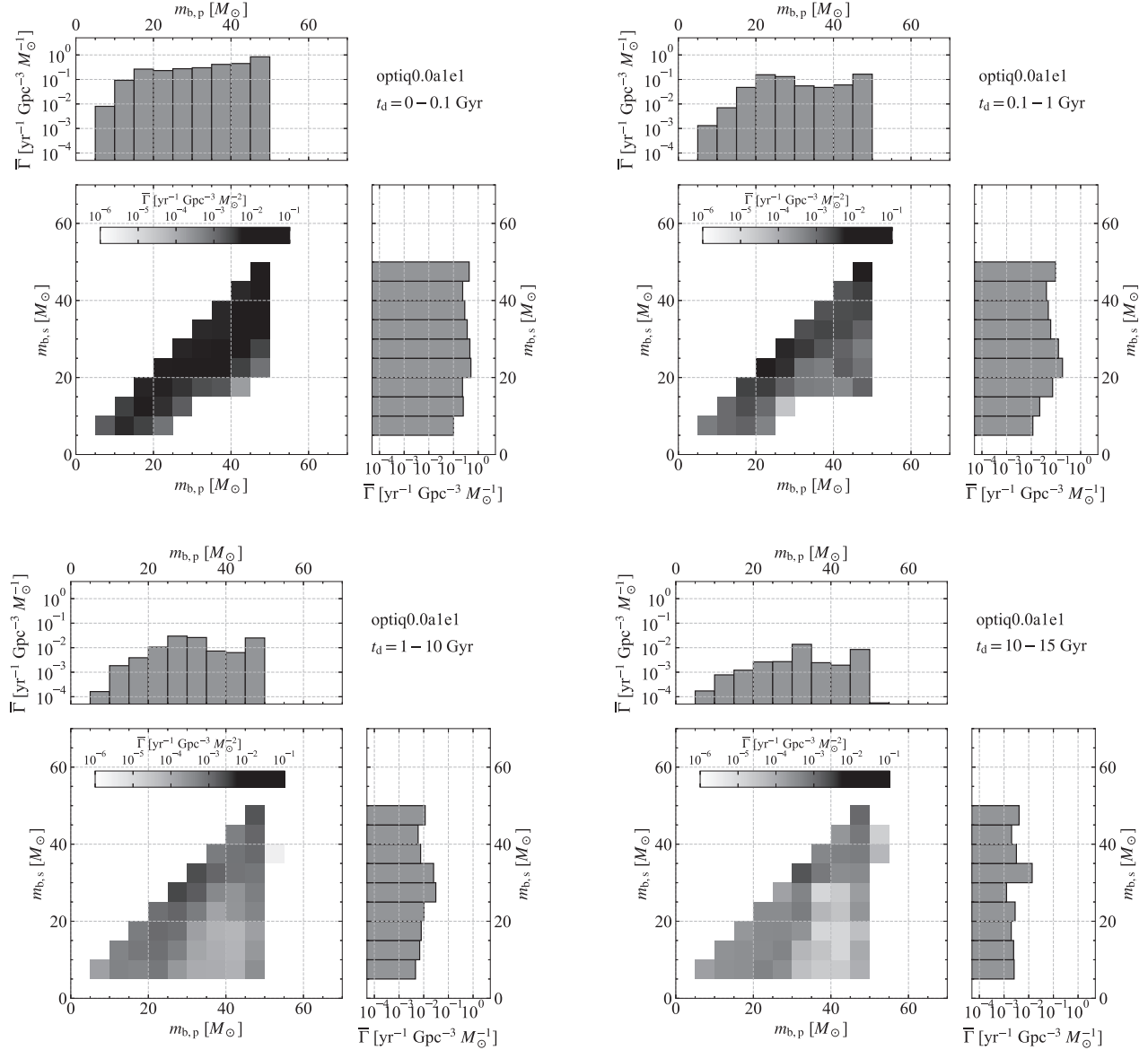


Figure 16. Merger rate densities of hBH0s for $t_d = 0-0.1$ (top left), $0.1-1$ (top right), $1-10$ (bottom left), and $10-15$ Gyr (bottom right) in the optiq0.0a1e1 model.

densities similar to those in the windq0.0a1e1 model. In fact, rotationally enhanced winds are responsible. If we switch off the rotationally enhanced winds in the no-rot-wind model, we find the merger rate densities similar to those in the optiq0.0a1e1 model. It is natural that the rotationally enhanced winds have strong effects in models with $a_{\min} = 10R_\odot$, because most of stars are effectively spun up by tidal fields of their companion stars. Eventually, the lower-mass peak is fragile against stellar winds with rotational enhancement. Although the lower-mass peak is present despite of the presence of natal kicks, its shift with t_d is erased by the natal kicks.

The distribution of spin magnitudes in the kickq0.0a1e1 model is similar to in the optiq0.0a1e1 model for both $0 \leq m_{b,p}/M_\odot < 40$ and $40 \leq m_{b,s}/M_\odot < 100$. On the other hand, the fraction of hBH0s with nearly zero spins in the windq0.0a1e1 and pessq0.0a1e1 models is 2 times larger than in the optiq0.0a1e1 model for $40 \leq m_{b,s}/M_\odot < 100$ (compare Figure 20 with Figure 17). This is because stellar winds carry away spin angular momenta. We do not show spin distributions

of hBH0s for $0 \leq m_{b,p}/M_\odot < 40$ in these models, because the lower-mass peak is weak.

Natal kicks can tilt the BH spin vectors from the binary orbit vectors of hBH0s. Figure 21 shows the tilt-angle distribution. Note that the spin and binary orbit vectors are parallel and antiparallel for $\cos \theta = 1$ and -1 , respectively. The fractions of $\theta \gtrsim 45^\circ$ and $\gtrsim 90^\circ$ are ~ 0.1 and ~ 0.01 , respectively, for both cases of $m_{b,p}$. Primary BHs have larger tilt angles than secondary BHs. Because primary BHs tend to have first-evolving stars as their progenitors, they have two chances to tilt their spin vectors from binary orbit vectors.

We examine the mass distribution of hBH0s in the “kick,” “wind,” and “pess” models with $q_{\min} \neq 0.0$ or $a_{\min} \neq 10R_\odot$. Then, in all of the models, we find peaks corresponding to the higher-mass peak in the optiq0.0a1e1 model. On the other hand, there is no lower-mass peak seen in the optiq0.0a1e1 model. Most BHs have zero spins for $t_d = 10-15$ Gyr. This is because they have a large t_d , and because most of them are not formed through the CE0 channel. If some of them were formed through the CE0 channel, there would be a lower-mass peak.

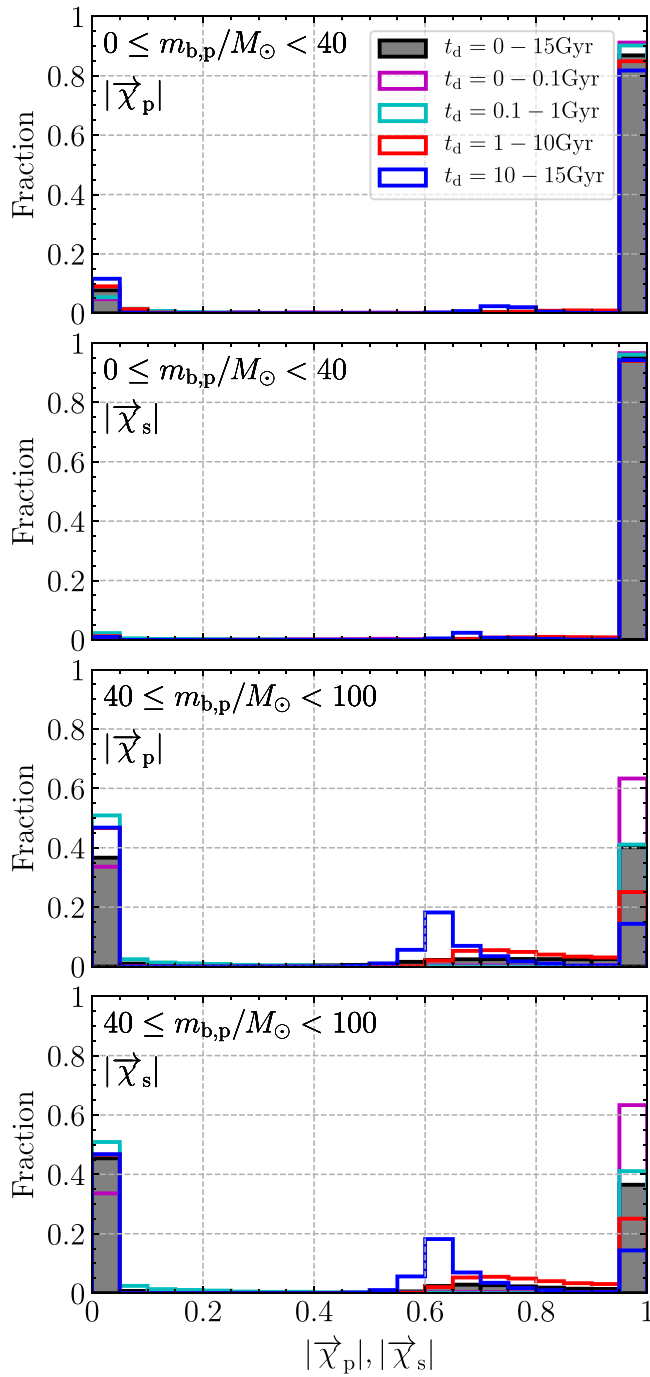


Figure 17. Spin distributions of hBH0s for each t_d in the optiq0.0a1e1 model. The panels indicate the primary and secondary BH spins of hBH0 with $0 \leq m_{b,p}/M_\odot < 40$ (the top two panels) and $40 \leq m_{b,p}/M_\odot < 100$ (the bottom two panels).

We summarize the features of merging hBH0s with $t_d \leq 15$ Gyr. In the optiq0.0a1e1 model, they have two peaks in their mass distribution: $(m_{b,p}, m_{b,s}) \sim (45M_\odot, 45M_\odot)$ (the higher-mass peak) and $(m_{b,p}, m_{b,s}) \sim (30M_\odot, 30M_\odot)$ (the lower-mass peak). The lower-mass peak shifts from $20M_\odot$ to $35M_\odot$ from $t_d = 0.1 - 1$ Gyr to $t_d = 10 - 15$ Gyr. Half (most) of the BHs belonging to the higher-mass (lower-mass) peak have a significantly high spin. The higher-mass peak is present even in models with different initial conditions (q_{\min} and a_{\min}) and different stellar evolution models (stellar winds and natal kicks), while BHs around the higher-mass peak tend to have

zero spins in models other than the optiq0.0a1e1 and kickq0.0a1e1 models due to small contribution of the CE0 channel. The lower-mass peak and its t_d dependence are quite fragile. It disappears when $a_{\min} = 200R_\odot$ or is shifted to $\sim 20M_\odot$ by stellar wind effects. Stellar winds have large effects on the lower-mass peak due to the rotational enhancement, not due to the high metallicity. The time-shift feature of the lower-mass peak is erased by natal kicks.

3.3.2. Binaries with High- and Low-mass BHs (hBH1s)

First, we investigate the optiq0.0a1e1 model again for the same reason in Section 3.3.1. Figure 22 shows the merger rate densities of hBH1s for each t_d . There is no hBH1 with $t_d \lesssim 0.1$ Gyr. Only binaries with $r_{p,i} \gtrsim 10^2 R_\odot$ can form hBH1s through the CE1 channel, and their minimum t_d is ~ 0.1 Gyr. On the other hand, a binary with $r_{p,i} \lesssim 10^2 R_\odot$ experiences a merger when the first-evolving star fills its Roche lobe for the reason described in Section 3.3.

For $t_d = 0.1 - 15$ Gyr, the $m_{b,p}$ distribution has a plateau in $m_{b,p} \sim 130 - 180M_\odot$ and has a tail in $m_{b,p} \sim 180 - 200M_\odot$. The plateau ranges from the minimum He core mass needed for the direct collapse ($M_{c,He,DC} = 135M_\odot$) to the He core mass of a star with $M_{ZAMS} = 300M_\odot$, the maximum mass of $m_{1,i}$ in our models. The merger rate density of $\sim 130M_\odot$ should be larger than that of $\sim 180M_\odot$, because the $m_{1,i}$ distribution is top light ($\propto m_{1,i}^{-1}$). Nevertheless, the number of stars forming $M_{c,He} \sim 180M_\odot$ ($m_{1,i} \sim 300M_\odot$) is comparable to that of stars forming $M_{c,He} \sim 135M_\odot$ ($m_{1,i} \sim 250M_\odot$). This is because the number ratio of the former star to the latter star is only ~ 1.2 . The tail is formed through stable mass transfer from the second-evolving stars to the first BH (see Figure 12). The tail is more prominent in smaller t_d , because the second-evolving stars are closer to the first BH and give a larger mass to the first BH.

The $m_{b,s}$ distribution has a peak at $25 - 40M_\odot$, and the peak shifts from $25M_\odot$ to $40M_\odot$ with t_d . This is the backreaction of the formation of the $m_{b,p}$ tail. As the second-evolving stars, progenitors of the second BHs, give larger mass to the first BH, they lose their mass.

We describe the three features of hBH1s: no merger for $t_d \lesssim 0.1$ Gyr, the $m_{b,p}$ distribution with the plateau and tail, and the $m_{b,s}$ distribution with the peak and its shift with t_d . Hereafter, we investigate the dependence of these features on the initial conditions (q_{\min} and a_{\min}) and single star models (stellar winds and natal kicks). Actually, these features are insensitive to a_{\min} . As seen in Figure 11, hBH1s can be formed through the CE1 channel even if binaries have $a_i \gtrsim 200R_\odot$. On the other hand, the formation of hBH1s is seriously affected by q_{\min} . For $q_{\min} = 0.9$, hBH1s are never formed (see Figures 9 and 10). Because a binary has stars with similar masses, it cannot form one IBH and one BH.

Natal kicks again erase the t_d dependence. In the kickq0.0a1e1 model, hBH1s with $t_d \lesssim 0.1$ Gyr appear, and the time shift of the peak in the $m_{b,s}$ distribution disappears. The $m_{b,s}$ peak is always at $\sim 30M_\odot$. Stellar winds also affect the mass distribution. The $m_{b,p}$ distribution also has a plateau for the following reason. The first-evolving stars always become nHe stars regardless of the presence or absence of stellar winds due to the CE1 channel. The nHe stars lose little mass through stellar winds, because they do not exceed the Eddington limit and are not sufficiently spun up. However, the tail disappears for the following reason. The second-evolving stars are

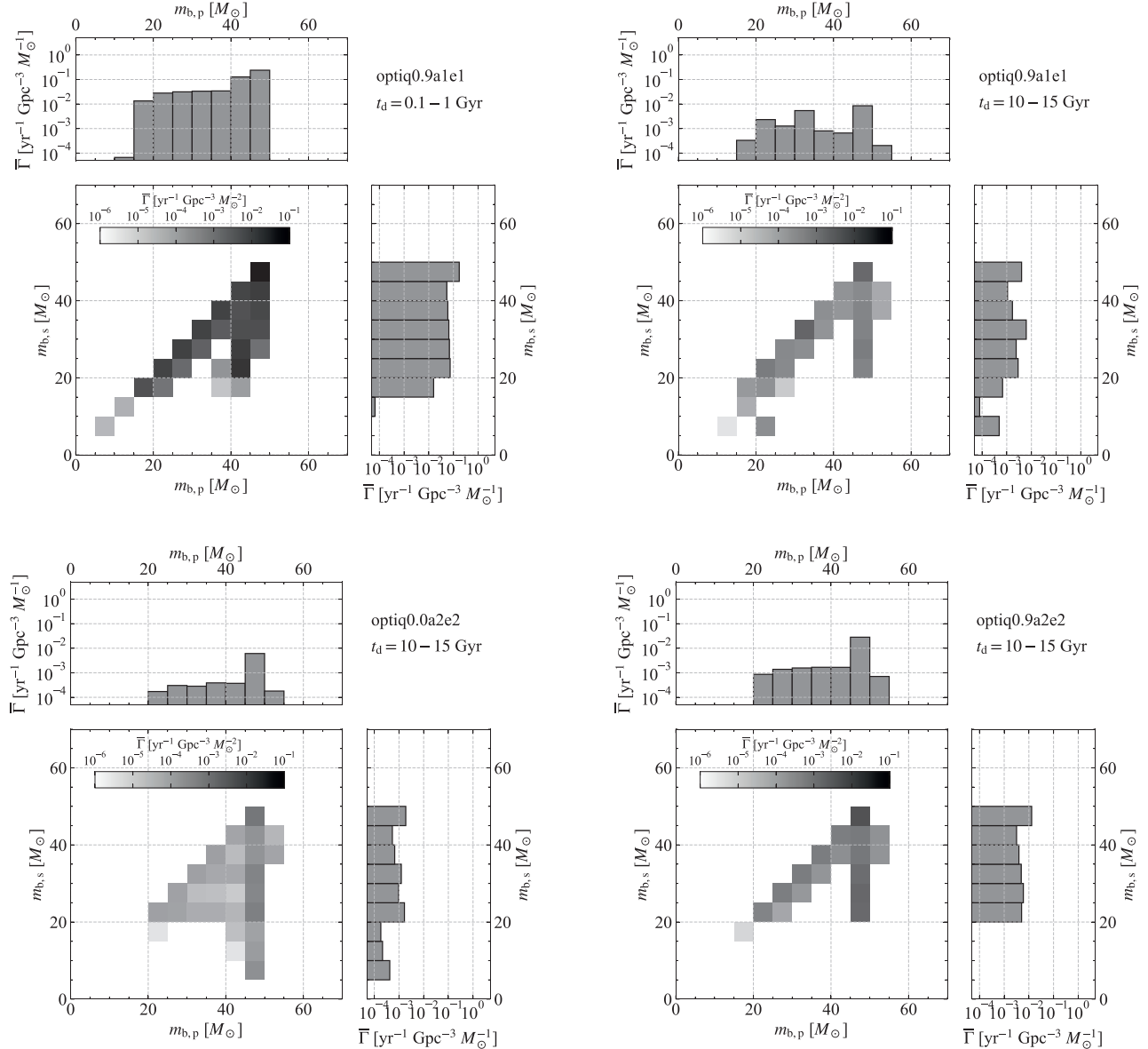


Figure 18. Merger rate densities of hBH0s. The top panels show the results of the optiq0.9a1e1 model for $t_d = 0.1 - 1$ (left) and $10 - 15$ Gyr (right). The bottom panels show the results of the optiq0.0a2e2 (left) and optiq0.9a2e2 models (right) for $t_d = 10 - 15$ Gyr.

strongly spun up by the first-evolving star or first BH after the CE1 channel. Then, they lose a significant portion of their H envelopes through stellar winds as seen in Figure 3. Thus, they cannot transfer their mass to the first BHs. The $m_{b,s}$ distribution is sensitive to the stellar winds, because the second-evolving stars are spun up and lose their mass rotationally enhanced stellar winds as described above. Then, the peak of $m_{b,s}$ moves down to $\sim 20M_\odot$. In the other models, we find that the mass distributions can be explained by simple combinations of initial conditions, natal kicks, and stellar winds.

Figure 23 shows the spin distributions of BHs in hBH1s. The fraction of primary BHs with nearly zero spins increases with t_d . The fraction of $|\vec{\chi}_p| \lesssim 0.2$ reaches ~ 1 for $t_d = 10 - 15$ Gyr. This can be also explained by the spin- t_d relation described in Section 3.3.1. On the other hand, the secondary BHs have high spins ~ 1 for all t_d . This is because they are spun up by the tidal fields of the first BHs and retain their H envelopes.

The spin distribution is insensitive to a_{\min} for the same reason as the mass distribution. Natal kicks erase the t_d dependence, and average the distribution to that for $t_d = 0 - 15$ Gyr. This is because natal kicks shorten and lengthen t_d at random as described in Section 3.3.1. Figure 24 shows the spin distributions of BHs in hBH1s in the windq0.0a1e1 model. Stellar winds largely reduce spins for both the primary and secondary BHs. Although the fraction of nonspinning BHs for $t_d = 10 - 15$ Gyr in the pessq0.0a1e1 model is smaller than in the windq0.0a1e1 model due to natal kicks, the fraction is still high (~ 0.6) for both the primary and secondary BHs.

Figure 25 shows the distribution of angles between the primary and secondary BH spin vectors and binary orbit vectors for hBH1s in the kickq0.0a1e1 model. The angles are formed only due to natal kicks. Comparing Figure 25 with Figure 21, we can find that spins of hBH1s are more aligned than those of hBH0s. This is not due to the small number of

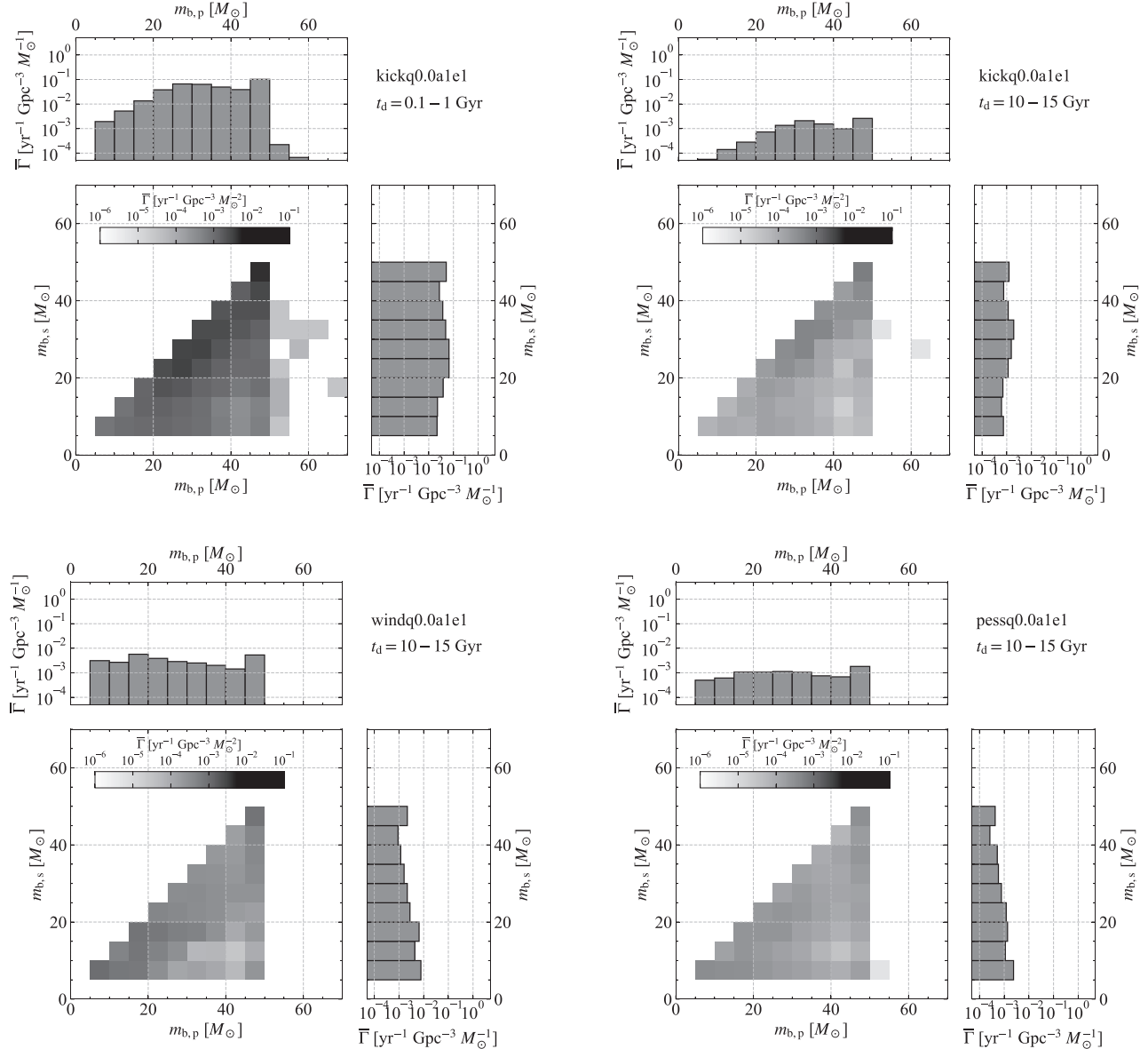


Figure 19. Merger rate densities of hBH0s. The top panels show the results of the kickq0.0a1e1 model for $t_d = 0.1 - 1$ (left) and $10 - 15$ Gyr (right). The bottom panels show the results of the windq0.0a1e1 (left) and pessq0.0a1e1 models (right) for $t_d = 10 - 15$ Gyr.

hBH1s, although the number of BHs in the top panel of Figure 25 is $\sim 10^3$ out of 10^6 binaries, and that in the top panel of Figure 21, it is $\sim 3 \times 10^4$ of 10^6 binaries. For example, the fraction of $\theta \gtrsim 45^\circ$ is a few 0.01 for hBH1s, while it is ~ 0.1 for hBH0s. This reason can be interpreted as follows. We can obtain the circular velocity of a BH-BH, rewriting Equation (25) as

$$v_{\text{circ}} \propto t_{\text{GW}}^{-1/8} m_{b,p}^{-1/8} m_{b,s}^{-1/8} (m_{b,p} + m_{b,s})^{3/8}. \quad (27)$$

As seen in Equation (27), the internal velocity of a BH-BH becomes larger with its total mass, if t_{GW} is fixed. Thus, BH-BHs with larger total masses are less sensitive to natal kicks. This is the reason why spins of hBH1s are more aligned than those of hBH0s.

We summarize the features of merging hBH1s. We first see the optiq0.0a1e1 model. They merge for $t_d \gtrsim 0.1$ Gyr. The $m_{b,p}$ distribution has a plateau in $130 - 180 M_\odot$ and a tail in $180 - 200 M_\odot$. The tail is more prominent in smaller t_d . The $m_{b,s}$ distribution has

a peak shifting from $20 M_\odot$ to $40 M_\odot$ with t_d . The fraction of hBH1s with $|\vec{\chi}_p| \lesssim 0.2$ increases with t_d and reaches unity for $t_d = 10 - 15$ Gyr, while the fraction of hBH1s with $|\vec{\chi}_s| \sim 1$ is unity for all t_d .

The above features are changed by various effects. First, hBH1s themselves vanish if $q_{\min} = 0.9$. The above features have a weak dependence on a_{\min} . Natal kicks erase the t_d dependence and raise spin-orbit misalignments smaller than those of hBH0s. Stellar winds erase the tail of the $m_{b,p}$ distribution and reduce the peak location of the $m_{b,s}$ distribution to $\sim 20 M_\odot$. Moreover, stellar winds greatly increase the fraction of hBH1s with $|\vec{\chi}_p| \sim 0$ and $|\vec{\chi}_s| \sim 0$.

3.3.3. Binaries with Two High-mass BHs (hBH2s)

We first investigate the optiq0.0a1e1 model, similarly to the previous sections. Figure 26 shows the merger rate density of hBH2s for each t_d . The 2D distribution for $t_d = 0 - 0.1$ Gyr has a triangular shape ($m_{b,p} \lesssim 180 M_\odot$), while that for $t_d = 0.1 - 15$ Gyr

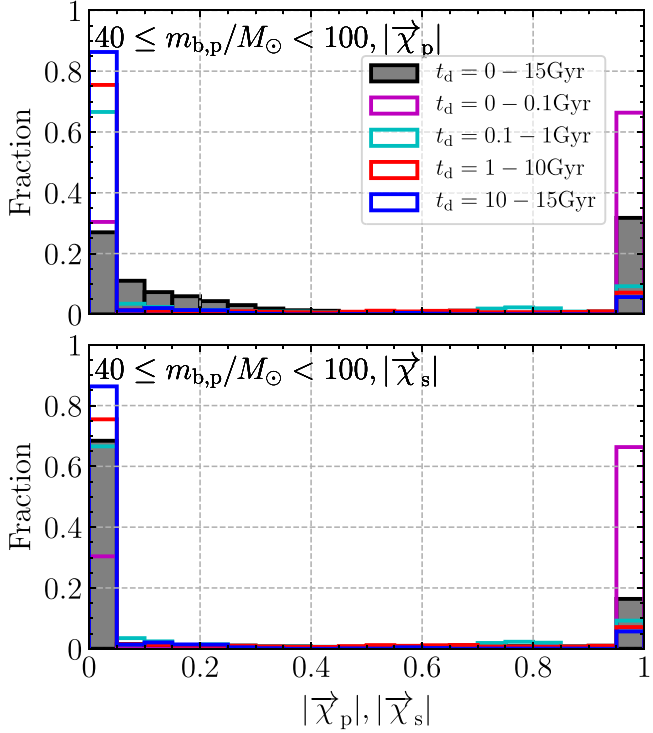


Figure 20. Spin distributions of hBH0s for each t_d in the windq0.0a1e1 model. The panels indicate the primary and secondary BH spins of hBH0s with $40 \leq m_{b,p}/M_\odot < 100$.

has a parallelogram shape ($m_{b,p} \lesssim 200M_\odot$). Their different shapes are due to the difference between their formation channels. For $t_d \lesssim 0.1$ Gyr, they are formed through the CE4 channel (see also Figure 11). This is the reason why the $m_{b,p}$ distribution is flat in $130\text{--}180M_\odot$, the same reason for the plateau of the primary BHs in hBH1s described in Section 3.3.2. The $m_{b,s}$ distribution monotonically decreases with $m_{b,s}$. In our initial conditions, as the second-evolving stars become more massive, they have fewer chances to have first-evolving stars with $M_{\text{ZAMS}} = 250\text{--}300M_\odot$ which overcome PISN. For $t_d \gtrsim 0.1$ Gyr, hBH2s are formed through the CE0 channel (see also Figure 11). This is the reason why the primary BHs can have larger masses than the He core formed from stars with $M_{\text{ZAMS}} = 300M_\odot$. The 2D distributions have shapes like parallelograms. This means hBH2s have two BHs with similar masses. This is because the second mass transfer tends to stop when the mass ratio of the binary becomes close to unity, similarly to hBH0s around the lower-mass peak in the optiq0.0a1e1 model.

For $q_{\min} = 0.9$ or $a_{\min} = 200R_\odot$, the mass distributions in all t_d are similar to that in $t_d \lesssim 0.1$ Gyr in the optiq0.0a1e1 model. In other words, all of the hBH2s are formed only through the CE4 channel. This is because the CE0 channel does not work. As seen in Figure 11, the CE0 channel works well only when $q_i < 0.9$ (the top panel) and $a_i < 200R_\odot$ (the left-hand side of the vertical dashed line). For $q_i \geq 0.9$, two stars fill their Roche lobes simultaneously. Then, they experience a merger or common-envelope evolution. They merge when they are MS stars, and they experience common-envelope evolution when they are post-MS stars. Thus, they cannot go through the CE0 channel. For $a_i \geq 200R_\odot$, binaries can go through the CE0 channel. However, the resulting BH-BHs have separations that are too large to merge in $t_d \leq 15$ Gyr, because the CE0 channel does not shrink binary separations.

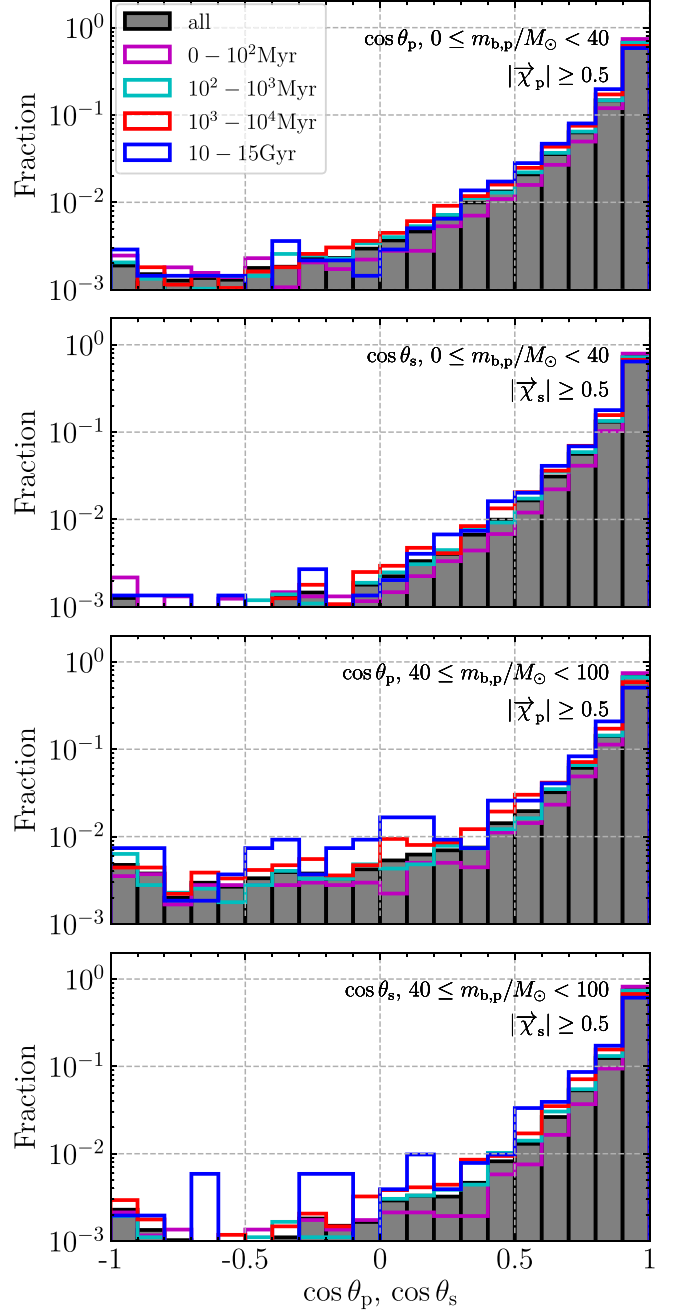


Figure 21. Distribution of angles between the primary and secondary BH spin vectors and binary orbit vectors for $0 \leq m_{b,p}/M_\odot < 40$ (the top two panels), and $40 \leq m_{b,p}/M_\odot < 100$ (the bottom two panels) in the kickq0.0a1e1 model. The BHs are limited to those with $|\vec{\chi}_p| \geq 0.5$ or $|\vec{\chi}_s| \geq 0.5$.

Natal kicks erase the t_d dependence. Thus, hBH2s formed through the CE0 channel appear for $t_d \lesssim 0.1$ Gyr, and the 2D distributions have shapes like parallelograms for all t_d . Stellar winds erase hBH2s formed through the CE0 channel. The first-evolving star fills its Roche lobe when it is an MS star. It is spun up and loses a large amount of mass due to rotationally enhanced stellar winds. Because it makes a He core with mass smaller than $M_{c,\text{He,DC}} (= 135M_\odot)$ due to the stellar winds, it experiences PISN. Thus, the shapes of the 2D distributions for all t_d are triangle-like, similar to that for $t_d = 0\text{--}0.1$ Gyr in the optiq0.0a1e1 model. This is the same if both natal kicks and stellar winds are taken into account (i.e., the pess models). The

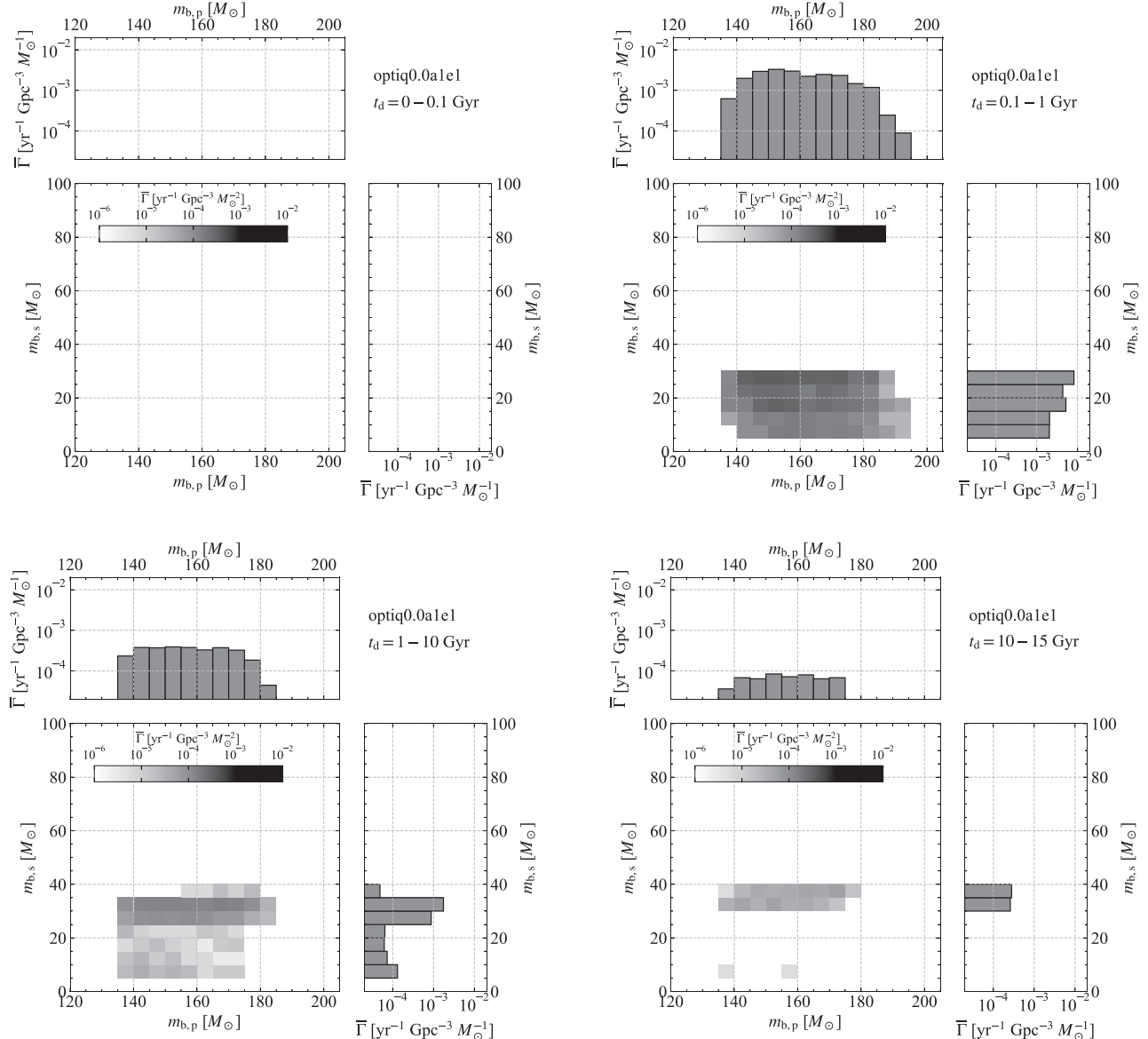


Figure 22. Merger rate densities of hBH1s in the optiq0.0a1e1 model.

mass distributions in models with different initial conditions and single star models can be understood as simple combinations of the effects described above.

Figure 27 shows the spin distribution of the primary and secondary BHs of hBH2s in the optiq0.0a1e1 model. The fraction of BHs with high spins decreases with t_d because of the spin– t_d relation. A large number of BHs have low spins, ~ 0.2 , for $t_d = 10 - 15$ Gyr. Note that their spins are nonzero. Because they are formed through the CE0 channel, they can retain their H envelopes and spin angular momenta until their collapse.

Different initial conditions make the spin distribution smaller, especially for $t_d = 10 - 15$ Gyr. Figure 28 shows the spin distribution of hBH2s in the optiq0.0a2e2 model. Most primary and secondary BH spins are zero for $t_d = 10 - 15$ Gyr in contrast to those in the optiq0.0a1e1 model. This is because hBH2s for $t_d = 10 - 15$ Gyr are formed only through the CE channel. Note that the corresponding hBH2s in the optiq0.0a1e1 model are formed predominantly through the CE channel. Because the CE4 channel carries away the H envelopes of the progenitors of both primary and secondary

BHs, the resulting BHs have lower spins than the BHs formed through the CE0 channel.

Natal kicks erase the t_d dependence of the spin distribution, and the spin distribution for each t_d is similar to that for $t_d = 0 - 15$ Gyr. Stellar winds decrease both the primary and secondary spins. Most of the BH spins are zero for $t_d = 10 - 15$ Gyr. When both initial conditions and single star models are different from the optiq0.0a1e1 model, we can interpret the spin distributions as simple combinations of the effects described above.

Natal kicks increase the spin–orbit misalignments of hBH2s. We show in Figure 29 the distribution of the misalignments. The misalignments are clearly weaker than those of hBH0s (see Figure 21) because of their larger internal velocities as discussed in Section 3.3.2. However, the misalignments appear similar to those of hBH1s (see Figure 25). There can be two reasons. First, the difference between the internal velocities of hBH1s and hBH2s is smaller than the difference between the internal velocities of hBH0s and hBH1s. Second, the number of hBH1s and hBH2s is small, $\sim 10^3$ of 10^6 binaries.

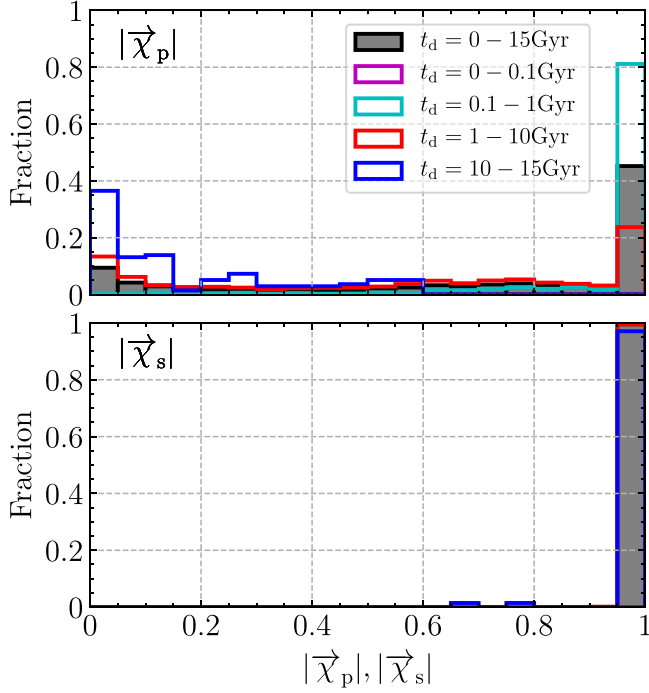


Figure 23. Spin distributions of the primary and secondary BHs in hBH1s for each t_d in the optiq0.0a1e1 model.

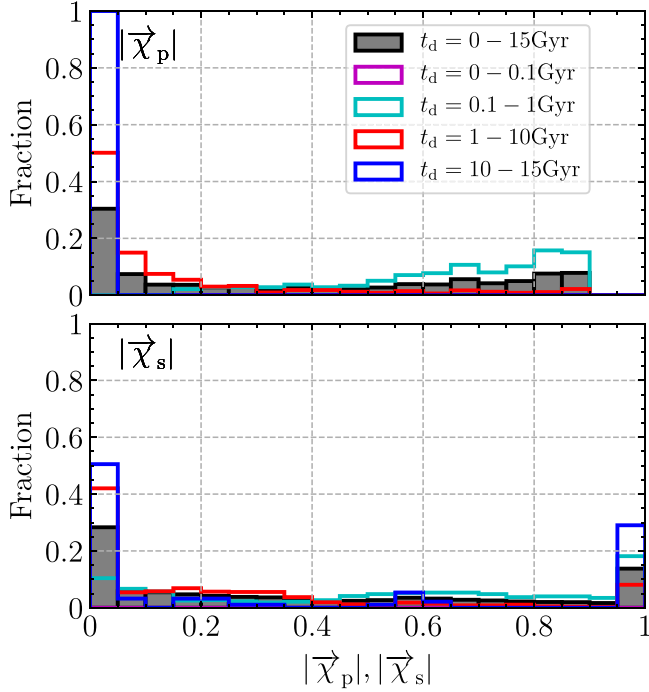


Figure 24. Spin distribution of the primary and secondary BHs in hBH1s for each t_d in the windq0.0a1e1 model.

We summarize the features of hBH2s. In the optiq0.0a1e1 model, they are formed through the CE0 and CE4 channels. The CE4 and CE0 channels are dominant for $t_d = 0\text{--}0.1$ and $0.1\text{--}15$ Gyr, respectively. Thus, the mass distribution is limited to He core masses in $130\text{--}180 M_\odot$ for $t_d = 0\text{--}0.1$ Gyr, while it extends to $\sim 200 M_\odot$, because BHs keep their H envelopes. The 2D mass distributions have a triangular-like shape for $t_d = 0\text{--}0.1$ Gyr, and parallelogram-like shapes for $t_d = 0.1\text{--}15$ Gyr. The primary

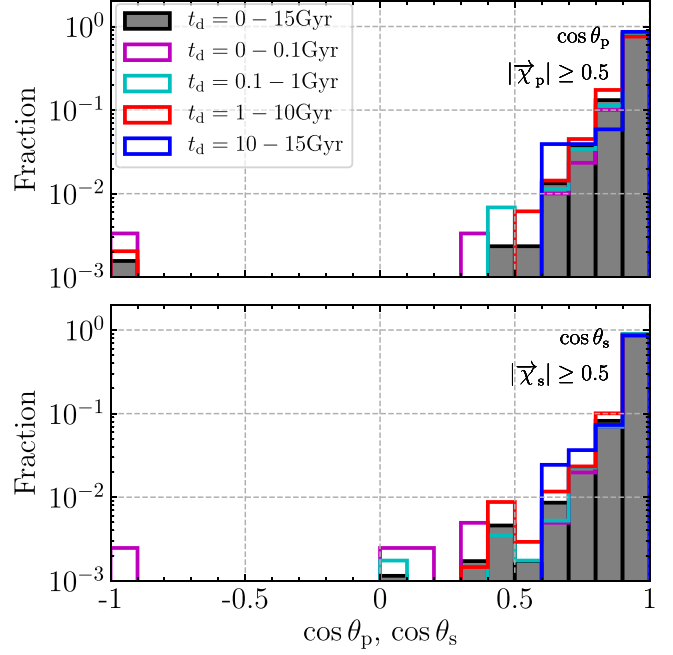


Figure 25. Distribution of angles between the primary and secondary BH spin vectors and binary orbit vectors for hBH1s in the kickq0.0a1e1 model. The BHs are limited to those with $|\vec{\chi}_p| \geq 0.5$ or $|\vec{\chi}_s| \geq 0.5$.

and secondary BH spins decrease with t_d due to the spin- t_d relation, and they only have ~ 0.2 for $t_d = 10\text{--}15$ Gyr. If initial conditions are different or stellar winds are switched on, hBH2s formed through the CE0 channel vanish. Their mass distributions for all t_d have triangular-like shapes, similar to those for $t_d = 0\text{--}0.1$ Gyr in the optiq0.0a1e1 model. BH spins decrease with t_d , and most of them are zero for $t_d = 10\text{--}15$ Gyr. Natal kicks erase the t_d dependence, and increase spin-orbit misalignments smaller than those of hBH0s and similar to those of hBH1s. Mass and spin distributions with different initial conditions and single star models can be interpreted as simple combinations of their effects.

4. Identification of Population III BH–BHs

We discuss the possibility of identifying Population III BH–BHs with the current and future GW observatories. In Section 4.1, we compare our results with previous events of BH–BH mergers, and present clues to identify Population III BH–BHs if Population III BH–BHs are contained in previous and near-future events detected by the current GW observatories. In Section 4.2, we examine how to find Population III BH–BHs using future GW observatories. Figures 14 and 15 will be helpful also in this section.

4.1. Current GW Observatories

In Sections 4.1.1 and 4.1.2, we discuss hBH0s and hBH1s/hBH2s, respectively.

4.1.1. Binaries with Two Low-mass BHs (hBH0)

As described above, the merger rate of Population III BH–BHs at the present day (or $t_d \sim 10$ Gyr) is $\sim 0.1 \text{ yr}^{-1} \text{ Gpc}^{-3}$, much smaller than inferred by LIGO/Virgo observations by two or three orders of magnitude. However, the merger rate density of Population III BH–BHs should be largely influenced by the total mass density of Population III stars, which contains

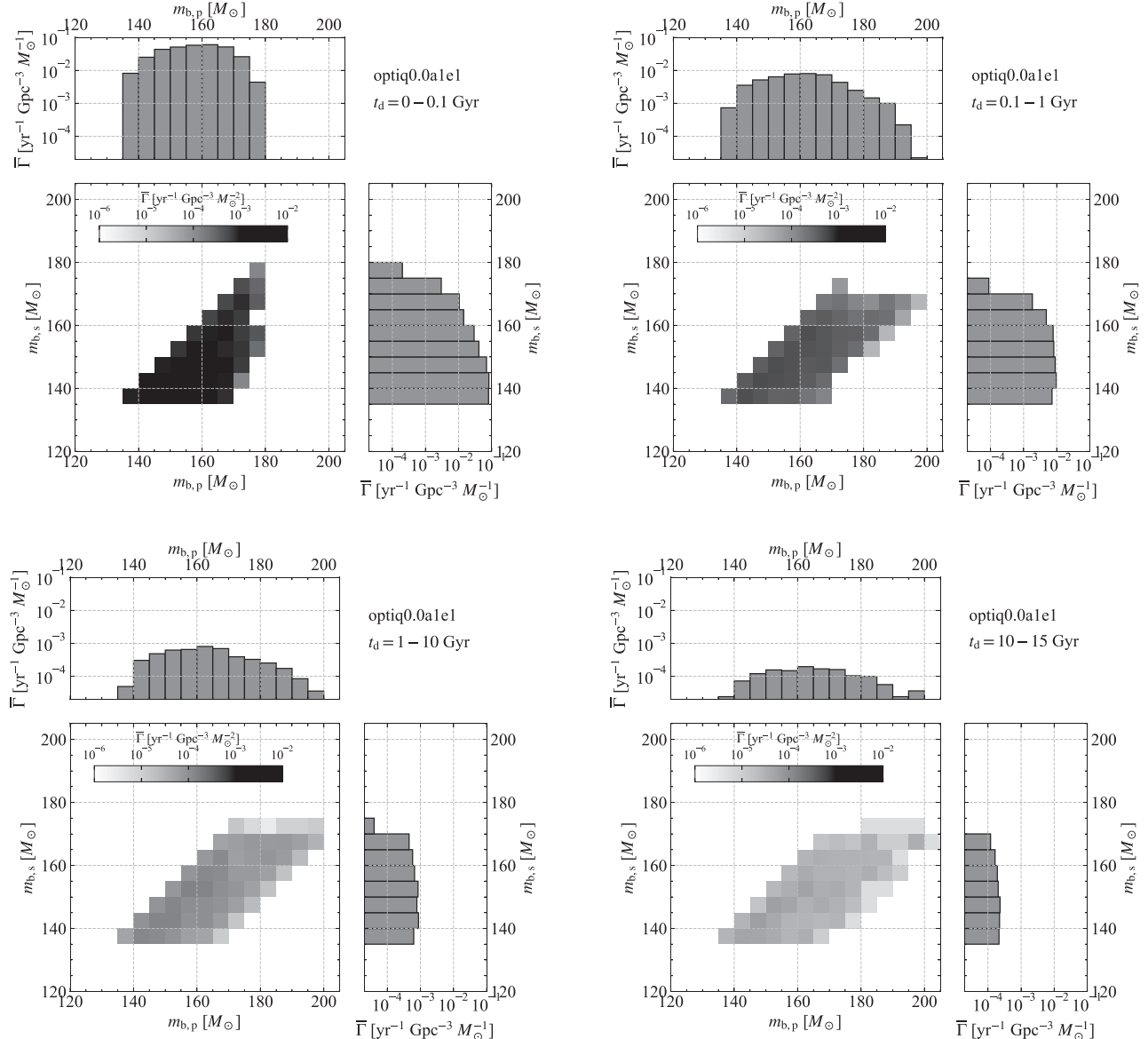


Figure 26. Merger rate densities of hBH2s in the optiq0.0a1e1 model.

large uncertainties. Hereafter, we compare the Population III hBH0's mass and spin distributions with observed BH–BHs. These distributions should not be affected by the total mass density of Population III stars.

Here, we focus on the lower-mass ($\sim 30 M_{\odot}$) peak of Population III hBH0s. As seen in Figure 15, a high fraction of hBH0s have high χ_{eff} if the peak is present. Because this peak is unique to Population III hBH0s, it can be a clue to identify Population III BH–BHs. We do not mention the higher-mass ($\sim 45 M_{\odot}$) peak despite it being present regardless of different initial conditions (q_{\min} and a_{\min}) and different stellar evolution models (stellar winds and natal kicks). This is because it is also predicted for Population I/II hBH0s.

We compare the $m_{b,p}$ distributions for $t_d = 10-15$ Gyr with observed BH–BHs. From GW observations, Abbott et al. (2020d) inferred that the merger rate density has a global maximum at $7.8^{+2.2}_{-2.1} M_{\odot}$. No model in this paper indicates such a global maximum as seen in Figures 16, 18, and 19. Population III binaries may not cover all BH–BHs observed by the current GW observatories.

We examine whether Population III binaries can explain a possible subcomponent of currently observed BH–BHs. Here, we focus on a peak at $30-40 M_{\odot}$ in the merger rate density shown by GW observations (Abbott et al. 2020d). If we increase the total mass density of Population III stars 30–100 times, the Population III merger rate density at the lower-mass peak (see Figure 16) can be matched with the observed BH–BH merger rate density at around $\sim 30 M_{\odot}$ ($\sim 0.3 \text{ yr}^{-1} \text{ Gpc}^{-3} M_{\odot}^{-1}$). However, most of the observed BH–BHs have $\chi_{\text{eff}} \lesssim 0.4$ (Abbott et al. 2020d), while most of the Population III hBH0s around the lower-mass peak have $\chi_{\text{eff}} \sim 1$. It may be difficult to claim that the observed $30-40 M_{\odot}$ peak is formed from Population III hBH0s. Note that BH spins can depend on models of tidal interaction and mass transfer (Kinugawa et al. 2020).

Hereafter, we assess whether Population III hBH0s can explain the rare events discovered in the first half of the third observing run by LIGO and Virgo. The rare events are GW190412, GW190814, and GW190521.

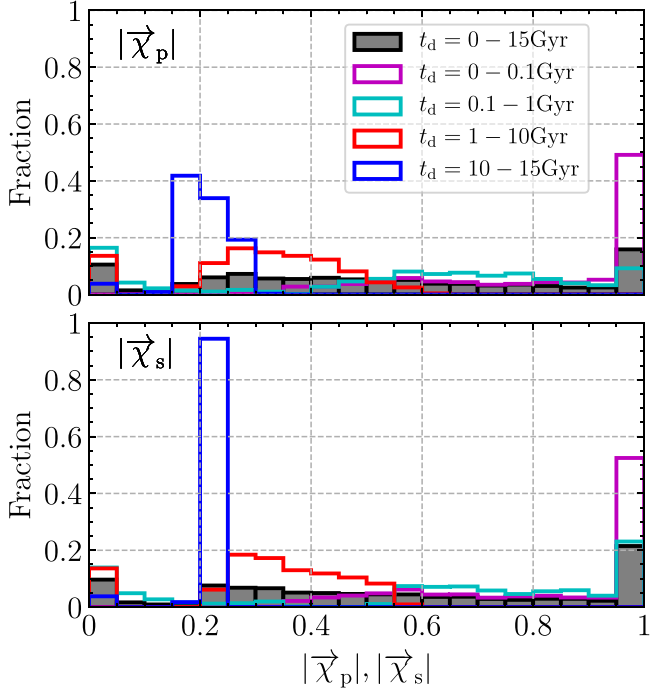


Figure 27. Spin distributions of hBH2s for each t_d in the optiq0.0a1e1 model.

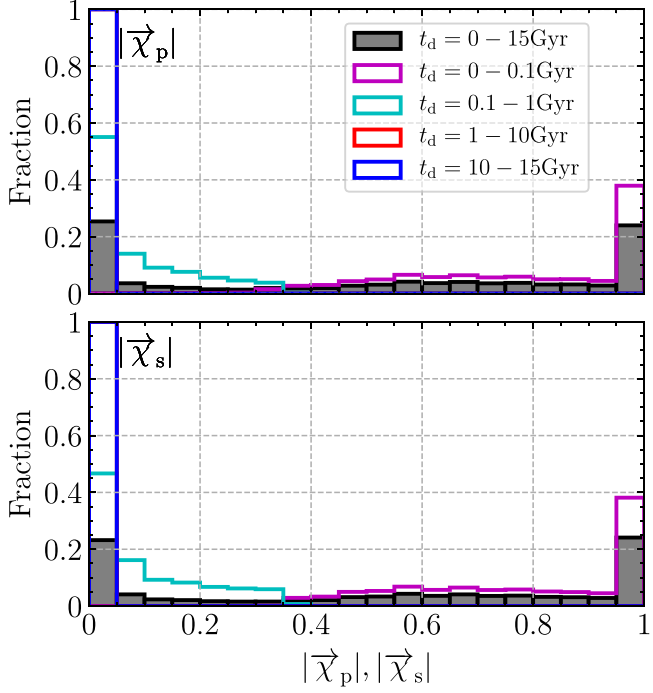


Figure 28. Spin distributions of hBH2s for each t_d in the optiq0.0a2e2 model.

GW190412 has $m_{b,p} \sim 30M_\odot$, $m_{b,s} \sim 8M_\odot$, $\chi_{\text{eff}} \sim 0.28$, and $|\vec{\chi}_p| \sim 0.31$ (Abbott et al. 2020a). Some studies have pointed out that the secondary BH may have a high spin, and the primary BH may not have a high spin (e.g., Olejak et al. 2020; Safarzadeh & Hotokezaka 2020). On the other hand, reanalysis by Zevin et al. (2020) have supported the primary BH being a spinning BH. In either case, Population III hBH0s in our results cannot explain this event, because Population III hBH0s with $m_{b,p} \sim 30M_\odot$ should have high spins (but see Kinugawa et al. 2020).

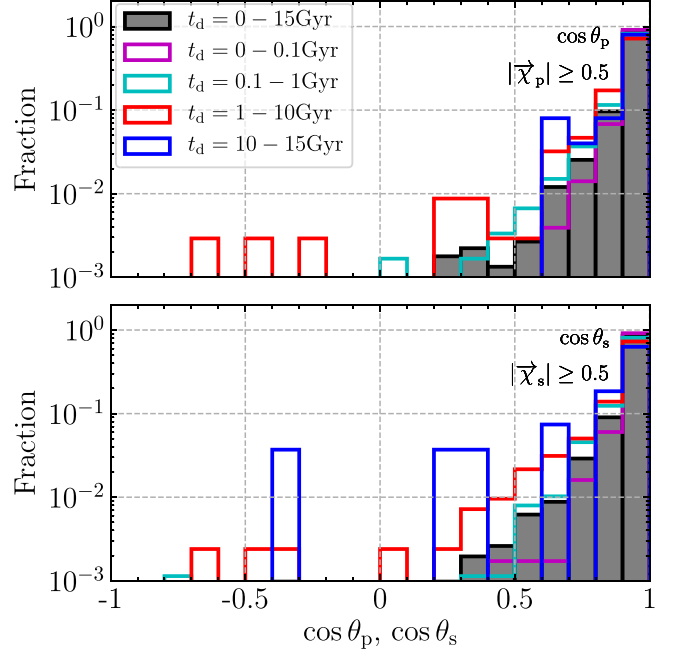


Figure 29. Distribution of angles between the primary and secondary BH spin vectors and the binary orbit vectors for hBH2s in the kickq0.0a1e1 model. The BHs are limited to those with $|\vec{\chi}_1| \geq 0.5$ or $|\vec{\chi}_2| \geq 0.5$.

Our supernova model is a rapid model in which BHs in the lower-mass mass gap are not formed. Thus, our models have no hBH0 like GW190814, which contains a $2.6M_\odot$ compact object (Abbott et al. 2020c). Kinugawa et al. (2021b) have chosen a supernova model with a lower-mass gap, and have suggested that GW190814-like events can happen under Population III environments.

GW190521 has $m_{b,p} \sim 85M_\odot$ and $m_{b,s} \sim 66M_\odot$ (Abbott et al. 2020b). Unfortunately, our models cannot form mass combinations like GW190521 as seen in Figure 8 (but see Liu & Bromm 2020b; Safarzadeh & Haiman 2020; Tanikawa et al. 2020b; Farrell et al. 2021; Kinugawa et al. 2021a). However, GW190521 can be interpreted as a BH–BH with hBH and IBH (Fishbach & Holz 2020; Nitz & Capano 2021). We discuss the possibility that GW190521 may be a Population III hBH1 in Section 4.1.2.

We summarize this section. We compare Population III hBH0s with observed BH–BHs. Even if we match the merger rate density of Population III hBH0s with that of observed BH–BHs by increasing the Population III formation rate by two or three orders of magnitude, Population III hBH0s cannot explain a global maximum at $\sim 8M_\odot$ in observed BH–BHs. The $\sim 30M_\odot$ peak of Population III hBH0s may not be consistent with that of observed BH–BHs, because Population III hBH0s have much higher spins than observed ones. GW190412 and GW190814 are unlikely to be Population III hBH0s according to our Population III models.

4.1.2. Binaries Including hBHs (hBH1 and hBH2)

María Ezquiaga & Holz (2021) have shown that the current GW observatories are most sensitive to BH–BHs with the total masses of $\sim 200M_\odot$, which is similar to the total masses of hBH1s and hBH2s. Hence, we discuss the properties of Population III hBH1s and hBH2s, and their difference from others. We focus on the characteristic features of Population III

hBH1 and hBH2 weakly depending on initial conditions (q_{\min} and a_{\min}) and stellar evolution models (stellar winds and natal kicks), as described in Figure 15.

First, we compare Population III BH–BHs with those in globular clusters (GCs) (Rodriguez et al. 2019; Kimball et al. 2020), nuclear star clusters (NSCs) at galactic centers (Antonini & Rasio 2016; Belczynski & Banerjee 2020), open clusters (OCs; Banerjee 2019; Di Carlo et al. 2020a), and triple and quadruple systems (TS and QS, respectively; Fragione et al. 2020). In these scenarios, hBHs grow through stellar or BH mergers. Because these mergers should not be frequent, the ratio of hBHs to IBHs should not be high. Thus, the ratio of hBH2s to hBH1s should be much smaller than the Population III ratio. Many discoveries of hBH1s and hBH2s can distinguish Population III ones from the others. Moreover, because those with GC and NSC origins involve BH mergers, most of them should have high χ_{eff} . On the other hand, at least half of Population III ones have low χ_{eff} .

Gas accretion can increase BH masses up to the mass range of hBHs (e.g., Roupas & Kazanas 2019). This should make hBHs highly spinning. Thus, hBH1s and hBH2s in this scenario should have high χ_{eff} . On the other hand, at least half of Population III hBH1s and hBH2s have low χ_{eff} . Thus, they can be identified from those formed through gas accretion.

We compare our BH–BHs with Population III BH–BHs formed dynamically (Liu & Bromm 2020a). Their BH–BHs have $m_{\text{b,p}} \gtrsim 250M_{\odot}$ in contrast to our BH–BHs with $m_{\text{b,p}} \gtrsim 130M_{\odot}$. This is because each BH evolves as a single star and does not lose its mass through binary interactions, such as mass transfer, common envelope, and rotationally enhanced stellar winds. Their BH–BHs should have a high χ_{eff} different from Population III BH–BHs, because it gets extra mass through gas accretion. Eventually, using hBH masses and spins, we can distinguish whether Population III BH–BHs are formed through binary evolution or dynamical interaction.

Mangiagli et al. (2019) have examined merger rates of Population I/II hBH1s and hBH2s. Their merger rates are $\sim 10^{-2} \text{ yr}^{-1} \text{ Gpc}^{-3}$, comparable with the merger rates of the Population III hBH1s and hBH2s we estimate. It may be difficult to distinguish Population III hBH1s and hBH2s from Population I/II ones if we confine ourselves to discussing merger events in the current universe. Although Mangiagli et al. (2019) have not presented detailed properties, such as $m_{\text{b,p}}$, $m_{\text{b,s}}$, $\vec{\chi}_{\text{p}}$, and $\vec{\chi}_{\text{s}}$ distribution, these properties may be similar among Population I/II/III hBH1s and hBH2s, because all of them are formed through binary evolution.

Liu et al. (2019; see also Liu et al. 2020) have discovered a $70M_{\odot}$ BH in LB-1, and have raised the possibility that massive BHs can be formed more easily than previously thought (Belczynski et al. 2020b; Groh et al. 2020). Then, Population I/II hBH1s and hBH2s may also be formed more easily. However, there are many opinions against the presence of a $70M_{\odot}$ BH in LB-1 (Abdul-Masih et al. 2020; Bodensteiner et al. 2020; El-Badry & Quataert 2020, 2021; Eldridge et al. 2020; Irrgang et al. 2020; Simón-Díaz et al. 2020; Tanikawa et al. 2020a; Yungelson et al. 2020). Thus, we do not take into account this possibility here.

Finally, we discuss GW190521. Fishbach & Holz (2020) and Nitz & Capano (2021) suggested that GW190521 may be an hBH1. Nitz & Capano (2021) have also indicated that heavier BHs are most likely to have high spin magnitude and large spin–orbit misalignment ($\gtrsim 90^\circ$). Population III hBH1s

have difficulty explaining the spin features of GW190521. If we include BH natal kicks, hBHs in hBH1s can have high spins even in the current universe, because BH natal kicks relax the spin– t_{d} relation. However, their spin–orbit misalignments are $\lesssim 60^\circ$ (see Figure 25). We have to adopt $\sigma_{\text{k}} \gg 265 \text{ km s}^{-1}$ for BH natal kicks in order to form Population III hBH1s with spins as large as GW190521.

We summarize this section. Population III BH–BHs with hBHs (hBH1s and hBH2s) can be identified from those formed through stellar or BH mergers in GCs, NSCs, OCs, and TS/QSs, or through gas accretion by the ratio of the hBH1s to hBH2s and the hBH spins. On the other hand, it is difficult to distinguish between Population III and Population I/II BH–BHs. Although GW190521 may consist of an hBH and IBH similar to Population III hBH1s, the spin–orbit misalignment of GW190521 cannot be explained by Population III hBH1s, unless we adopt BH natal kicks with $\sigma_{\text{k}} \gg 265 \text{ km s}^{-1}$.

4.2. Future GW Observatories

Future ground-based GW observatories, such as the Einstein Telescope (Punturo et al. 2010; Maggiore et al. 2020) and Cosmic Explorer (Reitze et al. 2019), can detect hBH0s at the high-redshift universe. Moreover, future space-borne GW observatories, such as DECIGO (Kawamura et al. 2006), may observe hBH1s and hBH2s at the high-redshift universe. In this section, we discuss the t_{d} dependence of Population III hBH0s, hBH1s, and hBH2s, and suggest clues to identify Population III BH–BHs from other BH–BHs.

First, we note a feature unique to Population III BH–BHs, which are common to Population III hBH0s, hBH1s, and hBH2s. Because Population III stars are formed much earlier than Population I/II stars, Population III BH–BHs can be observed at a higher-redshift universe (say $z \sim 10$) than Population I/II BH–BHs ($z \sim 2$, when stars are most actively formed; Madau & Dickinson 2014). If Population III BH–BHs dominate the observed BH–BHs contrary to our results, the BH–BH merger rate density should have $\Gamma \propto t_{\text{d}}^{-1}$ beyond $z \sim 2$ regardless of the initial conditions and stellar models (see Figure 9).

Population III hBH0s have two time-evolving features in the optiq0.0a1e1 model (see also Figure 14):

1. Time evolution of the lower-mass peak in BH mass distribution from $20M_{\odot}$ to $35M_{\odot}$.
2. High fraction of high effective spins (~ 1) around the lower-mass peak.

These features can be strong evidence for the presence of Population III BH–BHs, even if Population III BH–BHs are not dominant GW sources. This t_{d} dependence is quite different from BH–BHs formed in other places. Santoliquido et al. (2020) do not find the cosmic evolution of mass distributions of BH–BHs formed through binary evolution and open clusters. Although BH–BH masses can evolve if GC-origin BH–BHs are dominant, their masses should decrease with time, because more massive BHs join BH–BHs and merge at an earlier time (e.g., Tanikawa 2013).

Population III hBH1s and hBH2s have two time-evolving features in the optiq0.0a1e1 model (see also Figure 14):

1. Decrease of the maximum $m_{\text{b,p}}$ with t_{d} for hBH1s.
2. Larger maximum $m_{\text{b,p}}$ mass for $t_{\text{d}} \gtrsim 0.1 \text{ Gyr}$ than for $t_{\text{d}} \lesssim 0.1 \text{ Gyr}$ for hBH2s.

These features can be clues to identify Population III hBH1s and hBH2s. Because the Population III formation epoch is much earlier than those of NSCs, GCs, OCs, TC/QCs, and Population I/II binaries, the Population III BH mass evolves earlier.

We summarize this section. The time evolution of the merger rate densities of hBH0s, hBH1s, and hBH2s can be a clue to identify Population III BH–BHs. If Population III BH–BHs are dominant, the BH–BH merger rate density keeps $\Gamma \propto t_d^{-1}$ beyond $z \sim 2$ regardless of the initial conditions and stellar models. For ideal conditions (i.e., the optiq0.0a1e1 model), the time evolution of BH mass distributions can be clues to identify Population III BH–BHs. Population III hBH0s have LBHs with a larger mass for larger t_d , and with high spin ~ 1 . The maximum $m_{b,p}$ mass of Population III hBH1s and hBH2s evolves earlier than those of other scenarios. No other scenario has suggested such time evolution.

5. Discussion

5.1. Chemically Homogeneous Population III Stars

So far, we have assumed that Population III stars have small stellar rotations at their ZAMS times. However, they can have large stellar rotations. In fact, the poloidal magnetic field around Population III stars is weaker than the turbulent field and toroidal field (Sharda et al. 2020). Thus, the magnetic braking effect to spin down the protostar could be inefficient. Furthermore, the abundant nitrogen in EMP stars suggests that Population III stars are fast rotators (e.g., Chopping et al. 2019). If they have large stellar rotations at their ZAMS times, they can switch on CHEs (e.g., Yoon et al. 2012, for Population III stars). Here, we make two simple models for Population III binary evolutions under CHEs, and estimate BH–BH merger rates. In the first model, we assume that a whole star evolves to a nHe star without stellar wind mass loss, and that a binary does not change its orbit without any interactions, such as tidal interaction, mass transfer and common envelope. The assumption of no binary interaction can be justified by the fact that the stars enter into CHEs due to their initial rotations (not due to tidal spin up), and do not expand so much. Such a resulting nHe star experiences supernova and PPI/PISN described in Section 2.1, and leaves an NS, BH, or no remnant. Because an nHe star with $\lesssim 10M_\odot$ and $45\text{--}65M_\odot$ loses part of its mass at supernova, the binary orbit should be changed. However, we ignore this effect for simplicity. In the second model, we assume that a star evolves to an nHe star, losing 30% of its ZAMS mass due to stellar winds, which is roughly consistent with the results of Yoon et al. (2012). We adiabatically change the binary orbital parameters through stellar winds so that the binary period is inversely proportional to the square of the total mass, and the eccentricity is constant. The nHe star experiences supernova in the same way as the first model, and the supernova does not change the binary orbital parameters.

Figure 30 shows the merger rate densities of Population III hBH0s, hBH1s, and hBH2s as a function of t_d when all Population III stars are CHEs. If $a_{\min} = 10R_\odot$, the hBH0, hBH1, and hBH2 merger rates for the CHE case are comparable to, or more than, those for the non-CHE cases in the present-day universe ($t_d = 10\text{--}15$ Gyr). Because we ignore stellar mergers before stars collapse to BHs, we overestimate the merger rates for $t_d \lesssim 0.1$ Gyr. However, binaries forming BH–BHs with $t_d \sim 10$ Gyr have much larger semimajor axes than nHe star radii, and thus, they should not

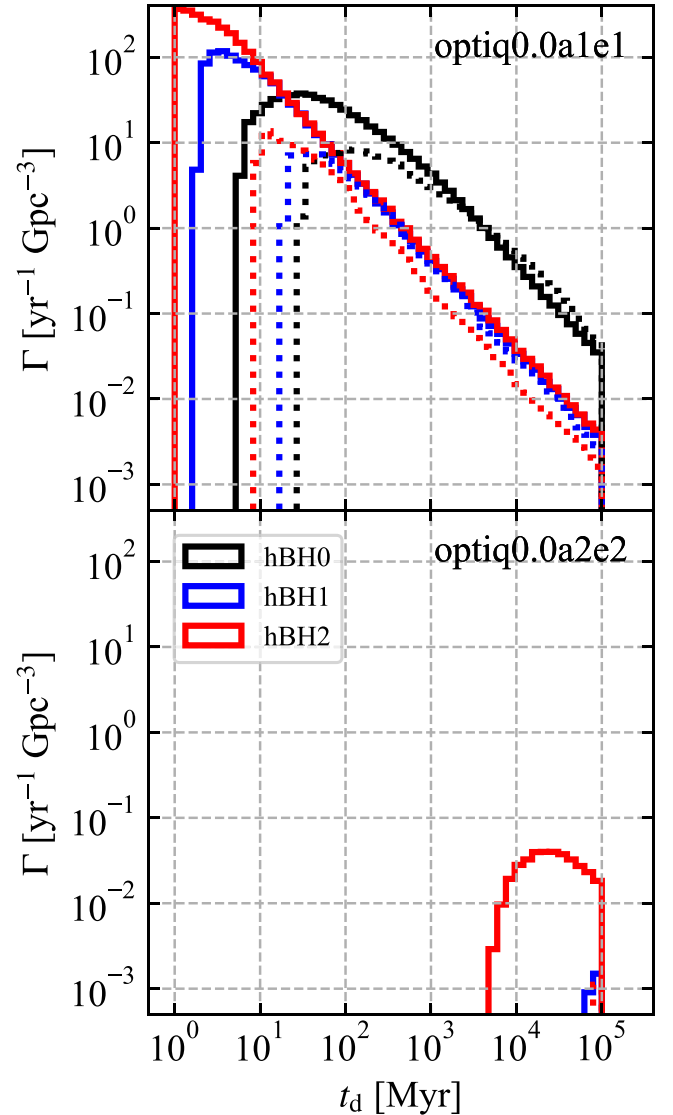


Figure 30. Merger rate densities of Population III hBH0s, hBH1s, and hBH2s as a function of t_d when all Population III stars experience CHEs with initial conditions of the optiq0.0a1e1 and optiq0.0a2e2 models (the top and bottom panels, respectively). The solid and dashed curves indicate the first and second models, respectively.

experience stellar mergers before their members collapse into BHs. Thus, the merger rates for $t_d \sim 10$ Gyr should be correct. If $a_{\min} = 200R_\odot$, hBH0s and hBH1s never merge at any time. If we take into account stellar wind mass loss, even hBH2s have no chance of merging for $t_d \leq 15$ Gyr. This shows that a_{\min} plays a crucial role if Population III stars have large stellar rotations and enter into CHEs. Here, we stop discussing CHEs. It is beyond of the scope of this paper to determine a_{\min} and whether Population III stars enter into CHEs or not.

5.2. Sensibility to λ_{CE}

We set $\lambda_{CE} = 1$ in Section 3. However, λ_{CE} is quite uncertain, and Klencki et al. (2021) have shown that λ_{CE} can be 0.01. For the optiq0.0a1e1 and optiq0.0a2e2 models, we change λ_{CE} to 0.1 and 0.01, and perform binary population synthesis calculations. Figure 31 shows their merger rate densities. We find that λ_{CE} has small effects on the merger rates of hBH0s and hBH2s in the optiq0.0a1e1 models (see also

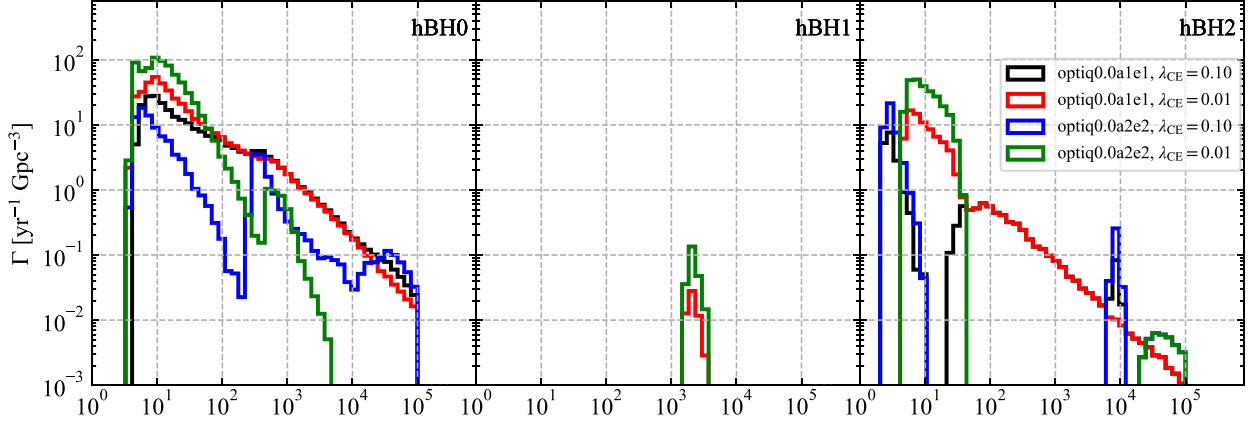


Figure 31. Merger rate densities of hBH0, hBH1, and hBH2 as a function of the delay time in the optiq0.0a1e1 and optiq0.0a2e2 models, where we set $\lambda_{\text{CE}} = 0.1$ and 0.01. The left, middle, and right panels indicate the merger rate densities of hBH0s, hBH1s, and hBH2s, respectively.

Figure 9). This is because a significant part of hBH0s and hBH2s in these models are formed through the CE0 channel not involving common-envelope evolution. On the other hand, hBH1s in all models and hBH0s and hBH2s in the optiq0.0a2e2 models drastically decrease with λ_{CE} decreasing. This is because they are formed through channels involving common-envelope evolution. Klencki et al. (2021) have also reported that it is harder for common-envelope evolution to take place than previously thought when a donor star is massive ($\geq 40M_{\odot}$) and a BSG star. If so, the dependence on λ_{CE} would become stronger.

5.3. BHs in the PI Mass Gap

In Section 3, we obtain BHs in the PI mass gap; however, their masses are at most $\sim 55M_{\odot}$. We examine the initial conditions and single star models in which BHs with $\sim 80M_{\odot}$ emerge. Note that the possible maximum mass of BHs in the PI mass gap is $\sim 85M_{\odot}$ in our single star model (see Figure 3). We modify the optiq0.0a1e1 model and prepare the following initial conditions. We extend the maximum semimajor axis from $2000R_{\odot}$ to 10^5R_{\odot} , and account for natal kicks with $\sigma_k = 50 \text{ km s}^{-1}$. We call this parameter set ‘‘PI-mass-gap’’ model.

Figure 32 shows the merger rate densities of Population III BH–BHs as a function of t_d in the PI-mass-gap model. The merger rate densities of hBH0s, hBH1s, and hBH2s are similar to those in the optiq0.0a1e1 model (see black curves in the upper panels of Figure 9). We can find BH–BHs with BHs in the PI mass gap. Their merger rate densities of $m_{\text{b,p}} > 50M_{\odot}$ and $m_{\text{b,p}} > 65M_{\odot}$ are $\sim 10^{-4} \text{ yr}^{-1} \text{ Gpc}^{-3}$ for $t_d = 10 \text{ Gyr}$. Even Population III BH–BHs with two BHs in the PI mass gap are present, although their merger rate is quite small. Among the 16 main models, the kickq0.9a2e2 model has the most BH–BHs with BHs in the PI mass gap. The merger rate density of $m_{\text{b,p}} > 50M_{\odot}$ is comparable to that of the PI-mass-gap model. On the other hand, the merger rate density of $m_{\text{b,p}} > 65M_{\odot}$ is much smaller than that of the PI-mass-gap model. Actually, the number of BH–BHs is too small to calculate the merger rate density. In contrast to the 16 main models, the PI-mass-gap model can have plenty of BH–BHs with BHs in the PI mass gap ranging from $50M_{\odot}$ to $85M_{\odot}$.

We draw a schematic picture of a formation channel for BH–BHs with BHs in the PI mass gap in Figure 33. There are two key points. First, the two stars do not fill their Roche lobes until the first-evolving star collapses to the first BH. Thus, the first-

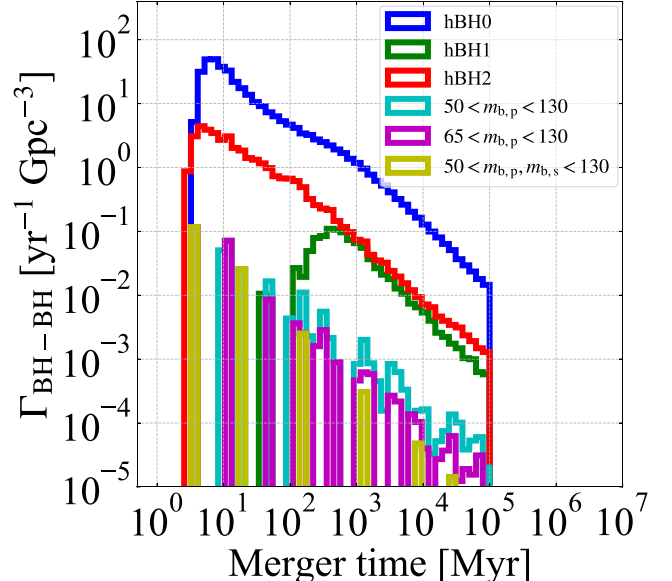


Figure 32. Merger rate densities of Population III BH–BHs as a function of t_d in the PI-mass-gap model. Here, the maximum mass of IBHs is defined as $50M_{\odot}$, and the minimum mass of hBHs is defined as $130M_{\odot}$.

evolving star keeps its H envelope, avoids PPI/PISN effects owing to its small He core with $< 45M_{\odot}$, and leaves a BH in the PI mass gap (see also Figure 3). Note that the first-evolving star is mildly spun up by the tidal field of the second-evolving star; however, it loses little mass even if we consider rotationally enhanced stellar winds. Second, a natal kick exerted on the first BH makes the binary eccentricity extremely high (~ 0.99), because the natal kick velocity is comparable to the orbital velocity of the binary. Then, the second-evolving star expands, touches the first BH, and drives common-envelope evolution. These two points finally make compact BH–BHs.

The PI-mass-gap model can form BH–BHs whose masses are similar to GW190521’s masses. However, their merger rate density of $\sim 10^{-4} \text{ yr}^{-1} \text{ Gpc}^{-3}$ is much smaller than the GW190521-like one, $\sim 10^{-1} \text{ yr}^{-1} \text{ Gpc}^{-3}$ (Abbott et al. 2020b). If we increase the total Population III mass density in the local universe by three orders of magnitude, we can match their merger rate density with the observed one. However, as a side effect, the merger rate densities of hBH0s, hBH1s, and hBH2s also increase

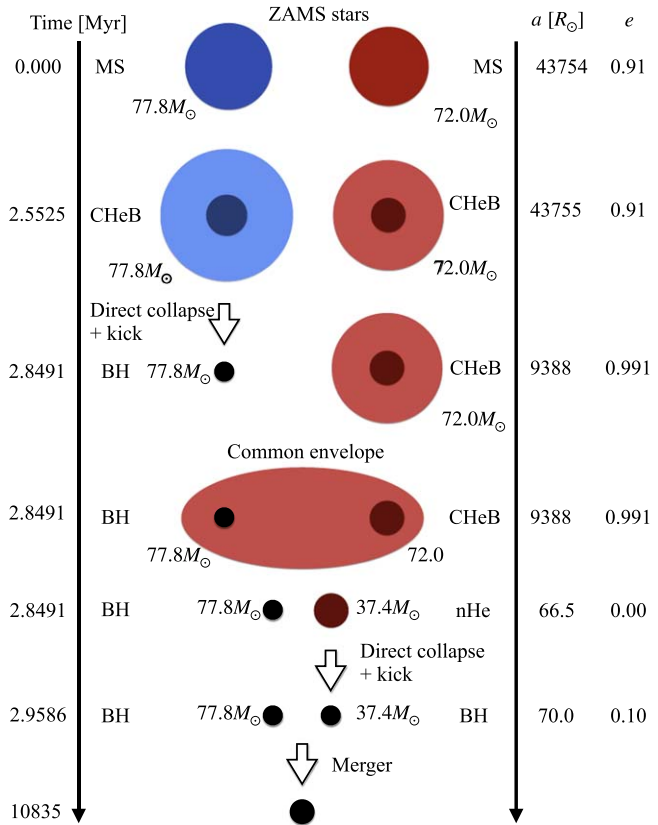


Figure 33. Example binary evolution leading to a BH–BH containing a BH in the PI mass gap.

to $\sim 10^2$, ~ 10 , and $\sim 10 \text{ yr}^{-1} \text{ Gpc}^{-3}$. These are not consistent with the observed merger rate density of hBH0s and the upper limit of the merger rate densities of hBH1s and hBH2s derived by María Ezquiaga & Holz (2021). We conclude that the PI-mass-gap model cannot explain the GW190521-like events.

5.4. Population III Hierarchical Triple and Quadruple Systems

Sugimura et al. (2020) have shown the possibility that Population III stars can be usually born as stable multiple systems. There may be many interesting aspects of stable multiple systems: the formation of BHs in the PI mass gap (Fragione et al. 2020; Tanikawa et al. 2020a), excitation of binary eccentricity through the Kozai–Lidov mechanism (Kozai 1962; Lidov 1962), and so on. However, the initial conditions of Population III multiple systems are much less clearer than those of binary stars. We will study Population III multiple systems as GW sources in future.

6. Summary

We perform binary population synthesis calculations to obtain the merger rate density of Population III BH–BHs by means of the BSE code with extensions to very massive Population III stars. Our BSE code has several novel features. The extensions enable us to follow Population III stars up to $300 M_\odot$, which include stars overcoming PISN and leaving BHs above the PI mass gap. We take into account PPI/PISN effects for binary population synthesis of Population III stars. We implement rotationally enhanced stellar winds into our BSE code. In our BSE code, natal kicks tilt BH spin vectors from binary orbit vectors, and the angles can be recorded. We use

our BSE code and investigate the properties of Population III BH–BHs and their dependence on single star models (natal kicks and stellar winds) and initial conditions (the minimum mass ratio q_{\min} and the minimum binary separation a_{\min} ; see Section 2.3).

We can categorize Population III BH–BHs into three subpopulations: hBH0s, hBH1s, and hBH2s (see Figure 8). This is because the PPI/PISN effects make the PI mass gap be between ~ 50 – $130 M_\odot$. Provided that the mass density of Population III stars is $\sim 10^{13} M_\odot \text{ Gpc}^{-3}$, the merger rates of hBH0s and the sum of hBH1s and hBH2s are $\sim 0.1 \text{ yr}^{-1} \text{ Gpc}^{-3}$ and $\sim 0.01 \text{ yr}^{-1} \text{ Gpc}^{-3}$, respectively (see Figure 9). These merger rates are independent of single star models and initial conditions. Because Population III BH–BHs have several formation channels, initial conditions have small effects on their merger rates (see Figure 11). The natal kicks we adopt have velocities comparable to or smaller than the internal velocities of Population III BH–BHs, and thus they do not affect much the merger rates. Population III stars lose their H envelopes through common-envelope evolution as well as stellar winds. The presence of stellar winds has minor effects on Population III BH masses.

We summarize the features of Population III hBH0s (see also Figures 14 and 15). The merger rate density of Population III hBH0s has higher-mass ($\sim 45 M_\odot$) and lower-mass (~ 20 – $35 M_\odot$) peaks in the optiq0.0a1e1 model. The lower-mass peak shifts from $\sim 20 M_\odot$ to $\sim 35 M_\odot$ with t_d . Most of the BHs in the lower-mass peak have high spins. Although the lower-mass peak is unique to Population III hBH0s, it is fragile against initial conditions and stellar evolution models. The characteristic feature of the lower-mass peak is that BHs around the peak have high spins if the peak is present.

Although their merger rate may be much smaller than inferred from the LIGO/Virgo observations, we could identify Population III hBH0s from observed BH–BHs in the ideal case where the initial conditions are similar to those in the optiq0.0a1e1 model. The clue is the lower-mass peak and highly spinning BHs around the lower-mass peak. Future GW observatories may detect conclusive Population III BH–BHs, a group of BH–BHs with high spins, and with peaks that shift from light to heavy with t_d . The above discussions can be also seen in Section 4.1.1.

We describe the characteristic features of Population III hBH1s and hBH2s depending weakly on initial conditions (q_{\min} and a_{\min}) and stellar evolution models (stellar winds and natal kicks) as seen in Figures 14 and 15. The rate ratio of Population III hBH2s to Population III hBH1s is $\gtrsim 0.1$. Both Population III hBH1s and hBH2s have two features: (i) $m_{b,p} \gtrsim 130 M_\odot$ and (ii) a high fraction of low effective spins ($\lesssim 0.2$).

Population III hBH1s and hBH2s can soon be discovered by current GW observatories. The above features can be clues to identify Population III hBH1s and hBH2s from others. Future GW observatories should find their merger rates are clearly $\propto t_d^{-1}$ beyond a redshift of ~ 2 if Population III hBH1s and hBH2s dominate BH–BHs in this mass range. We give a detailed discussion in Sections 4.1.2 and 4.2.

Population III BHs in the PI mass gap can merge if Population III binaries have initial semimajor axes of $\sim 10^4 R_\odot$, and BHs have natal kicks of $\sim 50 \text{ km s}^{-1}$ (see Figure 33). However, their merger rate is smaller than that of the GW190521-like BH–BHs inferred from GW observations by three orders of magnitude. If we match their merger rate with

the observed merger rate of GW190521-like BH–BHs, the total merger rate of Population III BH–BHs exceeds the total merger rate of observed BH–BHs. Thus, this formation process is not appropriate for the formation of GW190521-like BH–BHs.

In the worst scenario, the merger rates of Population III hBH0s, hBH1s, and hBH2s can be nearly zero (see Figure 30). The worst scenario is realized if the following two conditions are satisfied at the same time. First, Population III stars form only wide binaries with separations of $\gtrsim 100R_{\odot}$, which is plausible, because Population III stars expand to $\sim 100R_{\odot}$ in their protostellar phases. Second, Population III stars have fast-enough rotations to excite CHEs from the beginning, which is supported by the theoretical study of Population III star formation as well as the observation of EMP stars. In order to assess whether these conditions are satisfied or not, we need extremely high-resolution and long-term hydrodynamical simulations of Population III star formation. Such simulations should consider chemical evolution, radiative transfer, magnetic fields, and so on, and would be computationally prohibitive at the current state. We expect that computational technology will rapidly evolve to achieve the above simulations, or that conclusive detections of Population III BH–BHs conversely rule out the worst scenario.

Aside from the worst scenario, we can expect that Population III hBH1s and hBH2s can be detected within a few years. Conversely, the nondetection would mean that the number of Population III stars overcoming PISNe is quite small. Thus, we may constrain the Population III IMF to be in the mass range $\gtrsim 100M_{\odot}$ in the near future.

We thank the anonymous referee for helpful comments. A.T. thanks Tilman Hartwig and Christopher Berry for fruitful discussions. This research has been supported by Grants-in-Aid for Scientific Research (17H01101, 17H01130, 17H02869, 17H06360, 17K05380, 19K03907) from the Japan Society for the Promotion of Science.

ORCID iDs

Ataru Tanikawa <https://orcid.org/0000-0002-8461-5517>
 Hajime Susa <https://orcid.org/0000-0002-3380-5302>
 Takashi Yoshida <https://orcid.org/0000-0002-8967-7063>
 Alessandro A. Trani <https://orcid.org/0000-0001-5371-3432>
 Tomoya Kinugawa <https://orcid.org/0000-0002-3033-4576>

References

- Abbott, B. P., Abbott, R., Abbott, T. D., et al. 2016, *PhRvL*, **116**, 061102
 Abbott, B. P., Abbott, R., Abbott, T. D., et al. 2019, *PhRvX*, **9**, 031040
 Abbott, R., Abbott, T. D., Abraham, S., et al. 2020a, *PhRvD*, **102**, 043015
 Abbott, R., Abbott, T. D., Abraham, S., et al. 2020b, *PhRvL*, **125**, 101102
 Abbott, R., Abbott, T. D., Abraham, S., et al. 2020c, *ApJL*, **896**, L44
 Abbott, R., Abbott, T. D., Abraham, S., et al. 2020d, arXiv:2010.14527
 Abdul-Masih, M., Banyard, G., Bodensteiner, J., et al. 2020, *Natur*, **580**, E11
 Abel, T., Bryan, G. L., & Norman, M. L. 2002, *Sci*, **295**, 93
 Amaro-Seoane, P., Audley, H., Babak, S., et al. 2017, arXiv:1702.00786
 Antonini, F., Murray, N., & Mikkola, S. 2014, *ApJ*, **781**, 45
 Antonini, F., & Perets, H. B. 2012, *ApJ*, **757**, 27
 Antonini, F., & Rasio, F. A. 2016, *ApJ*, **831**, 187
 Antonini, F., Toonen, S., & Hamers, A. S. 2017, *ApJ*, **841**, 77
 Arca Sedda, M. 2020, *ApJ*, **891**, 47
 Askar, A., Szkuldrak, M., Gondek-Rosińska, D., Giersz, M., & Bulik, T. 2017, *MNRAS*, **464**, L36
 Bae, Y.-B., Kim, C., & Lee, H. M. 2014, *MNRAS*, **440**, 2714
 Banerjee, S. 2017, *MNRAS*, **467**, 524
 Banerjee, S. 2018a, *MNRAS*, **473**, 909
 Banerjee, S. 2018b, *MNRAS*, **481**, 5123
 Banerjee, S. 2019, arXiv:1912.06022
 Barkat, Z., Rakavy, G., & Sack, N. 1967, *PhRvL*, **18**, 379
 Barkov, M. V., & Komissarov, S. S. 2010, *MNRAS*, **401**, 1644
 Bartos, I., Kocsis, B., Haiman, Z., & Márka, S. 2017, *ApJ*, **835**, 165
 Batta, A., & Ramirez-Ruiz, E. 2019, arXiv:1904.04835
 Belczynski, K., & Banerjee, S. 2020, *A&A*, **640**, L20
 Belczynski, K., Bulik, T., Fryer, C. L., et al. 2010, *ApJ*, **714**, 1217
 Belczynski, K., Bulik, T., & Rudak, B. 2004, *ApJL*, **608**, L45
 Belczynski, K., Buonanno, A., Cantiello, M., et al. 2014, *ApJ*, **789**, 120
 Belczynski, K., Heger, A., Gladysz, W., et al. 2016b, *A&A*, **594**, A97
 Belczynski, K., Hirschi, R., Kaiser, E. A., et al. 2020b, *ApJ*, **890**, 113
 Belczynski, K., Holz, D. E., Bulik, T., & O’Shaughnessy, R. 2016a, *Natur*, **534**, 512
 Belczynski, K., Kalogera, V., & Bulik, T. 2002, *ApJ*, **572**, 407
 Belczynski, K., Klencki, J., Fields, C. E., et al. 2020a, *A&A*, **636**, A104
 Belczynski, K., Ryu, T., Perna, R., et al. 2017, *MNRAS*, **471**, 4702
 Bethe, H. A., & Brown, G. E. 1998, *ApJ*, **506**, 780
 Bodensteiner, J., Shenar, T., Mahy, L., et al. 2020, *A&A*, **641**, A43
 Bond, J. R., Arnett, W. D., & Carr, B. J. 1984, *ApJ*, **280**, 825
 Bondi, H., & Hoyle, F. 1944, *MNRAS*, **104**, 273
 Bromm, V. 2013, *RPPh*, **76**, 112901
 Bromm, V., & Larson, R. B. 2004, *ARA&A*, **42**, 79
 Callister, T. A., Farr, W. M., & Renzo, M. 2020, arXiv:2011.09570
 Cameron, A. G. W., & Mock, M. 1967, *Natur*, **215**, 464
 Casares, J., Jonker, P. G., & Israelian, G. 2017, in *Handbook of Supernovae*, ed. A. W. Alsabti & P. Murdin (Cham: Springer), 1499
 Chiaki, G., Yoshida, N., & Hirano, S. 2016, *MNRAS*, **463**, 2781
 Chopin, A., Tominaga, N., & Ishigaki, M. N. 2019, *A&A*, **632**, A62
 Clark, P. C., Glover, S. C. O., Klessen, R. S., & Bromm, V. 2011a, *ApJ*, **727**, 110
 Clark, P. C., Glover, S. C. O., Smith, R. J., et al. 2011b, *Sci*, **331**, 1040
 Dayal, P., & Ferrara, A. 2018, *PhR*, **780**, 1
 de Mink, S. E., Cantiello, M., Langer, N., et al. 2009, *A&A*, **497**, 243
 de Souza, R. S., Yoshida, N., & Ioka, K. 2011, *A&A*, **533**, A32
 Di Carlo, U. N., Giacobbo, N., Mapelli, M., et al. 2019, *MNRAS*, **487**, 2947
 Di Carlo, U. N., Mapelli, M., Bouffanais, Y., et al. 2020a, *MNRAS*, **497**, 1043
 Di Carlo, U. N., Mapelli, M., Giacobbo, N., et al. 2020b, *MNRAS*, **498**, 495
 Dominik, M., Belczynski, K., Fryer, C., et al. 2012, *ApJ*, **759**, 52
 Dominik, M., Belczynski, K., Fryer, C., et al. 2013, *ApJ*, **779**, 72
 Downing, J. M. B., Benacquista, M. J., Giersz, M., & Spurzem, R. 2010, *MNRAS*, **407**, 1946
 du Buison, L., Marchant, P., Podsiadlowski, P., et al. 2020, *MNRAS*, **499**, 5941
 El Eid, M. F., & Langer, N. 1986, *A&A*, **167**, 274
 El-Badry, K., & Quataert, E. 2021, *MNRAS*, **502**, 3436
 El-Badry, K., & Quataert, E. 2020, *MNRAS*, **493**, L22
 Eldridge, J. J., & Stanway, E. R. 2016, *MNRAS*, **462**, 3302
 Eldridge, J. J., Stanway, E. R., Breivik, K., et al. 2020, *MNRAS*, **495**, 2786
 Eldridge, J. J., Stanway, E. R., & Tang, P. N. 2019, *MNRAS*, **482**, 870
 Eldridge, J. J., Stanway, E. R., Xiao, L., et al. 2017, *PASA*, **34**, e058
 Farrell, E. J., Groh, J. H., Hirschi, R., et al. 2021, *MNRAS*, **502**, L40
 Fishbach, M., & Holz, D. E. 2020, *ApJL*, **904**, L26
 Fragione, G., & Kocsis, B. 2019, *MNRAS*, **486**, 4781
 Fragione, G., Loeb, A., & Rasio, F. A. 2020, *ApJL*, **895**, L15
 Fraley, G. S. 1968, *Ap&SS*, **2**, 96
 Frebel, A., & Norris, J. E. 2015, *ARA&A*, **53**, 631
 Fryer, C. L., Belczynski, K., Wiktorowicz, G., et al. 2012, *ApJ*, **749**, 91
 Fryer, C. L., Woosley, S. E., & Heger, A. 2001, *ApJ*, **550**, 372
 Fujii, M. S., Tanikawa, A., & Makino, J. 2017, *PASJ*, **69**, 94
 Gandhi, P., Rao, A., Charles, P. A., et al. 2020, *MNRAS*, **496**, L22
 Gandhi, P., Rao, A., Johnson, M. A. C., Paice, J. A., & Maccarone, T. J. 2019, *MNRAS*, **485**, 2642
 Giacobbo, N., & Mapelli, M. 2018, *MNRAS*, **480**, 2011
 Giacobbo, N., Mapelli, M., & Spera, M. 2018, *MNRAS*, **474**, 2959
 Greif, T. H., Bromm, V., Clark, P. C., et al. 2012, *MNRAS*, **424**, 399
 Greif, T. H., Springel, V., White, S. D. M., et al. 2011, *ApJ*, **737**, 75
 Groh, J. H., Farrell, E. J., Meynet, G., et al. 2020, *ApJ*, **900**, 98
 Hamann, W. R., & Koesterke, L. 1998, *A&A*, **335**, 1003
 Hamers, A. S., Bar-Or, B., Petrovich, C., & Antonini, F. 2018, *ApJ*, **865**, 2
 Hamers, A. S., & Safarzadeh, M. 2020, *ApJ*, **898**, 99
 Hartwig, T., Volonteri, M., Bromm, V., et al. 2016, *MNRAS*, **460**, L74
 Heger, A., & Woosley, S. E. 2002, *ApJ*, **567**, 532
 Hirano, S., Hosokawa, T., Yoshida, N., et al. 2014, *ApJ*, **781**, 60

- Hirano, S., Hosokawa, T., Yoshida, N., Omukai, K., & Yorke, H. W. 2015, *MNRAS*, **448**, 568
- Hoang, B.-M., Naoz, S., Kocsis, B., Rasio, F. A., & Dosopoulou, F. 2018, *ApJ*, **856**, 140
- Hobbs, G., Lorimer, D. R., Lyne, A. G., & Kramer, M. 2005, *MNRAS*, **360**, 974
- Hong, J., Askar, A., Giersz, M., Hypki, A., & Yoon, S.-J. 2020, *MNRAS*, **498**, 4287
- Hong, J., Vesperini, E., Askar, A., et al. 2018, *MNRAS*, **480**, 5645
- Hosokawa, T., Omukai, K., Yoshida, N., & Yorke, H. W. 2011, *Sci*, **334**, 1250
- Hotokezaka, K., & Piran, T. 2017, *ApJ*, **842**, 111
- Humphreys, R. M., & Davidson, K. 1994, *PASP*, **106**, 1025
- Hurley, J. R., Pols, O. R., & Tout, C. A. 2000, *MNRAS*, **315**, 543
- Hurley, J. R., Tout, C. A., & Pols, O. R. 2002, *MNRAS*, **329**, 897
- Iben, I. J., & Renzini, A. 1983, *ARA&A*, **21**, 271
- Inayoshi, K., Hirai, R., Kinugawa, T., & Hotokezaka, K. 2017, *MNRAS*, **468**, 5020
- Inayoshi, K., Kashiyama, K., Visbal, E., & Haiman, Z. 2016, *MNRAS*, **461**, 2722
- Irrgang, A., Geier, S., Kreuzer, S., Pelisoli, I., & Heber, U. 2020, *A&A*, **633**, L5
- Kawamura, S., Nakamura, T., Ando, M., et al. 2006, *CQGra*, **23**, S125
- Kimball, C., Talbot, C., Berry, C. P. L., et al. 2020, *ApJ*, **900**, 177
- Kinugawa, T., Inayoshi, K., Hotokezaka, K., Nakuchi, D., & Nakamura, T. 2014, *MNRAS*, **442**, 2963
- Kinugawa, T., Miyamoto, A., Kanda, N., & Nakamura, T. 2016a, *MNRAS*, **456**, 1093
- Kinugawa, T., Nakamura, T., & Nakano, H. 2020, *MNRAS*, **498**, 3946
- Kinugawa, T., Nakamura, T., & Nakano, H. 2021a, *MNRAS*, **501**, L49
- Kinugawa, T., Nakamura, T., & Nakano, H. 2021b, *PTEP*, **2021**, 021E01
- Kinugawa, T., Nakano, H., & Nakamura, T. 2016b, *PTEP*, **2016**, 103E01
- Kinugawa, T., Nakano, H., & Nakamura, T. 2016c, *PTEP*, **2016**, 031E01
- Kirihara, T., Tanikawa, A., & Ishiyama, T. 2019, *MNRAS*, **486**, 5917
- Klencki, J., Nelemans, G., Istrate, A. G., & Chruslinska, M. 2021, *A&A*, **645**, A54
- Komiya, Y., Suda, T., & Fujimoto, M. Y. 2015, *ApJL*, **808**, L47
- Kozai, Y. 1962, *AJ*, **67**, 591
- Kruckow, M. U., Tauris, T. M., Langer, N., Kramer, M., & Izzard, R. G. 2018, *MNRAS*, **481**, 1908
- Kudritzki, R. P., Pauldrach, A., Puls, J., & Abbott, D. C. 1989, *A&A*, **219**, 205
- Kudritzki, R. P., & Reimers, D. 1978, *A&A*, **70**, 227
- Kumamoto, J., Fujii, M. S., & Tanikawa, A. 2019, *MNRAS*, **486**, 3942
- Kumamoto, J., Fujii, M. S., & Tanikawa, A. 2020, *MNRAS*, **495**, 4268
- Kushnir, D., Zaldarriaga, M., Kollmeier, J. A., & Waldman, R. 2016, *MNRAS*, **462**, 844
- Leigh, N. W. C., Geller, A. M., McKernan, B., et al. 2018, *MNRAS*, **474**, 5672
- Leung, S.-C., Nomoto, K., & Blinnikov, S. 2019, *ApJ*, **887**, 72
- Lidov, M. L. 1962, *P&SS*, **9**, 719
- Liu, B., & Bromm, V. 2020a, *MNRAS*, **495**, 2475
- Liu, B., & Bromm, V. 2020b, *ApJL*, **903**, L40
- Liu, B., & Lai, D. 2019, *MNRAS*, **483**, 4060
- Liu, B., Meynet, G., & Bromm, V. 2021, *MNRAS*, **501**, 643
- Liu, J., Zhang, H., Howard, A. W., et al. 2019, *Natur*, **575**, 618
- Liu, J., Zheng, Z., Soria, R., et al. 2020, *ApJ*, **900**, 42
- Machida, M. N., & Doi, K. 2013, *MNRAS*, **435**, 3283
- Machida, M. N., Omukai, K., Matsumoto, T., & Inutsuka, S.-i. 2008, *ApJ*, **677**, 813
- Madau, P., & Dickinson, M. 2014, *ARA&A*, **52**, 415
- Magg, M., Hartwig, T., Agarwal, B., et al. 2018, *MNRAS*, **473**, 5308
- Magg, M., Hartwig, T., Glover, S. C. O., Klessen, R. S., & Whalen, D. J. 2016, *MNRAS*, **462**, 3591
- Magg, M., Klessen, R. S., Glover, S. C. O., & Li, H. 2019, *MNRAS*, **487**, 486
- Maggiore, M., Van Den Broeck, C., Bartolo, N., et al. 2020, *JCAP*, **2020**, 050
- Mandel, I. 2016, *MNRAS*, **456**, 578
- Mandel, I., & de Mink, S. E. 2016, *MNRAS*, **458**, 2634
- Mangiaglia, A., Bonetti, M., Sesana, A., & Colpi, M. 2019, *ApJL*, **883**, L27
- Mapelli, M. 2016, *MNRAS*, **459**, 3432
- Mapelli, M., & Giacobbo, N. 2018, *MNRAS*, **479**, 4391
- Mapelli, M., Giacobbo, N., Ripamonti, E., & Spera, M. 2017, *MNRAS*, **472**, 2422
- Mapelli, M., Giacobbo, N., Santoliquido, F., & Artale, M. C. 2019, *MNRAS*, **487**, 2
- Mapelli, M., Santoliquido, F., Bouffanais, Y., et al. 2020, arXiv:2007.15022
- Marchant, P., Langer, N., Podsiadlowski, P., Tauris, T. M., & Moriya, T. J. 2016, *A&A*, **588**, A50
- María Ezquiaga, J., & Holz, D. E. 2021, *ApJL*, **909**, L23
- Marigo, P., Girardi, L., Chiosi, C., & Wood, P. R. 2001, *A&A*, **371**, 152
- McKernan, B., Ford, K. E. S., Bellovary, J., et al. 2018, *ApJ*, **866**, 66
- McKernan, B., Ford, K. E. S., & O'Shaughnessy, R. 2020, *MNRAS*, **498**, 4088
- Mennekens, N., & Vanbeveren, D. 2014, *A&A*, **564**, A134
- Nakamura, F., & Umemura, M. 2001, *ApJ*, **548**, 19
- Nakamura, T., Ando, M., Kinugawa, T., et al. 2016, *PTEP*, **2016**, 093E01
- Nieuwenhuijzen, H., & de Jager, C. 1990, *A&A*, **231**, 134
- Nitz, A. H., & Capano, C. D. 2021, *ApJL*, **907**, L9
- O'Leary, R. M., Kocsis, B., & Loeb, A. 2009, *MNRAS*, **395**, 2127
- Olejak, A., Fishbach, M., Belczynski, K., et al. 2020, *ApJL*, **901**, L39
- Omukai, K., & Nishi, R. 1998, *ApJ*, **508**, 141
- Omukai, K., & Palla, F. 2001, *ApJL*, **561**, L55
- Omukai, K., & Palla, F. 2003, *ApJ*, **589**, 677
- Park, D., Kim, C., Lee, H. M., Bae, Y.-B., & Belczynski, K. 2017, *MNRAS*, **469**, 4665
- Petrovich, C., & Antonini, F. 2017, *ApJ*, **846**, 146
- Piran, Z., & Piran, T. 2020, *ApJ*, **892**, 64
- Portegies Zwart, S. F., & McMillan, S. L. W. 2000, *ApJL*, **528**, L17
- Punturo, M., Abernathy, M., Acernese, F., et al. 2010, *CQGra*, **27**, 194002
- Rasskazov, A., & Kocsis, B. 2019, *ApJ*, **881**, 20
- Rastello, S., Amaro-Seoane, P., Arca-Sedda, M., et al. 2019, *MNRAS*, **483**, 1233
- Reitze, D., Adhikari, R. X., Ballmer, S., et al. 2019, *BAAS*, **51**, 35
- Repetto, S., Igoshev, A. P., & Nelemans, G. 2017, *MNRAS*, **467**, 298
- Repetto, S., & Nelemans, G. 2015, *MNRAS*, **453**, 3341
- Riley, J., Mandel, I., Marchant, P., et al. 2020, arXiv:2010.00002
- Rodriguez, C. L., Amaro-Seoane, P., Chatterjee, S., et al. 2018a, *PhRvD*, **98**, 123005
- Rodriguez, C. L., Amaro-Seoane, P., Chatterjee, S., & Rasio, F. A. 2018b, *PhRvL*, **120**, 151101
- Rodriguez, C. L., & Antonini, F. 2018, *ApJ*, **863**, 7
- Rodriguez, C. L., Chatterjee, S., & Rasio, F. A. 2016a, *PhRvD*, **93**, 084029
- Rodriguez, C. L., Haster, C.-J., Chatterjee, S., Kalogera, V., & Rasio, F. A. 2016b, *ApJL*, **824**, L8
- Rodriguez, C. L., Zevin, M., Amaro-Seoane, P., et al. 2019, *PhRvD*, **100**, 043027
- Roupa, Z., & Kazanas, D. 2019, *A&A*, **632**, L8
- Ryderberg, C.-E., Zackrisson, E., Lundqvist, P., & Scott, P. 2013, *MNRAS*, **429**, 3658
- Safarzadeh, M., & Haiman, Z. 2020, *ApJL*, **903**, L21
- Safarzadeh, M., & Hotokezaka, K. 2020, *ApJL*, **897**, L7
- Samsing, J. 2018, *PhRvD*, **97**, 103014
- Samsing, J., Askar, A., & Giersz, M. 2018, *ApJ*, **855**, 124
- Samsing, J., & Ramírez-Ruiz, E. 2017, *ApJL*, **840**, L14
- Santoliquido, F., Mapelli, M., Bouffanais, Y., et al. 2020, *ApJ*, **898**, 152
- Sasaki, M., Suyama, T., Tanaka, T., & Yokoyama, S. 2016, *PhRvL*, **117**, 061101
- Schauer, A. T. P., Drory, N., & Bromm, V. 2020, *ApJ*, **904**, 145
- Sesana, A. 2016, *PhRvL*, **116**, 231102
- Sesana, A., Gair, J., Mandel, I., & Vecchio, A. 2009, *ApJL*, **698**, L129
- Sharda, P., Federrath, C., & Krumholz, M. R. 2020, *MNRAS*, **497**, 336
- Silsbee, K., & Tremaine, S. 2017, *ApJ*, **836**, 39
- Simón-Díaz, S., Maíz Apellániz, J., Lennon, D. J., et al. 2020, *A&A*, **634**, L7
- Skinner, D., & Wise, J. H. 2020, *MNRAS*, **492**, 4386
- Spera, M., Mapelli, M., & Bressan, A. 2015, *MNRAS*, **451**, 4086
- Spera, M., Mapelli, M., Giacobbo, N., et al. 2019, *MNRAS*, **485**, 889
- Stacy, A., Bromm, V., & Loeb, A. 2011, *MNRAS*, **413**, 543
- Stacy, A., Greif, T. H., & Bromm, V. 2012, *MNRAS*, **422**, 290
- Stahler, S. W., Palla, F., & Salpeter, E. E. 1986, *ApJ*, **302**, 590
- Stevenson, S., Vigna-Gómez, A., Mandel, I., et al. 2017, *NatCo*, **8**, 14906
- Stone, N. C., Metzger, B. D., & Haiman, Z. 2017, *MNRAS*, **464**, 946
- Sugimura, K., Matsumoto, T., Hosokawa, T., Hirano, S., & Omukai, K. 2020, *ApJL*, **992**, L14
- Susa, I. 2013, *ApJ*, **773**, 185
- Susa, H. 2019, *ApJ*, **877**, 99
- Susa, H., Hasegawa, K., & Tominaga, N. 2014, *ApJ*, **792**, 32
- Suzuki, T. K. 2018, *PASJ*, **70**, 34
- Tagawa, H., Haiman, Z., Bartos, I., & Kocsis, B. 2020a, *ApJ*, **899**, 26
- Tagawa, H., Haiman, Z., & Kocsis, B. 2020b, *ApJ*, **898**, 25
- Takahashi, K., Sumiyoshi, K., Yamada, S., Umeda, H., & Yoshida, T. 2019, *ApJ*, **871**, 153
- Takahashi, K., Yoshida, T., & Umeda, H. 2018, *ApJ*, **857**, 111
- Takahashi, K., Yoshida, T., Umeda, H., Sumiyoshi, K., & Yamada, S. 2016, *MNRAS*, **456**, 1320
- Tanaka, S. J., Chiaki, G., Tominaga, N., & Susa, H. 2017, *ApJ*, **844**, 137
- Tanikawa, A. 2013, *MNRAS*, **435**, 1358

- Tanikawa, A., Kinugawa, T., Kumamoto, J., & Fujii, M. S. 2020a, *PASJ*, **72**, 39
- Tanikawa, A., Kinugawa, T., Yoshida, T., Hijikawa, K., & Umeda, H. 2020b, arXiv:2010.07616
- Tanikawa, A., Suzuki, T. K., & Doi, Y. 2018, *PASJ*, **70**, 80
- Tanikawa, A., Yoshida, T., Kinugawa, T., Takahashi, K., & Umeda, H. 2020c, *MNRAS*, **495**, 4170
- Tarumi, Y., Hartwig, T., & Magg, M. 2020, *ApJ*, **897**, 58
- The LIGO Scientific Collaborationthe Virgo Collaboration, Abbott, R., et al. 2020, arXiv:2010.14533
- Tout, C. A., Aarseth, S. J., Pols, O. R., & Eggleton, P. P. 1997, *MNRAS*, **291**, 732
- Trani, A. A., Spera, M., Leigh, N. W. C., & Fujii, M. S. 2019, *ApJ*, **885**, 135
- Umeda, H., & Nomoto, K. 2002, *ApJ*, **565**, 385
- VanLandingham, J. H., Miller, M. C., Hamilton, D. P., & Richardson, D. C. 2016, *ApJ*, **828**, 77
- Vassiliadis, E., & Wood, P. R. 1993, *ApJ*, **413**, 641
- Venumadhav, T., Zackay, B., Roulet, J., Dai, L., & Zaldarriaga, M. 2020, *PhRvD*, **101**, 083030
- Vink, J. S., & de Koter, A. 2005, *A&A*, **442**, 587
- Vink, J. S., de Koter, A., & Lamers, H. J. G. L. M. 2001, *A&A*, **369**, 574
- Wang, C., Jia, K., & Li, X.-D. 2016, *MNRAS*, **457**, 1015
- Webbink, R. F. 1984, *ApJ*, **277**, 355
- Willems, B., Henninger, M., Levin, T., et al. 2005, *ApJ*, **625**, 324
- Wong, T.-W., Valsecchi, F., Fragos, T., & Kalogera, V. 2012, *ApJ*, **747**, 111
- Woosley, S. E. 2017, *ApJ*, **836**, 244
- Woosley, S. E., Blinnikov, S., & Heger, A. 2007, *Natur*, **450**, 390
- Yang, Y., Bartos, I., Haiman, Z., et al. 2019, *ApJ*, **876**, 122
- Yoon, S. C., Dierks, A., & Langer, N. 2012, *A&A*, **542**, A113
- Yoon, S. C., Woosley, S. E., & Langer, N. 2010, *ApJ*, **725**, 940
- Yoshida, N., Omukai, K., & Hernquist, L. 2008, *Sci*, **321**, 669
- Yoshida, T., Takiwaki, T., Kotake, K., et al. 2019, *ApJ*, **881**, 16
- Yoshida, T., Umeda, H., Maeda, K., & Ishii, T. 2016, *MNRAS*, **457**, 351
- Yungelson, L. R., Kuranov, A. G., Postnov, K. A., & Kolesnikov, D. A. 2020, *MNRAS*, **496**, L6
- Zackay, B., Dai, L., Venumadhav, T., Roulet, J., & Zaldarriaga, M. 2019, arXiv:1910.09528
- Zevin, M., Berry, C. P. L., Coughlin, S., Chatzioannou, K., & Vitale, S. 2020, *ApJL*, **899**, L17
- Ziosi, B. M., Mapelli, M., Branchesi, M., & Tormen, G. 2014, *MNRAS*, **441**, 3703